Pattern Detection in Medical Imaging: Pathology Specific Imaging Contrast, Features, and Statistical Models

by

Sinchai Tsao

A Dissertation Presented to the
FACULTY OF THE USC GRADUATE SCHOOL
UNIVERSITY OF SOUTHERN CALIFORNIA
In Partial Fulfillment of the
Requirements of the Degree
DOCTOR OF PHILOSOPHY
(Biomedical Engineering)

December 2013

Dedicated to the memory of Manbir Singh, PhD

Born Oct. 7, 1945 in Amritsar, India, Manbir Singh earned his Ph.D. in physics from UCLA in 1971, before conducting his postdoctoral studies in biomedical physics at UCLAs Laboratory of Nuclear Medicine and Radiation Biology.

He later spent one year as a Visiting Scholar of the American Heart Association at the Mayo Clinic in Rochester, Minn., where he conducted the first studies in single-photon emission computed tomography (SPECT). He joined the Department of Radiology at USC in 1977 and received an appointment in biomedical engineering in 1988.

Singh pioneered the use of SPECT to detect and quantify acute myocardial infarctions in three dimensions and was one of the first investigators to demonstrate the synergism of CT scans and nuclear medicine SPECT imaging in detecting and visualizing both the anatomy and function of the heart.

He was the nationally elected AdCom representative for Nuclear Medical Sciences in the IEEE Nuclear and Plasma Society (NPSS) from 1986 to 1989, co-founder of the IEEE Medical Imaging Conference in 1990, the technical chair for nuclear medical sciences within IEEE NPSS from 1991 to 1993 and scientific program chair of the 1992 and 1993 IEEE Medical Imaging conferences.

His latest interests were in functional magnetic resonance imaging (MRI) and diffusion tensor imaging (DTI) tractography with applications of DTI to Alzheimers disease and traumatic brain injuries. He was founder and director of the neuroimaging core at USC, which develops new methodology in functional MRI and DTI.

Singh also was founding director of the graduate program in biomedical imaging in the Department of Biomedical Engineering.

Singh passed away due to unknown causes while visiting family in India in the winter of 2011. He is survived by his wife, Heidi and their son, Kabir.

Acknowledgements

I would like to first and foremost thank my loving wife, Kori, who has been with me through this long process and supported me through it all. I definitely couldn't have done it without you! Thank you for being there through all the late nights, lab changes and grumpiness of failed experiments. You've sacrificed so much for this volume of work. It belongs as much to you as much it is to me. To my parents, Winnie and Fred, who raised me to think independently and not to be swayed by other's opinions. My darling sister, Sonia, who continues to inspire me daily with her courage and never ceasing enthusiasm for life. My in-laws, Sharon and Rodney, who generously shared their academic journeys and who was always there to listen to my research problems. I would like to especially recognize the members of my qualifying and defense committee members. Your invaluable and thoughtful feedback and evaluation has made me the researcher I am today. For my qualifying examination: Krishna Nayak (Chair), Vasilis Marmarelis, Walter Wolf, Richard Leahy and Arkadiusz Gertych. For my defense: Natasha Lepore (Chair), Norberto Grzywacz, Vasilis Marmarelis, Walter Wolf and Arkadiusz Gertych. Behind the scene, we have Mischalgrace Diasanta, our under appreciated graduate student advisor and my friend. I believe a piece of this thesis belongs to every one of you. Your support through the years have been incredible. I truly could not have done this without you.

This thesis is dedicated to Manbir Singh, PhD. My mentor, advisor and friend who passed away in 2011. Although many people have mentored and helped me through my PhD training, Dr. Singh is definitely the most influential person in my academic life. Dr. Singh was my PhD advisor from 2008-2011 but the bulk of the work of this PhD is a continuation of his research program and legacy. I started my life at USC learning Medical Imaging from him through his classes: BME 425 & 525. His lab was full at the time and it was not until 2008 did I have the opportunity to join his group. I believe that this fortuitous event was one of the best things that have ever happened to me. I would like to thank him for his dedication to his many students including myself. His legacy lives within this body of work as well as any other work I do in the future. Thank you Dr. Singh! Mrs Heidi Singh and Kabir, Thank you for sharing your husband / father with us, this would not have been possible without you or him.

I would also like to thank my many mentors and I've been so lucky and grateful to have been able to learn from all of you (in no particular order):

The inspirational Natasha Lepore who adopted me when I was advisor-less and got me through the tough last year of my PhD. I will forever be grateful for your mentorship and how you helped me set the course of my career. Arek Gertych my constant mentor of

throughout my PhD who taught me everything I know about up and downs of research and how to do research with integrity. Meng Law who provide us guidance and support during our toughest times. Jorge Documet who was my coding partner and teacher, you truly inspired me with your ability to write elegant code. Dr. Helena Chui, who was my perfect role model for a brilliant yet dedicated and humble medical researcher. Dr. Walter Wolf, you encapsulate the researcher and person that I want to be. Thank you for mentoring me and sharing your life experiences with me. Krishna Nayak who inspired us with his passion for learning and drive for research. Norberto Gzywacz for all your inspirational leadership of the BME department as well as your care and support through our loss of Manbir Singh. I would not be here without Michael Khoo who as chair of the BME department gave me the opportunity to prove myself as a researcher and never stop believing in me. Tanja Adam the brilliant neurobiologist who directed me through the pediatric obesity portion of this work. Katie Page for the opportunity to work on the fructose vs glucose studies. Vidya Rajagopalan, I don't know what I would have done had our paths not crossed. Not only did you support me through my last year of my PhD but have been instrumental in getting me started with a new chapter of my academic life. Brent Liu and Bernie Hwang who guided me through my first years of my PhD. Alexander Lin, for sharing his journey to faculty with me and his many words of encouragement and guidance throughout the years. Ihab Hajjar, thank you for your support and being so generous to me. I can't wait to see the results of your clinical trial. Tara Chklovski for giving the opportunity to work with the kids at Iridescent and supporting my research. Yiqiao Song and Sharron Lin, thank you so much for all your support over the years. From the early days giving me advice over the phone to visiting you on the east coast. I'm truly grateful for your encouragement and generosity. Karen Johnson, I really couldn't have done this without you! The BME department at USC is so lucky to have you. Thank you for your support through the ups and downs and especially when we loss Dr. Singh. All the Professors who have guided me: Harry Hu, David D'Argenio, Ellis Meng, Jesse Yen, Kirk Shung, Gerald Loeb, Ted Burger, Francis Richmond, Bob Scholtz, Jay Kuo, Urbashi Mitra, Bosco Tjan, T.K. Hsiai, Bartlett Mel, Massoud Ghyam-Khah, Manouchehr Moradi, Kathleen Allen, Heinz Lemke, Jianguo Zhang, Maria Law, Stephan Buml, Anita Zimmerman, Sharon Swartz, Christine Kearney, Anubhav Tripathi, Michael Lysaght, John Stein, Robert Pelcovits, Chung-I Tan, James Valles, Sean Ling, Thomas Banchoff, Jonathan Waage, Toby Cumberbatch, ...

My many many (lab) mates current and past! But especially ... Darryl Hwang, it's been a pleasure working with you in the lab, hanging out and learning from you. I have

always and forever will be been impressed by your love for your work and will miss those long days working hard and then playing hard. Niharika Gajawelli, it has been a pleasure working with you. I believe you will make an amazing researcher and I stand by it. Bryce Wilkins, thank you for coming down this long and difficult road with me. I know I will continue to learn from you for many years to come. Sam Ma, I'm so excited for you. Thank you so much for working with me. Nam (Namgyun Lee), can't wait until you get back to the US after your military service and we can work together again. Yi Lao, I'm so lucky to have so many inspiring lab mates you are definitely one of the top ones. Fernando Yepes, wish we had more time to work together in Los Angeles. It has been a great honor to have been able to work with you. You've been a great inspiration and will continue to be for many years to come. Kevin Ma, my housemate, lab mate and my friend. This volume of work in many ways document our learning journey together at USC. You've contributed to it in so many ways. Anika Joseph, couldn't have done it without your energy and companionship in this crazy journey to a doctorate. Anh Le, I have learned so much from you. A lot this work reminds me of our first years as a PhD student taking classes and learning to be strong researchers. I thank you for all the things you have taught me over the years. Witaya Sungkarat. P'Wit, I believe more than half the things I know I have learned from you. I continue the legacy that you've left behind at USC. You'll always be part of who I am as a researcher. David Woollard, the committee loved all the suggestions you made for my qualifying examination. As always I am ever impressed by your work and your passion. As I put my defense together, I can see how I've applied what you've taught me! Thank you! Mark Haney, I wish we have more chances to work together. I will never forget your drive, determination and incredible spirit. Lauren Brown, it's been a pleasure working with you. I would really like the chance to work together in the future. I'm so excited for you starting your interdisciplinary work in Gerontology. Others including but limited to Jose Iriarte-Diaz, Kristin Bishop, Kevin M. Middleton, ...

To the rest of my family and friends: Erick Soedjasa, thank you for your friendship and support. My Tsao cousins Allegra and Spencer, you have both inspired me and more ways than you know! My Lin cousins Charles, Stephanie, Michelle, Felicia, Andre, Jeremy and Judith, thank you for loving support. In particular, Andre thanks for sharing your USC college life with me. My uncle and aunts, Mary Ann, Bennett, Calvin, David, Zack, Cheryd, Alfred, Liz, Michael, Winnie, John, Wendy and last but not least Rebecca. This work is full of your love and support. To my grandparents, this would not have been

possible if you had not braved the turmoils of our home country to give us all a better life.

And so many others that have contributed in their own unique way to this volume of work: [Again, in no particular order]

Bing G.	Geo T	Terrence J	Limei C
Lucy Z	Harry S	Vanessa L	Jonathan L
Jasper L	Guru S	Hung D	Susan C
Sharon J	Jefferey C	Brian W	Chaithanya R
Paul B	Jay F	Yinghua Z	Rosa C
Alan S	Leslie K	Yoon K	Adam W
Talia BY	Melissa F	Ida A	Leon C
Hugh P	Maya C	Matt B	Christian G
Marvin N	Phillip H	Ronalee L	Vivek P
Mary BN	Sadaf S	Jay M	Rachelle B
Sam Valencerina	Rui Z	Manish K	Leanne C
Vincent C	Sam Lin	Gabriela MO	Arthi S
Brian Lim	Sang C	Flavia O	Kelsey S
Josh B	Sam Cunningham	Andrew W	Orian L
Travis P	Ude L	Jae Youn H	Ami S
Mandy L	Peggy H	Man N	Bryce C
Pirran T	Jeff T	Nadav I	Debra F
Kenny K	Kathryn D	Fei Yu	Thad P
Jin Ho O	Dan T	Chris N	Mary H
Devyani N	Patrick H	Helene N	Tim Chklovski
Alice C	Jon C	David F	Julia Castro
Shruthi N	Hsu-Lei Lee	Dennis M	Luz Rivas
Shivanth B	Syed A	Lauren H	Jenna Blanton
Ming S	Wesley Z	Aneeta J	Mariana R
Vanessa G	Mahender M	Jamuna M	Paul Yarin
Alexis W	Samir S	Xenia Z	Kara Christianson
Wenli W	Chris Sandino	Yue Kang	Lindsey JS
Angelica D	Wayne C	Joseph M	Erika A
Brian Li	Davi L	Chi Hyung (JJ) Seo	Jennifer Hsu
Caroline W	Ahsan J	Winston T	Srinivas Yerramalli
Dong S	Yi Guo	Djordje P	
Heidi G	Eamon D	Jarree C	

All the Kids at Iridescent!!

Table of Contents

List of Figures

List of Tables

Acronyms

AD Alzheimer's Disease. xxi, 5, 8, 9

BOLD Blood Oxygen Level Dependent. 10, 183

CSF Cerebrospinal Fluid. 5, 8

CST Corticospinal Tract. 9

CT Computed Tomography. 5

DTI Diffusion Tensor Imaging. 8, 12

EBM evidence-based medicine. xxi, 1, 7

EMR Electronic Medical Record. 3

FLAIR fluid attenuated inversion recovery. 12

fMRI functional magnetic resonance imaging. xxi, 4, 12

HRF Hemodynamic Response Function. 10, 183

MANN massive artificial neural network. 185

MCI Mild Cognitive Impairment. 5

MRI magnetic resonance imaging. 5, 8, 12

PACS Picture Archival and Communication System. xxi, 3

QEBM quantitative evidence-based medicine. 7

RIS Radiology Information System. 3

SMS Short Message Service. xxi, 3

SVM Support Vector Machine. 185

WMH white matter hyperintensity. 12

Abstract

The motivation for this work is a vision of widespread adoption of a priori quantitative epidemiological information for clinical decision-making, and can be seen as a quantitative large-scale extension of evidence-based medicine (EBM) [2]. Medical images can be seen as a spatially encoded map of physiological measurements that can be used to predict prognosis and to drive treatment plans. This paradigm can be very powerful and is driven by the recent big data revolution in computer science as well as the increasing availability of medical imaging modalities due to decreases in manufacturing costs. In order to achieve this overarching goal, three practical requirements must be reached and correspond to the parts of this thesis: Part A: Developing IT infrastructure and technology that enables the dataset to be properly collected and organized for analysis. Part B & C: Generation of functional (Part B) and structural (Part C) medical imaging contrast that are optimized for analysis. Part D: Pattern recognition techniques (including both image processing and machine learning techniques) to mine information from the large imaging datasets generated. As part of the thesis, I discuss my contribution to IT infrastructure (Part A) by developing a Short Message Service (SMS)-based system to control the clinically used Picture Archival and Communication System (PACS) (Ch.2) as well as an imaging study tool that categorizes patient imaging data for use in retrospective studies(Ch.3). I then go on to detail my work with functional neuroimaging of obesity using functional magnetic resonance imaging (fMRI)(Ch.4) and (Ch.5). Chapters 6-9 details my efforts at studying abnormal aging versus normal aging using diffusion MRI as well as applications of diffusion MRI to surgical planning. Chapters 10 discusses my work integrating diffusion MR with FLAIR MRI to investigate the properties of white matter lesions and how it can be used in the clinical setting. Chapter 11 then moves on to talk about my work modifying standard brain parcellation techniques to allow them to work with aged brains with large infarcts. Chapters 6-11 altogether represent my efforts in structural neuroimaging using MRI (Part C). The thesis then closes with capstone work in development staging using hand x-rays using fuzzy logic (Ch. 12 & 13). To close the work with Alzheimer's Disease (AD) and aging, we used machine learning techniques to predict disease progression based on a baseline MRI scan as well as higher order analysis of our diffusion MRI dataset by integrating MRI information with other clinical information such as neuropsychological tests, cardiovascular status. This is all in an effort to computationally explore the relationship between MRI measurements and clinical presentation of disease as measured by neuropsychological scores. Similarly with the Obesity work, we related fMRI activation differences between high and low calorie foods with non-imaging information such as insulin resistance (Ch. 16).

Chapter 1

Introduction

子曰："知之为知之，
不知为不知，是知也。"

Real `knowledge` *is* `knowing` *what you* `know` *and what you* `don't know`. *Confucius*

1 Motivation

The motivation for this work is a vision of widespread adoption of a priori quantitative epidemiological information for clinical decision-making, and can be seen as a quantitative large-scale extension of evidence-based medicine [2]. Medical Images can be thought of a structured multi-dimensional form of medical data. The structure comes from the fact that each voxel or image matrix value is related spatially to neighboring values and its location in the image matrix has anatomical meaning. Pattern detection / statistical analysis using this information can exploit not only the measurements or matrix

values but also their patterns related to matrix indices (i.e. in the hippocampus, certain cortex region, etc) to predict prognosis and to drive treatment plans. This paradigm can be very powerful and is driven by the recent big data revolution in computer science: As data storage prices have plummeted, databases sizes have exponentially increased and high computational power have become increasingly ubiquitous. Meanwhile, there have been significant advances in improving the availability of medical imaging modalities as clinical diagnostic tools. This is mainly due to decreases in manufacturing costs, but also because physicians have found them to be increasingly useful as screening tools. However, in order to take advantage of this unique increase in medical data, we also require a revolution in analysis techniques that can handle high dimensionality, multiple comparison issues as well as the unique challenges that come with medical information and medical imaging datasets (imaging artifacts, sampling issues, etc).

In order to achieve this overarching goal, three practical requirements must be reached and correspond to the parts of this thesis:

1. Part A: Development of IT infrastructure and technologies that enables imaging data to be properly collected and organized for analysis.

2. Part B & C: Generation of functional (Part B) and structural (Part C) medical imaging contrast that are optimized for analysis.

3. Part D: Pattern recognition techniques (including both image processing and machine learning techniques) to mine information from the large imaging datasets generated.

The overarching vision of this thesis is to contribute to building advanced computational techniques that leverage a priori information to characterize disease progression

and to support clinical decision-making. This is important not only in the context of providing benchmarks for developing treatments but provides a way to understand basic biological processes.

2 Overview

2.1 Part A: Imaging Informatics

Before being able to leverage advanced computational techniques, we have to address the basic problem of getting information (in this case medical images) properly classified and organized. To this end, in chapter 2, we developed a SMS-based routing system to remotely manage the PACS database. In terms of image classification, the information required currently lives on a number of separate databases in the clinic, including the PACS, Radiology Information System (RIS) and increasingly the Electronic Medical Record (EMR). Important image meta-information such as the radiologist's report as well as patient demographic information lives on the RIS database and the medical images are stored in the PACS. The two systems are often from different vendors with limited integration. It is, therefore, difficult to classify images for retrospective studies and data mining. To compound this problem further, epidemiological information on the RIS is unstructured and exists in a pure text form as a radiologist's report. To this end, I developed a prototype system in chapter 3 that classifies the medical images in the PACS using extracted structured information from the RIS.

2.2 Part B & C: Functional and Structural Neuroimaging

Next we address the quality of the information. In medical imaging, this means generating high signal to noise ratio (SNR) / low noise images with meaningful contrast. There are two overall types of magnetic resonance imaging (MRI) contrast: Contrast based on structure and those based on function. In structural MRI, the system recreates image matrices that are representations of the object / person. We can take advantage of physical properties of the magnetic dipoles in the body and alter the pulse sequence parameters to change how contrast is generated. Functional techniques can be seen as an extension of structural imaging which require the subject to perform a certain task. The differences in images acquired during different tasks versus control yield the contrast desired.

Improving sensitivity of the both the functional and structural image contrast allows us to detect ever smaller variations. In Chapter 4, we were able to take a large number of data samples and measure small but significant changes in the T2* signal between a control and a stimulated state. To give you an idea of what changes can be detected in state-of-the-art medical imaging, the actual change in T2* weighted image/signal intensity is in the order of 1-3%. With multiple repetition of the same stimulus / presentation paradigm over time and averaging of this signal, the 1-3% raw signal change can be converted in to a much more manageable change of about 2-3 standard deviations. This is only possible because in fMRI, we trade image quality for sensitivity and speed.

The signal changes measured in fMRI are intra-subject. This problem becomes even more difficult with inter-subject population studies using structural scans such as the diffusion MR studies in Part C of the thesis. In these studies, it is more important to have high quality data that has high SNR / low error since it is rare to have 1000s of

subject scans to decrease our standard deviation sizes. In these cases, the actual signal deviations are closer to 10% of the raw signal. Therefore, artifact correction techniques such as Cerebrospinal Fluid (CSF) correction (Chapter 8) as well as proper feature extraction (Chapter 13) can really improve statistical power when doing large group studies. Moreover, the image intensity differences are "perceived" very differently by the human eye versus the computer algorithm. For example, group-wise small signal changes undetectable by the human eye can be statistically significant when using large number of subjects. We demonstrated this with our MR studies comparing Normal Control (NC), Mild Cognitive Impairment (MCI) and Probable AD subjects (Chapters 6,9,15).

2.3 Part D: Statistical Analysis and Machine Learning

All of these efforts allows us to create images that have high SNR and low noise with respect to the desired contrast. These contrasts can be functional (Part B) or structural (Part C) in nature. Once we have good contrast, the problem is to then design methods that integrate these images with other clinical information so as to better understand the complex relationship between laboratory diagnostic tests (such as hematological, genetic, etc), neuropsychological examinations and the images created from the subject. This work is contained in Part D of the thesis.

In recent years, there have been tremendous increases in the speed and ubiquity of diagnostic systems, leading to a dramatic surge in the amount of clinical diagnostic information, both imaging and non-imaging, available for driving treatment. For example, in chapters 15 & 16, the studies contained both MRI information as well as large collection of clinical measures such as neuropsychological scores, cardiovascular status and insulin response.

In the clinic, however, physicians are usually able to only consider a select number of information to make treatment decisions. This is where computational techniques are useful. By integrating all significant portions of large multi-dimensional datasets, machine learning and other pattern recognition techniques allows us to find trends and patterns in large datasets that might gives us an edge on treatment planning. The question is then how to design meaningful computation techniques of dimension reduction.

One approach is to use pieces of existing information to put a priori constraints on the analysis. A lot of reasonable assumptions can be made: For example, in Chapter 14, we assumed that disease progress is gradual and relatively monotonic. Hence, we put a constraint on expecting our output disease progression measure (in this case, cognitive ability) to be changing monotonically when sampled at 6 month intervals. In many cases simpler approaches that such as multivariate permutation testing (Ch. 15) and fuzzy logic (Ch. 12) are sufficient in accurately doing classification or regression analysis.

Our results are promising, by using fuzzy logic we were able to mimic the pattern detection work done by pediatric radiologists in matching pediatric hand x-rays to an atlas to predict the patient's bone age. At geriatric end of research (Ch. 15), we have began to be able to isolate the different parts of the brain that correlates with normal aging, acute insult and long term genetic factors (such as ApoE). In our machine learning work (Ch. 14), we are beginning to be able to predict disease progression in the next 48 months by using baseline measures from both clinical testing as well as structural images. Finally, in our childhood obesity work (Ch.16), we were able to link the amount of difference in brain activation between low and high calorie with insulin resistance, suggesting that the amount of insulin resistance may play a role in regulating the reward pathway response to food or vice versa.

3 Organization

	Project	Bone Age	Aging & Dementia			Obesity		PACS
		⋮	⋮	⋮	⋮	⋮	⋮	⋮
	Modality	X-ray	FLAIR	DTI	T1	fMRI	fcMRI	PACS
A	Imaging							Ch. 2
	Informatics							Ch. 3
B	Functional					Ch. 4		
	Neuroimaging						Ch. 5	
C	Structural Neuroimaging		Ch. 10	Ch. 6 Ch. 7 Ch. 8 Ch. 9	Ch. 11			
D	Statistics & M.L.	Ch. 12 Ch. 13		Ch. 15	Ch. 14	Ch. 16		

Figure 1.1: Organizational chart for this thesis

This thesis organized into four parts:

1. Imaging Informatics
2. Functional Neuroimaging
3. Structural Neuroimaging
4. Statistical Analysis and Machine Learning in Medical Imaging

Each part of this thesis outlines my contribution to a particular sub-discipline within Medical Imaging; Part A outlines my work in improving access to medical imaging information by optimizing how digital medical imaging information is transmitted (chapter 2) and organized (chapter 3), Part B details my contribution to **functional** Neuroimaging in particular fMRI in the study of obesity where we applied statistical techniques not only in the time domain (chapters 4 & 5) but also in the subject group domain (chapter 16). Part C talks about my contribution to **structural** MRI, it takes the functional techniques in Part B and applies it to measure inter subject variation (chapter 15. It also outlines my contribution to Diffusion MRI, in particular, Diffusion Tensor Imaging (DTI) where I've worked on improving image contrast (chapter 8) as well as tractography (chapter 6,7,9). Lastly, I outline my efforts at looking at white matter hyperintensity (WMH)s, a characteristic of white matter damage shown in fluid attenuated inversion recovery (FLAIR) images. Part D demonstrates applications of various machine learning techniques in capstone applications of automated skeletal age assessment (chapter 12) and predicting disease progression based on a baseline MRI scan.

These medical imaging methods were applied to three main research areas:

1. Obesity and Reward Pathway Disorders
2. Dementias and Aging
3. Skeletal developmental disorders and Bone Age Assessment.

The fourth area PACS can be seen as creating enabling imaging IT infrastructure for the three main research areas.

Part A

Imaging Informatics

Chapter 2

Managing Healthcare Information Using Short Message Service (SMS) in Wireless Broadband Networks

Jorge Documet[a] , Sinchai Tsao[a] , Luis Documet[b], Brent J. Liu[a] ,
Zheng Zhou[a] , Anika O. Joseph[a]

[a] Image Processing and Informatics Lab, Department of Radiology, ISI/USC,
Marina Del Rey, CA USA 90292;
[b] Saint Johns Health Center, 1328 Twenty-Second Street,
Santa Monica, CA USA 90404-2091;

Medical Imaging 2007: PACS and Imaging Informatics, edited by Steven C. Horii, Katherine P. Andriole, Proc. of SPIE Vol. 6516, 65160T, (2007) 1605-7422/07/$18 doi: 10.1117/12.710160

1 Abstract

Due to the ubiquity of cell phones, SMS (Short Message Service) has become an ideal means to wirelessly manage a Healthcare environment and in particular PACS (Picture Archival and Communications System) data. SMS is a flexible and mobile method for real-time access and control of Healthcare information systems such as HIS (Hospital Information System) or PACS. Unlike conventional wireless access methods, SMS mobility is not limited by the presence of a WiFi network or any other localized signal. It provides a simple, reliable yet flexible method to communicate with an information system. In addition, SMS services are widely available for low costs from cellular phone service providers and allows for more mobility than other services such as wireless internet. This paper aims to describe a use case of SMS as a means of remotely communicating with a PACS server. Remote access to a PACS server and its Query-Retrieve services allows for a more convenient, flexible and streamlined radiology workflow. Wireless access methods such as SMS will increase dedicated PACS workstation availability for more specialized DICOM (Digital Imaging and Communications in Medicine) workflow management. This implementation will address potential security, performance and cost issues of applying SMS as part of a healthcare information management system. This is in an effort to design a wireless communication system with optimal mobility and flexibility at minimum material and time costs.

Keywords: DICOM, PACS, PDA, SMS, Study Management Tool, Query-Retrieve

2 Introduction

The paradigm of remotely accessing and controlling Healthcare information via cell phone-based SMS has yet to be explored. To illustrate the utility of this paradigm, a system has been designed to perform DICOM Query-Retrieve on a standalone model PACS. Traditionally, the distribution of PACS images in a standalone model PACS would require a user performing DICOM Query-Retrieve operations on a free workstation and waiting for the retrieve operation to complete before being able to view the images. Wireless devices such as PDAs (Personal Digital Assistant) and cell phone-based SMSs have the potential to streamline this process by allowing the user to wirelessly command the PACS to transmit the images to a specified workstation beforehand. [3, 4, 5, 6, 7, 8, 9]These tools are particularly useful when viewing cases that are not normally pre-fetched automatically. In order to elicit key features vis-a-vis security, performance and costs, the design of the aforementioned system has been outlined.

3 Methods and Materials

3.1 System Components

The system can reside on either two separate machines or a single machine. The software components are distributed on both the Web Server as well as the Gateway Server (see Table 1). Both single machine and dual machine configurations were tested. In an attempt to provide a clear distinction between the Gateway and Web server, the systems will be treated as two separate entities connected by an https (hypertext transfer protocol - secure) web link as shown in Figure 1. This design utilizes Kannel Open Source SMS Gateway as the Gateway Server software. The Gateway Server is serially connected to

the SMS modem (MultiModem GPRS Wireless Modem from MultiTech Systems, Mounds View, Minnesota, USA) and communicates via AT commands1. The SMS modem is associated with a GSM (Groupe Spcial Mobile or Global System for Mobile Communications) cell phone account via a SIM (Subscriber Identity Module) card. The phone number of the cell phone account is used as the server access number. On the Web Server machine, a Perl capable web server such as Apache is required. The Perl scripts allow the web server to dynamically create web pages by calling a C++ program that performs the DICOM communications with the PACS archive.

3.2 Standard Workflow

3.2.1 Component Perspective

The standard workflow illustrated in Figure 1 shows how the different components interact with each other. The following steps describe the workflow: In step 1, a standard query will start with the cell phone sending a SMS to the SMS gateway. Steps 2 and 3 shows the gateway accessing a dynamic Perl-based web page from the Web Server via a build-in web client, thus passing-on the query parameters indicated by the user to the perform a DICOM operation. In order to respond back with dynamic data, the Web Server calls a C++ program to perform a DICOM query with the PACS archive in step 4 and 5. The data is then passed back to the user through the web page and SMS gateway. Once the user has found the study of interest, the user can then tell the SMS Gateway to issue a command down the system (steps 2 to 4) to the C++ program, which can then issue a DICOM send command with the desired parameters as indicated in step 6.

Table 2.1: System Components

Gateway Server

Hardware	Software
• Server with Linux OS • Network Connection with Web Server (Optional if on the same Physical Machine)	• Kannel Open Source SMS Gateway

SMS Modem

Hardware	Software
• GPRS Wireless Modem** • Serial Interface to Gateway Server	• Not Applicable

** The author used MultiModem® GPRS Wirless Modem from MultiTech Systems, Mounds View, Minnesota, USA

Web Server

Hardware	Software
• Server with Linux OS • Network Connection with Gateway Server (Optional if on the same Physical Machine) and PACS archive	• Apache Server with Perl Capabilities • C++ Program to interface with PACS archive

3.2.2 User's Perspective

Consider table 2, in a standard workflow the user (1) sends an SMS to the Gateway with a potential patient name. The system then takes the query from the user and performs a query based on the criteria sent, generating output (2) in the form of an SMS reply

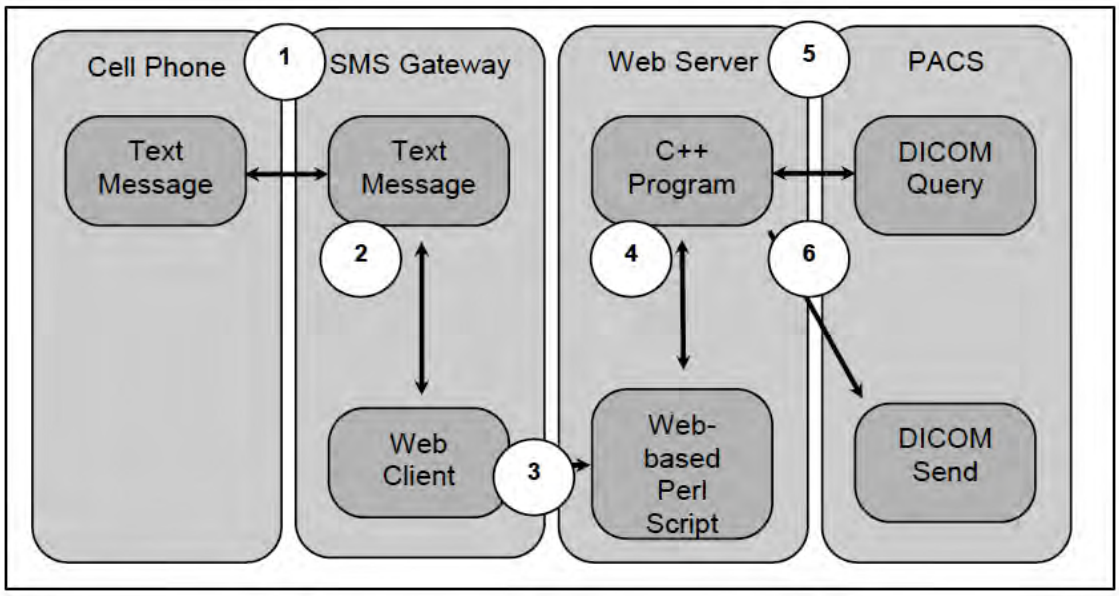

Figure 2.1: Component Interaction Diagram

to the user. To browse the potential matches to the initial query, the user can send two commands n for next page, which sends a request to the gateway to send an SMS with the next set of possible matches, or b to send a query to the gateway to resend the previous choices. In the example, the user does not see the desired patient in the first 4 results and sends n to get the next set of results (see step 3). In (4) , the server returns the next group of results. When the user finds the desired patient Doe, Joe ID number X8787224, the user then sends 8 to select the desired patient (step 5). The server returns the studies associated with patient Doe, Joe together with the examination date. In this case, the server returns two Thorax CTs with its respective date of examination in brackets. Since the user is looking for the examination performed in 1998 and therefore it is appropriate to send the associated index number 2 (step 7). The user is then presented with a list of destinations and as in the previous menu, chooses the desired destination by sending

the number 1 for the EFILM workstation 1 in examination room 1 (step 9). The system has recorded all of the users choices in its cache and sends the appropriate DICOM send command to the PACS archive (see number 5 in figure 1 or section 2.2.1). To confirm that the command has been sent successfully, the SMS gateway responds with a confirmation SMS in step 10. The system is now ready to accept a new query and has cleared the users cache of the previous data.

3.2.3 Background Processes

To be able to perform a full DICOM-query and direct a specified study to a destination via DICOM send, the state of the user must be tracked. In other words, the server must be able to track the input associated with user so as to give the user the appropriate options to choose from. This process is necessary because no session is kept on the user. The users choices and data is stored in the users cache which is associated with the users cell phone number as detected by caller ID. The users state is indicated by the state diagram (see figure 2), the cache is updated every time the user state changes. Each row of table 2 is associated with a single state indicated by a number in figure 2. The arrows shows how the user moves from one state to another. For example, to move from state 1 to state 2, the user has to send a patient name. From state 2 to 3, the user sends a number that associated the desired patient. The user is also able to send another Name or patient name while in the patient state, which will elicit another list of possible patient matches as seen in output 2 in table 2.

Table 2.2: Sample User - Server Interaction: Send Patient Doe, Joe (Patient ID: X8787224)s Chest CT from February 1998 to EFILM workstation in Exam Room 1.

User's Cell Phone -> SMS Gateway	SMS Gateway -> User's Cell Phone
(1) Send Patient Name Query: Doe	(2) Select Patient: 1) Doe, John (X123456) 2) Doe, Jane (X227645) 3) Doe, David (X229884) 4) Doe, Mary (X8787834) n) next
(3) Get Next Page of Results: n	(4) Select Patient (continued): 5) Doe, Jacob (X123226) 6) Doe, Chelsea (X222245) 7) Doe, James (X222284) 8) Doe, Joe (X8787224) n) next b) back
(5) Select Patient of Interest: 8	(6) Select Study: Doe, Joe (X8787224): 1) Thorax CT (01.02.96) 2) Thorax CT (02.02.98)
(7) Select Study of Interest: 2	(8) Select Destination: Doe, Joe (X8787224): 1) EFILM - WS1 (ExamRoom1) 2) Cedara - WS2 (ExamRoom4) 3) CD Burner -WS5 (ExamRoom2)
(9) Select Destination: 1	(10) Confirmation Data: Doe, Joe (X8787224): E-00787981 (02.02.98) -> EFILM : Sent

3.2.4 Other Features

To allow the user to return to the new query menu at anytime, there is a special command 0 that resets the system back to its initial state should the user make any mistakes and

wishes to start over. Other feathers include prefixing the initial query with ID: allowing the user to query by patient ID (see figure 2).

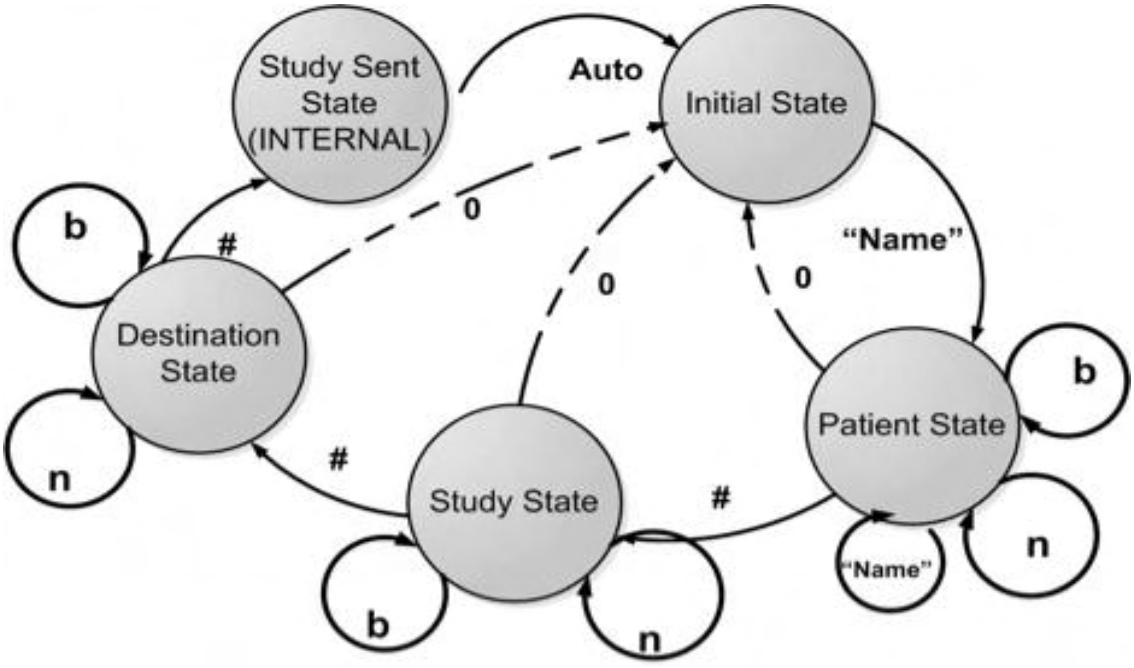

Figure 2.2: The System State diagram shows how the system keeps track of the users selections. This state tracking system allows the user to use the simplistic SMS text-based interface to select the study of interest from the patient of interest to be sent to a designated DICOM node.

4 Results and Discussion

4.1 SMS System Architecture vis-a-vis PDA System Architecture

The SMS system adds the advantage of being able to direct DICOM studies in the PACS archive without being requiring internet or local area network access. The only limitation is a cellular phone carrier signal. It works off the same web server architecture as the PDA system. [9] Therefore, the Web Server for the SMS is identical to the PDA server

except that the generated output is now modified for the SMS, with added functionality to read from a users state tracking mechanism that allows for navigation between the different states (see Figure 2). The limitation of the SMS is that it lacks the previewing capability on the web browser as on the PDA system.

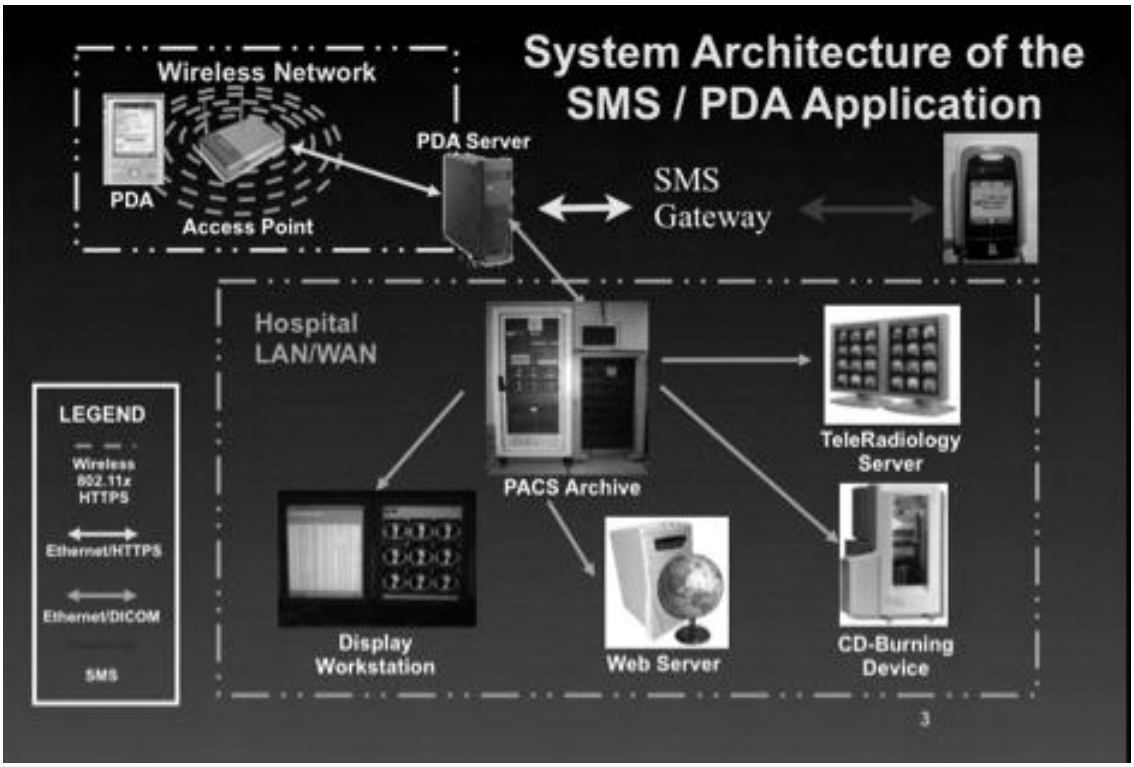

Figure 2.3: The SMS System Architecture is a powerful extension of the existing PDA System Architecture, allowing any authorized user with a cellular phone to direct DICOM images within the Hospital network.

4.2 System Performance

The average turn around time for a SMS command and a reply from the gateway was measured to be 15-20 seconds. However, users noted that turn-around time depended on cellular network congestion. Therefore, the navigation through the three states is

on the order of 2-3 minutes provided that the query does not yield too many possible matches. The system was tested with the PDA server and SMS gateway server on the same machine.

4.3 System Security

If the SMS gateway needs to be in a separate machine its communication with the PDA server is via https, a secure protocol. The SMS gateway only allows queries of 3 types of information: Patient Name, Patient ID and Study Information. This ensures that minimal patient demographic information can be extracted from the PACS archive. Moreover, the SMS gateway does not allow transfer of images outside of the pre-designated list of access-protected destinations. The system can also allow or disallow user-access based on the users phone number.

4.4 User Preferences

Since the users states are tracked internally, the system allows the administrator to set user preferences such as authorized destinations. Other possible user-based preferences could include user customized filters during searches, or a preference to search only by Patient ID.

4.5 Interface Usability

Referring to Table 2 above, it shows the complete workflow to perform a retrieve on a study. The user only has to enter a number at each step following the initial query by patient name. The only latency in the system is waiting for the server reply, which is about 15 seconds depending on cellular phone network congestion. For a large PACS archive,

the screen size and limited number of characters of the SMS protocol becomes a severe limitation when querying with common last or first names only. One way to overcome this problem is to use query by patient ID. Otherwise, the system is user friendly and requires simple inputs of numbers to make necessary choices.

4.6 System Component and Operation Costs

The system runs autonomously after setup and therefore should require minimal maintenance. Since the system can be run from a single machine, the hardware costs are relatively low. Moreover, the scripts and web server does not put a heavy load on the CPU or RAM, therefore the minimum hardware requirements are sufficient. The cost of the modem is also relatively low at about USD $300. Thus, the main burden lies in the cellular phone subscription plans. Most normal cellular phone plans can be used and usually gives 3000 SMS and 5 cents for each additional SMS received and transmitted a month for about USD $60.00. However, large hospitals may consider a fixed rate plan with a cellular provider due to their high volume.

5 Conclusions and Future Work

5.1 Future Work

5.1.1 User Authentication

An additional authentication step is required to ensure proper access protection to the SMS system. This can be easily implemented as extra user authentication state (see figure 2). The user will send an SMS with a password that will be authenticated against the origin (user) phone number.

5.1.2 Hospital Information System (HIS) / Laboratory Information System Applications (LIS)

Potential other use cases of such a system could include retrieving patient data from HIS and LIS, provided ways of circumventing HIPAA requirements are found.

5.1.3 Multimedia Capabilities

With the advent of 3G (Third Generation) cellular technologies such as video streaming and higher bandwidth data connections with cellular networks, it is possible that DICOM images can also be relayed in the same manner as the SMS messages through the use of MMS or Multimedia Messaging Service. One of the destinations in our system could be to the users cellular phone. This would enable the user to see images on the cellular phone display. Possibilities of features such as Window / Level and Zoom / Pan are possible but may be limited by the processing power of the cellular phone. Display resolution is another concern that needs to be addressed.

5.2 Conclusions

The SMS protocol provides an easy and simple way to deploy an application that can manage the DICOM workflow without being constrained by networking requirements. It complements the PDA technology by providing the user with a simpler interface with less network and bandwidth requirements. This paper shows that although SMS is a text-only communication tool, it can allow a user to perform tasks on a PACS network wirelessly. What remains is to see how receptive physicians and technologists are to such a method of streamlining their workflow. However, certain tasks and workflow scenarios will lend

itself more to SMS-based wireless control. For example, tasks such as CD burning of studies through a CD burning DICOM node would be well suited for this system.

SMS-based management of PACS workflow is only one potential application of this system. There are potentially a large variety of use cases for SMS in healthcare information management. Certainly, text-based laboratory information could easily be transmitted over SMS. Application of MMS to transmit images may open up greater possibilities in the realm of image-based information.

Chapter 3

RadSearch: A RIS/PACS Integrated Query Tool

Sinchai Tsao[a], Jorge Documet[a], Paymann Moin[a], Kevin Wang[a], Brent J. Liu[a]

[a] Image Processing and Informatics Lab, Department of Radiology, ISI/USC, Marina Del Rey, CA USA 90292;

Medical Imaging 2008: PACS and Imaging Informatics, edited by Katherine P. Andriole, Khan M. Siddiqui, Proc. of SPIE Vol. 6919, 691909, (2008) 1605-7422/08/$18 doi: 10.1117/12.772983

1 Abstract

Radiology Information Systems (RIS) contain a wealth of information that can be used for research, education, and practice management. However, the sheer amount of information available makes querying specific data difficult and time consuming. Previous work has shown that a clinical RIS database and its RIS text reports can be extracted, duplicated and indexed for searches while complying with HIPAA and IRB requirements. This projects intent is to provide a software tool, the RadSearch Toolkit, to allow intelligent indexing and parsing of RIS reports for easy yet powerful searches. In addition, the project aims to seamlessly query and retrieve associated images from the Picture Archiving and Communication System (PACS) in situations where an integrated RIS/PACS is in place – even subselecting individual series, such as in an MRI study. RadSearchs application of simple text parsing techniques to index text-based radiology reports will allow the search engine to quickly return relevant results. -This powerful combination will be useful in both private practice and academic settings; administrators can easily obtain complex practice management information such as referral patterns; researchers can conduct retrospective studies with specific, multiple criteria; teaching institutions can quickly and effectively create thorough teaching files.

Keywords: NLP, PACS, RIS, Data Mining, Radiology, Radiology Reports

2 Introduction

2.1 Previous Work

Previous work has shown that a RIS database can be searched and radiology report text can be parsed and indexed. Desjardins and Hamilton showed that radiology reports can be

extracted and indexed with minimal disturbance of the clinical workflow while complying with HIPAA and IRB requirements. Current trends in improving standards in Radiology Reporting as well as current practices of report voice recognition dictation using standard templates demonstrate predictability in the location of information within the format of the radiology report. Classification tools such as Index Medicus (IM), Medical Subject Headings (MeSH), International Classification of Disease (ICD), Systematized Nomenclature of Medicine (SNOMED), Unified Medical Language System (UMLS) and RadLex are built to classify large volumes of medical literature for easy searching. RadSearchs end goal is to apply the same concept to Radiology Reports within the RIS.

2.2 RadSearch Toolkit

The toolkit builds upon current functionalities in previous work by (1) parsing the radiology report intelligently into multiple clinically relevant subsections (2) linking the search results to PACS studies. This will enable administrative users of the toolkit to track referral patterns, perform receiver operating characteristic (ROC) analysis, and track billing codes for studies. The toolkit also allows researchers to easily perform large, complex retrospective PACS-based studies by querying for one or more study indications, findings, impressions, diagnostic codes or any other indexed criteria. Finally, the RadSearch toolkit allows educators to easily compile interesting cases and quickly assemble teaching files. In short, RadSearch will enhance radiological informatics support for three main groups: Administrators, Researchers, and Educators.

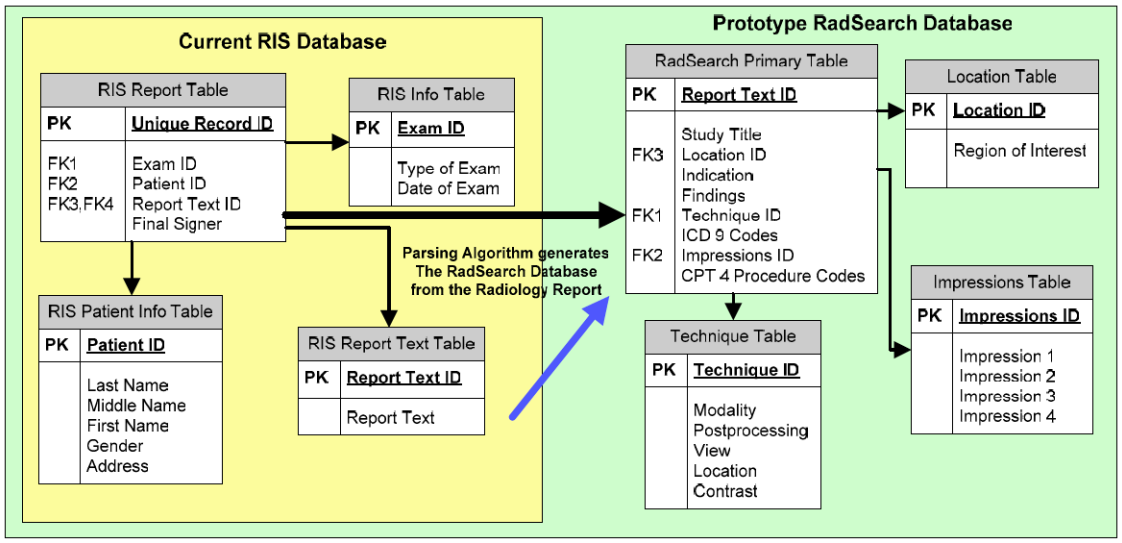

Figure 3.1: Prototype Database Schema

3 Methods

3.1 Natural Language Processing (NLP) -based Approaches

There have been numerous approaches to the data mining Radiology Text information in the RIS database. Taira et al. , Friedman et al. as well as other groups have approached the problem by classification for the specific type of Radiology Reports such as Chest X-rays or Mammograms using Natural Language Processing Techniques. Leximer, a NLP engine at Massachusetts General Hospital, went further to describe referral trends by classifying pathological findings. Nuance Inc. the company behind Leximer, also offers applies similar techniques to improve billing by NLP-based classification of billing codes. However, there have yet to be a tool that allow for generalized searches of the RIS database for teaching file generation or retrospective studies that also have PACS integrated image retrieval.

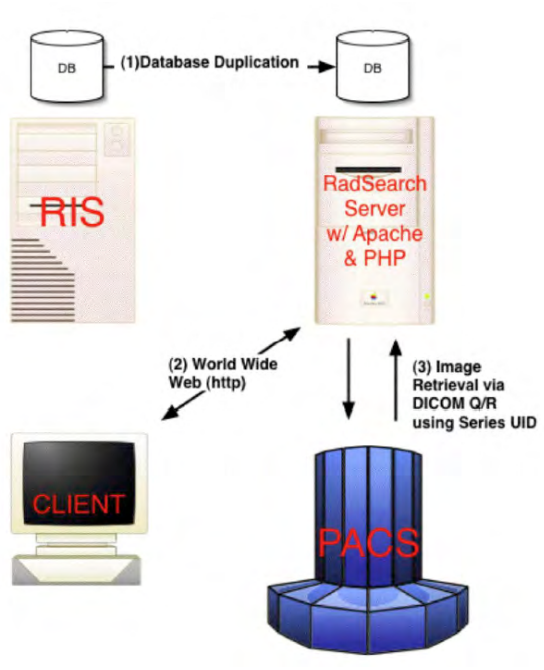

Figure 3.2: Overall System Diagram

3.2 Lexicons and Synonymity

Current work have also concentrated in including synonymity and uniformity to searches of Medical Literature (Journals and other publications) using thesauruses such as Unified Medical Language System or Radiological Society of North America (RSNA)s RadLex (Radiology Lexicon) for Radiology. These lexicons can just as easily be employed in Radiology Report searches and can be achieved in two ways. (1) Using the lexicons as a pure thesaurus, therefore searching of one specific term will search for all related terms. (2) Pre-Classification of the text with specific unified key terms for specific sub-headings and convert all queries to use those key terms. The later approach has advantages with increased search speed and accuracy since the text data can be indexed using those key terms.

3.3 RIS/PACS Integration

Integrated PACS/RIS solutions have shown that it is possible to link RIS radiology reports back to PACS image series using the Series Instance UID portion of the RIS radiology report table. However, none of the current tools allow RIS data mining techniques with PACS integration.

4 Results

4.1 System Architecture

The system is developed utilizing a SUSE linux box running a postgreSQL database as well as an Apache web server with PHP enabled. It employs current PHP scripting technology to perform database manipulations as well as to display results via a web interface. Advantages to using this architecture is that server-side scripting languages such as PHP do not require a compilation step and have an easy to use interface with html for displaying results on the web. PACS connections will be run using the open-source DCMTK toolkit executables called by PHP scripts.

4.2 Radiology Text Report Parsing

The current system has links from the RIS database to a text file that contains the Radiology reports. Our goal is to breakdown the RIS text into broad fields such as: Study Title, Location, Indications, Findings, Technique and Impressions. We can then index the database based on these subsections. This allows the users to make more precise searches based on the aforementioned fields. An initial parsing algorithm employs a simple method of detecting each of the subtitles and parsing the text into each of

the subsections. Subsections not detected is left null. The detected values are then populated into the database and indexed for expedited searching. The PHP scripts will handle both the retrieval of the text file containing the Radiology Text report, parsing, as well as population back into the database using the proposed schema in figure 1. Future advanced Natural Language Processing algorithms can be applied to enhance and improve the parsing step further and, thus improve the overall performance of the toolkit.

4.3 Forming Queries

Queries to the system is formed by specifying key terms for each of the subfields indicated in figure 1. This can include patient demographic data as well as information contained within the Radiology Report. The results will then be returned in the form of a list of Radiology Reports that matched that query along with links to related images.

4.4 Integration with PACS and as a Study Management Tool (SMT)

RadSearch builds upon our current real time patient dashboard [10], which tracks the status of current patients wait time and status within the radiology workflow. It warns clinicians and technicians if the patient has been waiting a long time or if the study hasnt been read after a certain duration past study completion. The patient dashboard does this via its real ime connection with the clinical RIS database and understanding of how and when the RIS database is updated throughout the workflow. RadSearch, therefore, builds upon this understanding to construct a query tool for the same set of database information. Data mining for the patient wait times, time from study completion to reading by a radiologist and other matrices is also possible since it resides on the same database system. PACS integration comes in when the user decides to view images related

to the desired Radiology Report. PACS images are query-retrieved and displayed in a presentation state (JPEG) as specified in the DICOM convention for WADO (Web Access for DICOM Objects). The system can also function as a study management tool that allows the images to be moved via DICOM standards to other DICOM nodes for CD burning, display on a PACS workstation, etc. This is done via the Series Instance UID attached to the desired Radiology Report. The Series Instance UID allows the RadSearch server to query-retrieve all series images from the PACS for the user or initiate a DICOM C-MOVE to move images to another DICOM node.

4.5 System Operation Considerations

To minimize disruption of the clinical RIS system, the system database is duplicated to a postgres SQL database on the RadSearch Server. The system will have weekly duplication sessions during non-peak times such as Sunday nights. PACS connections and query-retrieval will be based on an as-needed basis and should not effect the current clinical operations of the PACS system. Early uses of the system are limited to teaching file generation. IRB approval for use as a retrospective clinical research tool will be implemented when the system has been tested for reliability. User authentication as well as usage logging is also implemented to ensure HIPAA and IRB compliance.

5 Discussion

5.1 RadSearch versus other RIS Data Mining Approaches

RadSearchs approach differs from the other approaches in two folds (1) RadSearch includes PACS integration (2) RadSearch allows for higher specificity in the Radiology Report by

parsing the report into subsections. PACS integration is essential as it allows the user to preview the desired images on the same interface as the RIS search engine. Previously, the user would have to obtain the patient name or ID from the search interface and search for it within the PACS via a PACS workstation before being able to determine if those images are what the user is looking for. With PACS integration, RadSearch will allow the user to seamlessly preview the images together with the list of potential Radiology Reports. Ability to search within specific fields is also important, as the appearance of a term in one subsection of the report may have different meaning than if it appeared within another subsection. Therefore, this ability to search within subsections will improve specificity, accuracy and quality of the user query.

5.2 Future Work

We intend RadSearch to be a platform for future work. The next obvious step is to use a Lexicon to build a classification engine so as to allow for synonimity in searching. We plan to integrate the RadLex lexicon system, since it is build specifically for Radiology. Other possibilities include classification of findings, techniques and indications in the examinations to allow for statistical data mining.

Part B

Functional Neuroimaging

Chapter 4

Application of fMRI to Obesity Research: Differences in Reward Pathway Activation measured with fMRI BOLD during Visual Presentation of High and Low Calorie Foods

Sinchai Tsao[a] Tanja C. Adam[b] Michael I. Goran[c] and Manbir Singh[a,d]

[a]Department of Biomedical Engineering, Viterbi School of Engineering, University of Southern California, Los Angeles, California, USA
[b]Department of Human Biology, Maastricht University, 6200 MD Maastricht, Netherlands
[c]Department of Preventive Medicine, Keck School of Medicine, University of Southern California, Los Angeles, California, USA
[d]Department of Radiology, Keck School of Medicine, University of Southern California, Los Angeles, California, USA

Medical Imaging 2012: Biomedical Applications in Molecular, Structural, and Functional Imaging, edited by Robert C. Molthen, John B. Weaver, Proc. of SPIE Vol. 8317, 83170B
 CCC code: 1605-7422/12/$18 doi: 10.1117/12.911854

1 Abstract

The factors behind the neural mechanisms that motivate food choice and obesity are not well known [31, 32]. Furthermore, it is not known when these neural mechanisms develop and how they are influenced by both genetic and environmental factors. This study uses fMRI together with clinical data to shed light on the aforementioned questions by investigating how appetite-related activation in the brain changes with low versus high caloric foods in pre-pubescent girls. Previous studies have shown that obese adults have less striatal D2 receptors and thus reduced Dopamine (DA) signaling leading to the reward-deficit theory of obesity[33, 34]. However, overeating in itself reduces D2 receptor density, D2 sensitivity and thus reward sensitivity. The results of this study will show how early these neural mechanisms develop and what effect the drastic endocrinological changes during puberty has on these mechanisms. Our preliminary results showed increased activations in the Putamen, Insula, Thalamus and Hippocampus when looking at activations where High Calorie > Low Calorie. When comparing High Calorie > Control and Low Calorie > Control, the High > Control test showed increased significant activation in the frontal lobe. The Low > Control also yielded significant activation in the Left and Right Fusiform Gyrus, which did not appear in the High > Control test. These results indicate that the reward pathway activations previously shown in post-puberty and adults are present in pre-pubescent teens. These results may suggest that some of the preferential neural mechanisms of reward are already present pre-puberty.

Keywords: fMRI, MRI, Obesity, Reward Pathway, Food, Dopamine

2 Introduction

The factors behind the neural mechanisms that motivate food choice and obesity are not well known [31, 32]. Furthermore, it is not known when these neural mechanisms develop and how they are influenced by both genetic and environmental factors. This study uses fMRI together with clinical data to shed light on the aforementioned questions by investigating how appetite-related activation in the brain changes with low versus high caloric foods in pre-pubescent girls. Previous studies have shown that obese adults have less striatal D2 receptors and thus reduced Dopamine (DA) signaling leading to the reward-deficit theory of obesity[33, 34]. However, overeating in itself reduces D2 receptor density, D2 sensitivity and thus reward sensitivity. Moreover, Killgore et al's studies have shown that affective also effects the stratal activation in the brain [35, 33], suggesting that a numerous temporary inputs and more permanent factors such as body weight [36, 37, 38] could modulate the reward center. In this study we aim to use this fMRI techniques to measure differential activations due to the visual presentation of High Calorie (HC) and Low Calorie (LC) foods to prepubescent children. The motivation was to investigate these responses in the youngest population possible before factors like decreased Insulin Sensitivity sets in. The hope is that differences found will be due to responses that is affecting their obese status and not secondary to the adiposity. Furthermore, the presence of these differential responses in the pre-pubescent populations and investigation of potential treatment or weight management techniques will allow us to find out whether the endocrinological changes during puberty solidifies the pathology in terms of neural pathways and responses.

3 Methods

3.1 Participants

13 obese girls between the ages of 8 and 11 were selected to participate in this fMRI and clinical study. 3 of the studies were rejected because of either low fMRI data quality due to movement or violation of clinical protocol in measuring parameters such as Fasting Insulin. The remaining 10 girls had a mean age of 9.90 years and a standard deviation of 1.20 years. Their mean weight was 59.30 lbs with a standard deviation of 13.43 lbs. Their mean height was 144.06 cm with a standard deviation of 7.12 cm.

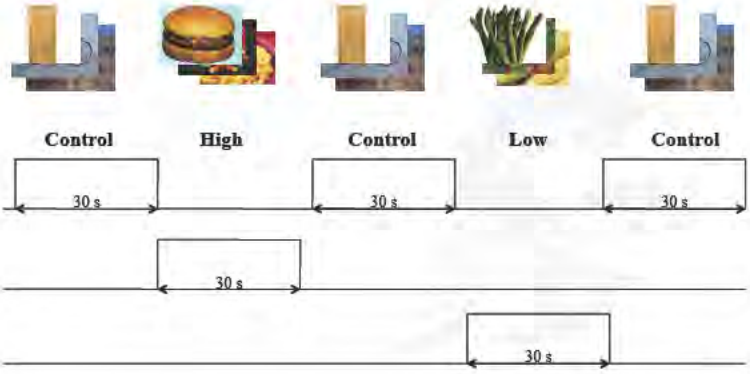

Figure 4.1: fMRI visual stimulus presentation paradigm as presented through the head coil mirror to a projection screen at the foot of the subject. All images were based on previous studies or through the International Affective Picture System. The first three box car functions below the images refer to the three stimulus reference functions for NF/Control, HC and LC respectively.

3.2 Procedures

This study was approved by the University of Southern California IRB committee. After informed consent by the subject and their parents, the subjects were required to participate in two separate visits. The first visit was for anthropometric and body composition measurements followed by an overnight stay and a Frequently Sampled Intravenous Glucose Tolerance Test (FSIVGTT). The second visit was for the neuroimaging study outlined in the next section. A pediatric health care provider conducted a medical history and physical examination together with a determination of maturation using the citeria of Tanner [39]. Body composition for all subjects was measured with dual-energy x-ray absorptiometry (DXA) using a Hologic Discovery A model (82702, Hologic, Bedford, MA).

3.3 MRI Protocol

An fMRI study (TR= 3000 ms, TE = 25 ms, Slice Thickness = 5 mm, Number of Slices = 33, Acquisition Matrix = 64 x 64, Voxel Size = 3.4375 x 3.4375) was performed on each participant and consisted of presenting sets of 10 randomized images of High Calorie (HC) Foods, Low Calorie (LC) Foods and Control Non-Food (NF) Images. The visual stimulus was presented using the PsychToolbox for MATLAB [40] to ensure accurate timing. The visual stimulus was an alternating set of NF, HC, NF, LC, NF images (Figure **??**). Each group of images were randomized to make sure that the results were not due to the effect of any single image but the average of the set as a whole. Anatomical images using T1 FSE and FSPGR sequences were also acquired. All data was acquired on a GE 3T HDxT scanner located at University of Southern Californias Health Consultation Center II.

3.4 SPM Post-processing

SPM8 was used to process the fMRI data. The data was first motion corrected then co-registered to it's corresponding T1-weighted FSPGR image. The T1-weighted FSPGR images are then normalized to an MNI template. This transformation was then applied to the motion-corrected fMRI images. The ROIs were extracted using the Anatomical Labeling Toolkit for SPM [1] .

Table 4.1: Results when comparing High Calorie > Control ordered by z score with Talairach Atlas Coordinates and the Automatic Labeling of the ROIs was done using AAL toolkit for SPM [1]

Regions of Activation	x	y	z	z score
L. Cerebelum Crus I	-26	-88	-26	3.33
L. Fusiform	-42	-50	-18	3.27
R. Frontal Middle	32	50	32	3.07
L. Fusiform	-38	-68	-16	3.02
L. Cerebelum Crus I	-46	-76	-22	3.02
L. Occipital Middle	-30	-84	6	2.99
R. Fusiform	28	-68	-8	2.59

4 Results

Our preliminary results showed increased activations in the Putamen, Insula, Thalamus and Hippocampus when looking at activations where High Calorie > Low Calorie. When comparing High Calorie > Control and Low Calorie > Control, the High > Control test

Table 4.2: Results when comparing Low Calorie > Control ordered by z score with Talairach Atlas Coordinates and the Automatic Labeling of the ROIs was done using AAL toolkit for SPM [1]

Regions of Activation	x	y	z	z score
L. Frontal Superior	-22	22	54	3.57
R. Frontal Superior	14	28	54	3.16
R. Cerebellum Crus I	24	-84	-24	2.92
R. Frontal Middle	30	14	54	2.80
L. Cerebelum Crus I	-16	-86	-28	2.73
L. Occipital Inferior	-50	-78	-12	2.55

showed increased significant activation in the frontal lobe. The Low > Control also yielded significant activation in the Left and Right Fusiform Gyrus, which did not appear in the High > Control test.

5 Discussion

Our preliminary results show that the differential activations detected by numerous previous studies [41] are also present in children. This is important because the end goal of the study is to determine how factors such as Insulin Sensitivity, Fasting Insulin levels and Body Composition are driving forces behind the development of obesity. Obese adults tend to have a low range of insulin sensitivity and therefore make investigating the relationship between brain reward and insulin sensitivity difficult. However, with obese children they still retain a large range of insulin sensitivity [42]. The hypothesis

is that insulin as a neurotransmitter plays a crucial role in regulating the reward centers in the brain and therefore a loss in insulin sensitivity will cause subjects to be unable to manage visual food stimulus appropriately. In other words, the loss of insulin sensitivity means that the patient will be unable to temper food stimulus appropriately leading to overeating and obesity. Previous work has shown to be consistent with this hypothesis [42, 43, 44, 45]. Most of the insulin receptors in the brain lie within the limbic region, our preliminary results show that a differential in activation occurs when the subjects are stimulated with high versus low calorie foods lie within the limbic regions (see Table 4.3). This coupled with preliminary clinical data indicating that our subjects have a wide range of insulin sensitivity suggests that it may be possible to correlated the degree of differential activation with each subject's insulin sensitivity. Furthermore, our study also collects body adiposity measurements, which have been known to be a factor in insulin resistance. Our current hypothesis suggests that insulin sensitivity may be an earlier precursor to body adiposity due to it's neurotransmitter role in the limbic system. This hypothesis can be tested by carefully controlling for body adiposity in our study thus showing that perhaps insulin sensitivity and not body adiposity is the culprit in mis-regulation of visual food stimulus in the obese.

6 Conclusion

Our study shows how we are able to extend traditional fMRI studies to investigate pathological neurological pathways in the obese. This example simply shows that if clinical parameters such as insulin sensitivity and adiposity can be incorporated into fMRI image analysis, a large range of clinical hypothesis can be tested. This study outlines the initial

steps of this type of analysis. These initial steps are important in establishing that the responses that we are correlating are indeed in areas that are related to the pathway in question. In our case, multiple parts of the limbic region and other brain reward areas were found to be significant in our High > Low Calorie analysis. These regions did not appear to be significant in our High > Control and Low > Control comparisons indicating that these regions are indeed involved only in differentiating between low and high visual food stimulus [41].

This paradigm of combining traditional clinical studies of pathologies such as obesity with fMRI techniques have traditional used only for primary neuroscience research but can easily be applied to a variety of disorders, obvious targets include Alzheimer Disease and Mildly Cognitively Impaired. Other applications include relating the change in fMRI activity with therapeutic outcomes and treatments.

ACKNOWLEDGMENTS

The authors would like to acknowledge the help of Kori Wong Kazama Tsao for her clinical psychology expertise in handling the anxiety of the young female subjects in the MRI. Darryl H. Hwang for his help in the operation of the MRI as well as handling of subjects. Kathleen A. Page for introducing the authors and her contribution to the use of fMRI in Obesity Research. Houchun Harry Hu for developing the initial version of the fMRI visual stimulus. Samuel Valencerina for his help with the operation of the MRI at USC. Last but not least, I'd like to dedicate this work to the late Professor Manbir Singh PhD, my mentor, friend and inspiration who's sudden passing this past winter has been

a tragic loss for us all. This work could not have been possible if not for every single one of you.

This study was supported by the National Cancer Institute (U54 CA 116848), a Pfizer Fellowship in Health Disparities awarded to Tanja C. Adam and by National Center of Research Resources (NCRR) grant 1S10RR019942 that provided the 3T MRI used in this study.

Table 4.3: Results when comparing High Calorie > Low Calorie ordered by z score with Talairach Atlas Coordinates and the Automatic Labeling of the ROIs was done using AAL toolkit for SPM [1]

Regions of Activation	x	y	z	z score
R. Temporal Superior	60	-52	24	3.24
R. Frontal Middle	46	18	34	3.11
L. Frontal Medial Orbital	-6	50	-4	3.09
R. Frontal Superior	28	32	48	3.05
L. Frontal Middle	-24	6	48	3.01
L. Precentral / Postcentral	-30	32	62	2.89
L. Frontal Middle	-24	32	42	2.88
R. Hippocampus / R. Thalamus	18	-36	6	2.85
L. Frontal Middle / Superior	-20	20	52	2.82
R. Temporal Superior	58	-18	-2	2.77
R. Putamen / R. Insula	32	-20	0	2.74
Caudate	0	14	-2	2.73
L. Frontal Inferior Opercularis / Middle	-48	16	34	2.63
R. Frontal Middle	30	18	54	2.48

d the neural mechanisms that motivate food choice and obesity are not well known. hen these neural mechanisms develop and how they are influence by both genetic and uses fMRI together with clinical data to shed light on the aforementioned questions by activation in the brain changes with low versus high caloric foods in pre-pubescent girls. obese humans have less striatal D2 receptors and thus reduced Dopamine (DA) signaling theory of obesity. However, density, D2 sensitivity and thus f this study will show how early op and what effect the drastic uberty has on these mechanisms.

se girls between the ages of 8 and n the study. An fMRI study was consisted of presenting sets of 10 ie (HC) Foods, Low Calorie (LC) ges. Each participant's percentage g with body height & weight, hip venous Glucose Tolerance Test x (BMI), Tanner Stage as well as

iminary results showed increased ula, Thalamus and Hippocampus re High Calorie > Low Calorie. > Control and Low Calorie > est showed increased significant The Low > Control also yielded and Right Fusiform Gyrus, which did not appear in the[45] High > Control test.

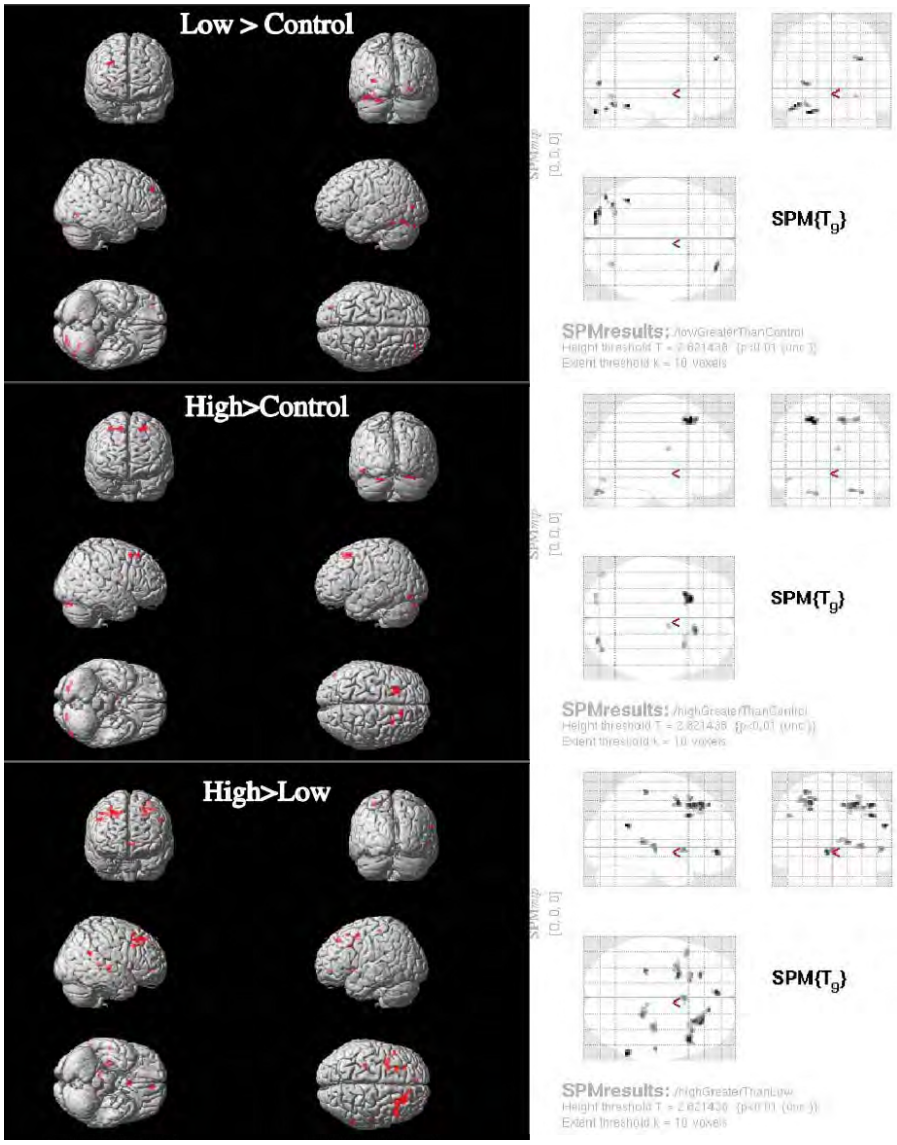

Figure 1. Group statistical parametric map (SPM) comparison of activated areas during presentation of Low Calorie, High Calorie and Control Images ($P < 0.01$, uncorrected) with an extent threshold of 10 Voxels. The SPMs are presented in two ways (LEFT) Rendered onto a single subject's brain (RIGHT) Maximum Intesity Projections (MIP) in three views.

Figure 4.2: Group statistical parametric map (SPM) comparison of activated areas during presentation of Low Calorie, High Calorie and Control Images ($P < 0.01$, uncorrected) with an extent threshold of 10 Voxels. The SPMs are presented in two ways (LEFT) Rendered onto a single subject's brain surface.

For Tables Note:
L. Left Hemisphere
R. Right Hemisphere.
Atlas coordinates x,y,z in mm are from the Talairach and Tournoux (1988) Atlas.
Only regions with z score significant beyond P<0.01 (Uncorrected are shown)

Conclusions: Our preliminary results show that the reward pathway activations previously shown in post-puberty and adults are present in pre-pubescent teens. These results may suggest that the some of the preferential neural mechanisms of reward are already present pre-puberty. We

	z score
4	3.24
4	3.11
4	3.09

Chapter 5

Novel MRI Methodology to detect Human Whole-Brain Connectivity Changes after Ingestion of Fructose or Glucose

Sinchai Tsao[a] Bryce Wilkins[a] Kathleen A. Page [b] and Manbir Singh[a,c]

[a]Department of Biomedical Engineering, Viterbi School of Engineering,
University of Southern California, Los Angeles, California, USA
[b]Department of Internal Medicine, Division of Endocrinology, Keck School of Medicine,
University of Southern California, Los Angeles, California, USA
[c]Department of Radiology, Keck School of Medicine,
University of Southern California, Los Angeles, California, USA

Medical Imaging 2012: Biomedical Applications in Molecular, Structural, and Functional Imaging, edited by Robert C. Molthen, John B. Weaver, Proc. of SPIE Vol. 8317, 83170B
 CCC code: 1605-7422/12/$18 doi: 10.1117/12.911854

1 Abstract

A novel MRI protocol has been developed to investigate the differential effects of glucose or fructose consumption on whole-brain functional brain connectivity. A previous study has reported a decrease in the fMRI blood oxygen level dependent (BOLD) signal of the hypothalamus following glucose ingestion, but due to technical limitations, was restricted to a single slice covering the hypothalamus, and thus unable to detect whole-brain connectivity. In another previous study, a protocol was devised to acquire whole-brain fMRI data following food intake, but only after restricting image acquisition to an MR sampling or repetition time (TR) of 20s, making the protocol unsuitable to detect functional connectivity above 0.025Hz. We have successfully implemented a continuous 36-min, 40 contiguous slices, whole-brain BOLD acquisition protocol on a 3T scanner with TR=4.5s to ensure detection of up to 0.1Hz frequencies for whole-brain functional connectivity analysis. Human data were acquired first with ingestion of water only, followed by a glucose or fructose drink within the scanner, without interrupting the scanning. Whole-brain connectivity was analyzed using standard correlation methodology in the 0.01-0.1 Hz range. The correlation coefficient differences between fructose and glucose ingestion among targeted regions were converted to t-scores using the water-only correlation coefficients as a null condition. Results show a dramatic increase in the hypothalamic connectivity to the hippocampus, amygdala, insula, caudate and the nucleus accumben for fructose over glucose. As these regions are known to be key components of the feeding and reward brain circuits, these results suggest a preference for fructose ingestion.

Keywords: MRI, fMRI, Functional Connectivity, Glucose, Fructose, Obesity, Insulin, Hypothalamus

2 Introduction

The main objective of these pilot studies was to develop a MRI protocol and conduct initial evaluation studies of the differential effects of glucose and fructose ingestion on the feeding pathways in normal (healthy) and obese adults. By identifying brain regions that show differential activity across normal and obese subjects following glucose or fructose ingestion, we hope that the data will permit new understandings of the effects of glucose/fructose ingestion and their implication in obesity. Recent published research [46, 47, 48, 49] has shown that glucose ingestion in healthy humans leads to a decrease in hypothalamic nuclei activity and consequently a decrease in the fMRI blood oxygen level dependent (BOLD) signal. Furthermore, it has been shown that glucose ingestion fails to inhibit hypothalamic nuclei activity in patients with type 2 diabetes[50]. These scans typically require continuous acquisition of fMRI data for a period of about 30-45 minutes, and due to MRI technical limitations, previous research in this area has been restricted to acquisition of fMRI data from a single mid-sagittal slice, covering only the hypothalamus. A fundamental difference in our proposed studies was to design a protocol to obtain fMRI sampling over the entire brain, permitting the detection of glucose/fructose related changes throughout the brain. A successful protocol would then enable us to conduct an analysis of whole-brain functional connectivity following glucose/fructose ingestion. To our knowledge, no such connectivity analysis has been reported previously by any group. Thus, development of a MRI scan protocol for this project, which presents many key technological challenges, was considered an essential first step.

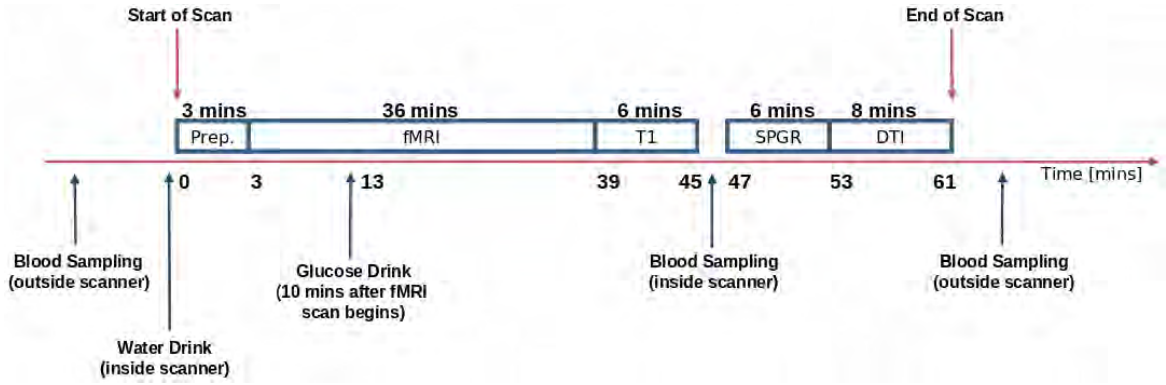

Figure 5.1: Three blood samples are taken during the experiment to track the subjects blood sugar level. The sequence of the individual scans, and times at which blood-sampling occurs, are indicated in the figure above.

3 Methods

3.1 Subjects

This protocol was tested with 4 Hispanic subjects between the ages of 15-25 who have no history of diabetes.

3.2 Protocol Development

The challenge was to develop a whole-brain fMRI protocol with continuous data acquisition for approximately 45 minutes that would include a baseline, a relatively long post-glucose/fructose ingestion period, and a short time for ingesting the glucose/fructose during the scan. Typically a TR of 2 seconds is used in fMRI connectivity studies and for TR=2s, continuous acquisition of 4mm thick images covering the whole brain would require a time-series of 40,500 images. As such long time-series have never been reported before in fMRI and are not allowed by hardware constraints of many scanners, we did several developmental scans to push the technical limits of the USC GE 3T MRI to increase

the number of images that could be acquired in a continuous time-series. It was found that our 3T system could acquire at most 20,000 images continuously before exhausting its current memory capabilities. However during some developmental scans, the gradients overheated and the scans had to be terminated.

We argued that as glucose/fructose were diluted in water during ingestion, it would be important to add a baseline study corresponding to ingestion of water only, so that confounding effects of water could be separated from those attributed to sugar ingestion. We conducted several developmental studies to assess the fMRI signals acquired with water ingestion only and those after ingestion of a sugar drink and came to the conclusion that because all images must be acquired continuously (stopping and restarting a scan is not an option as it changes many parameters including the baseline making an accurate analysis virtually impossible) it was essential to acquire data from a water only period prior to sugar ingestion in the same continuous scan. Incorporating these requirements, we came up with our final 36 min fMRI protocol during which the subject first drinks pure water, followed by 10 min of data acquisition, then drinks water containing glucose (or fructose), followed by about 24 min of data acquisition. Thus the fMRI scan was divided into three regions: a 10 min baseline condition before ingestion of the sugar drink; drink period of 2-4 min; and lastly 22-24 min of post-drink data (see Figure **??**). After several trials, the repetition time (TR) of the fMRI scan was chosen to be 4.5s. This TR is short enough for adequate temporal filtering of the data for functional connectivity analysis, and long enough to enable us to acquire data continuously for 36 min for a total of approximately 19,000 fMRI images. As additional images and time are required for anatomical and diffusion tensor imaging (DTI) analysis, 36 minutes were considered as close to the upper limit for the fMRI portion to finish the entire scan in about one hour.

Immediately following the fMRI acquisition, an anatomical T1-weighted scan is acquired to enable registration of subject fMRI data to an anatomical reference template. This is followed by another higher-resolution (SPGR) anatomical scan that is extensively used to spatially normalize images and delineate small anatomical regions of interest such as the hypothalamus.

Following the anatomical scans a diffusion-weighted data set is obtained in accordance with a standard DTI protocol that we have implemented on this GE scanner. This data may be used to investigate structural connectivity differences between normal (healthy) and obese subjects.

3.3 Data Processing and Analysis of fMRI Baseline Trends

As subjects are bound to move their heads during a relatively long scan and certainly during the drinking period, the first step in processing is to correct the fMRI time-series for head-movements. Each subjects' fMRI data is motion-corrected to the last acquired head-volume, registered to the individuals' high-resolution SPGR anatomical scan, and warped to normalized space through non-linear mapping techniques. The Colin Brain template [51] in Talairach Tournoux coordinates was used to define normalized space in this study though other templates such as the SPM MNI template could also be used. Regions of Interest (ROIs) are derived from the San Antonio Talairach Daemon [52, 53], which is also in the Talairach-Tournoux normalized space.

3.4 Connectivity Analysis

Whole-brain connectivity was analyzed using a standard technique where the movement and slice-timing corrected fMRI data are band-pass filtered (0.01 0.10 Hz), a seed region

is selected and then the time courses of all voxels throughout the brain volume are correlated to the time-course of the seed region to obtain a measure of functional connectivity. An alternative approach is to first define ROIs based on anatomy and then compute the pair-wise connectivity among averaged time-courses of these ROIs. Both methods were pursued. In addition, the resting state default connectivity network was also examined. A methodology was developed to answer the following questions: a) Is there a significant difference between the resting state functional connectivity of the default mode network, which generally shows strong functional connectivity among the posterior cingulate and certain parietal and frontal regions, after ingesting glucose vs. fructose? b) Is there a significant difference between the whole-brain functional connectivity of the hypothalamus after ingesting glucose vs. fructose? c) Is there a significant difference in the pair-wise functional connectivity among specified ROIs after ingesting glucose vs. fructose? To reduce the effects of inter-subject variations, a pair-wise connectivity analysis was conducted after averaging the time-courses in targeted ROIs of 3 subjects who completed the glucose and fructose scans. The fourth subjects drinking times were significantly different to other subjects and as a result data from this subject was not included in the pair-wise connectivity analysis. The selected ROIs included key brain regions previously suggested to be involved in brain feeding and reward circuits. The pair-wise connectivity scores were converted to t-scores by comparing to the water-only baseline connectivities of the same pairs.

4 Results

An example of raw fMRI results from a single subject are shown in Figure 5.2. Due to scanner drift, these signal cannot be interpreted directly. To account for scanner drift we demeaned the signal as shown in Figure 5.3. Using a seed region and time course of the signal before the ingestion of glucose / fructose in the posterior cingulum we were able to derive correlation maps for the default mode / resting state network (see Figure 5.4). After the ingestion of glucose / fructose we again used the same seed region and we were able to qualitative observe changes in the network (see Figure 5.5). We repeated the same procedure but used the hypothalamus as the seed regions in pre-glucose/pre-fructose and post-glucose/post-fructose (see Figure 5.6). To expand the search beyond manual selection of seed regions such as the posterior cingulum and the hypothalamus we used ROIs derived from the San Antonio Talairach Daemon [52, 53] and correlated each of the ROIs with each other as shown in Figure 5.7. The colors on the matrix grid indicate the degree of correlation between the two ROIs. ROIs with t-scores > 2.00 are shown in Table 5.1.

5 Discussion

Examples of the connectivity images obtained from one such subject are presented in Figures 5.4,5.5 showing potential differences in the default network between glucose and fructose ingestion. A correlation threshold of 0.5 was applied. Similar connectivity differences between the hypothalamic ROI and voxels throughout the brain were also noted. As the hypothalamus is composed of just a few voxels and is anatomically located in a region of the brain where susceptibility artifacts are strong, the signal-to-noise ratio in

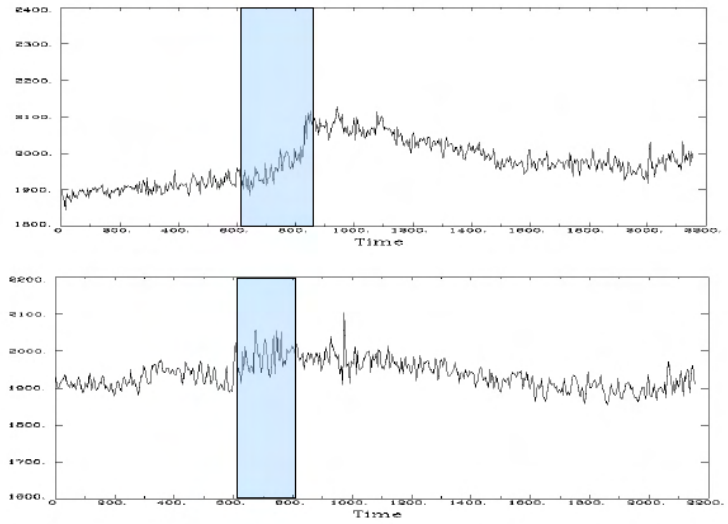

Figure 5.2: The hypothalamic fMRI time-course for a subject showing an initial water-only drink period, the actual drinking period (shaded) followed by either a glucose (top) or fructose (bottom) drink period. Glucose and fructose experiments were done on separate days.

the time-course is not very high. Thus more variation is expected in the hypothalamic connectivity analysis than the default network. The hypothalamic connectivity images are shown in Figure 5.6. Overall it appears that connectivity of several regions is altered post-fructose vs. post-glucose but there were significant inter-subject variations (which is expected).

Though the sample size is very small, the results show a dramatic increase in the hypothalamic connectivity to very specific regions known to be key components of the feeding and reward circuits after fructose ingestion when compared to glucose ingestion. Specifically, an increase in hypothalamic connectivity to the hippocampus, amygdala, insula, caudate and the nucleus accumbens stands out. The largest increase (t-score of 4.5, which means an increase of 4.5 standard deviations with respect to glucose connectivity)

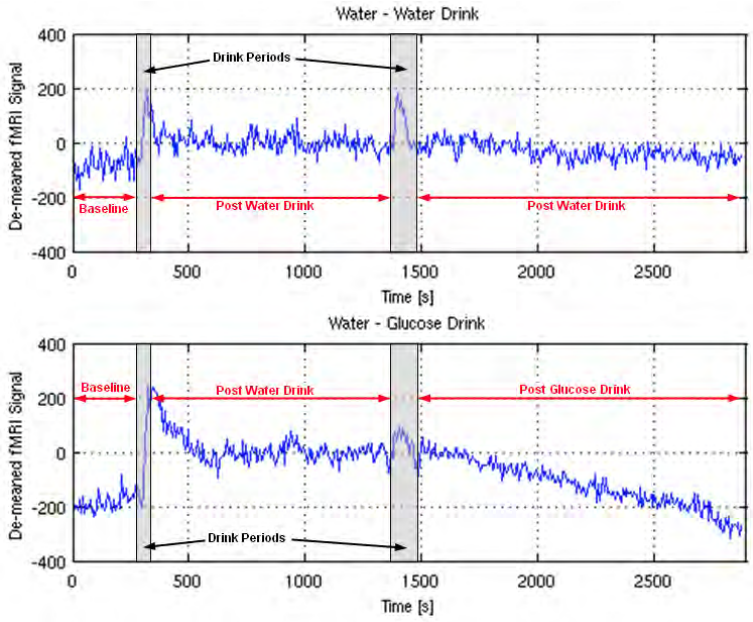

Figure 5.3: (top) The hypothalamic fMRI time-course includes a pre-drink baseline period preceding a water-only drink and then a second water-only drink. The data is de-trended by the first water-only period. (bottom) Same as top except the subject ingested a glucose drink during the second drinking period. The change in baseline trend following glucose ingestion is obvious.

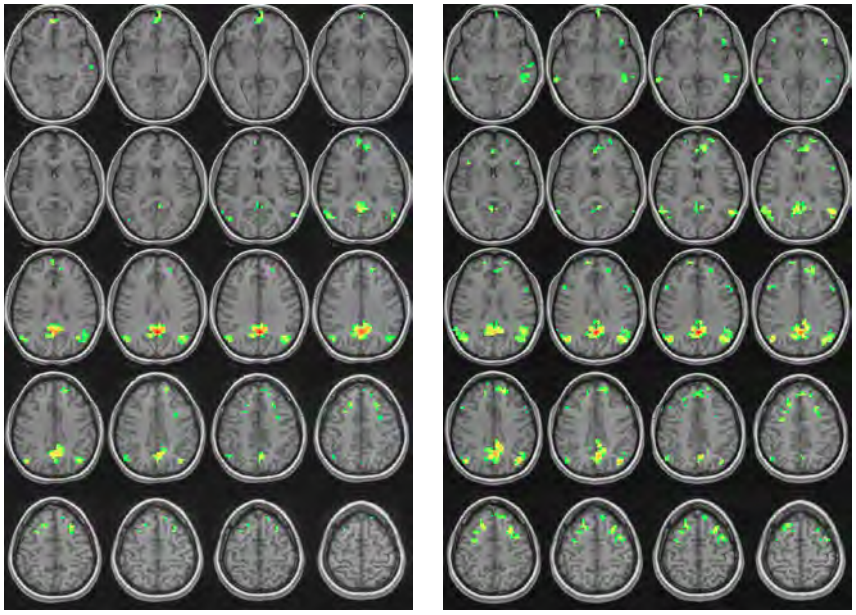

Figure 5.4: The default-mode network in a pilot subject during the pre-glucose (left) or the pre-fructose (right) period. These are expected to be the same but as the glucose and fructose experiments were done on separate days, minor differences can be seen. The default network is clearly identified by our protocol.

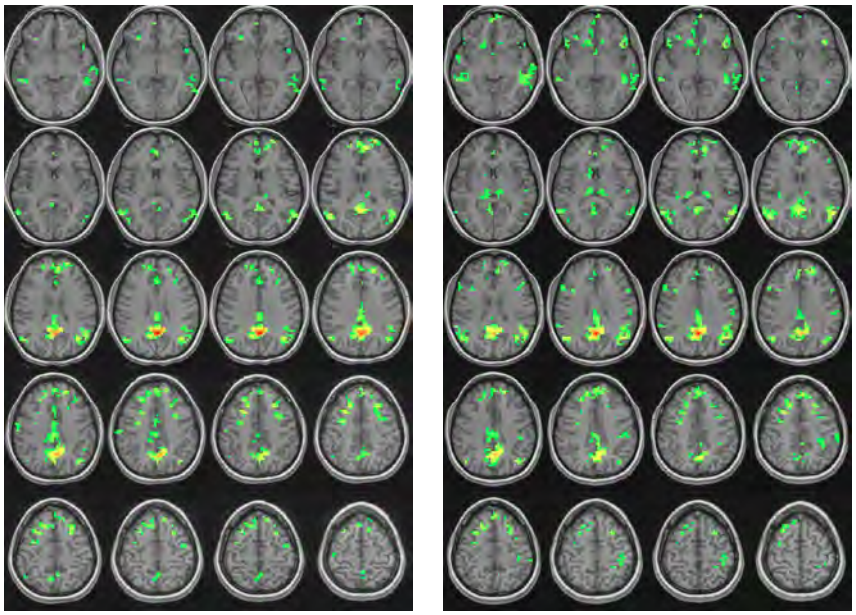

Figure 5.5: The default-mode network in a pilot subject during the post-glucose (left) or the post-fructose (right) period. Several differences can be seen, which need further analysis to interpret their significance.

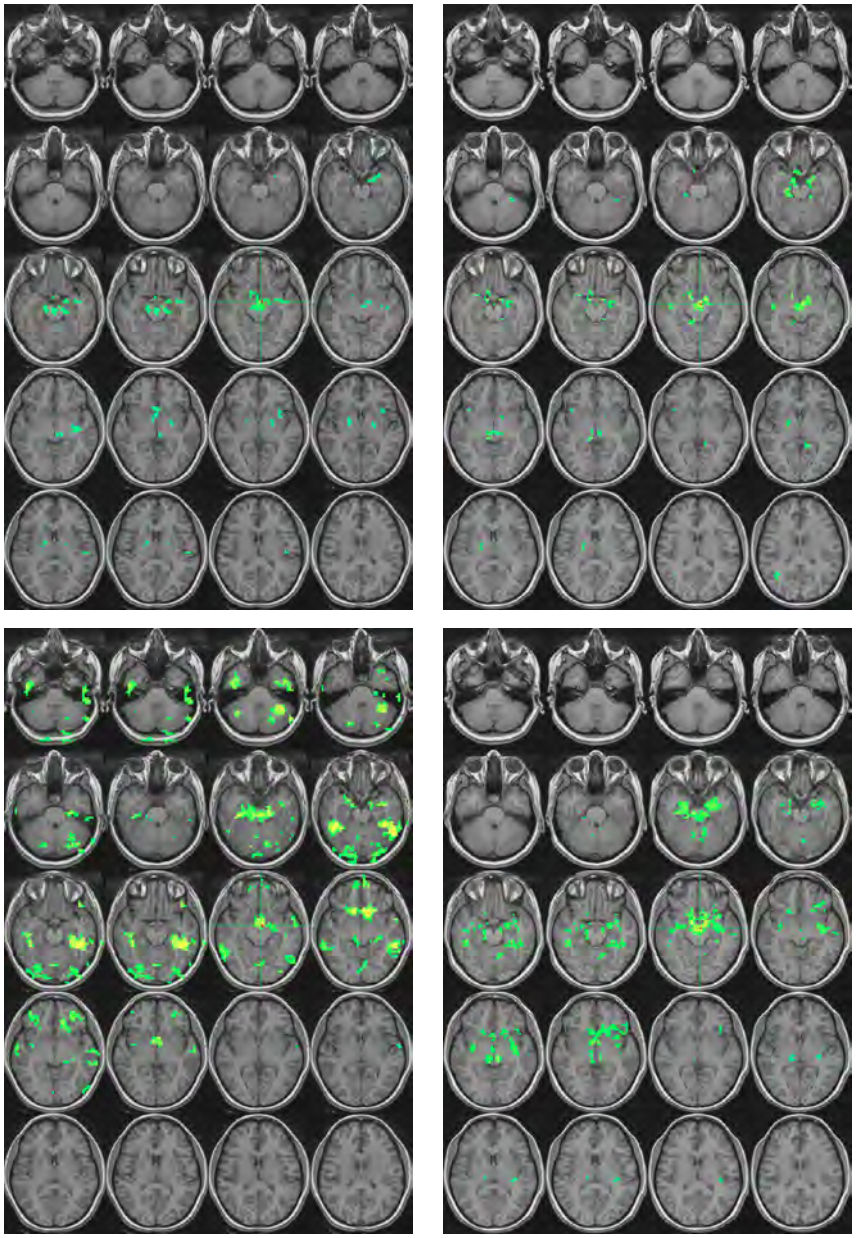

Figure 5.6: The hypothalamic connectivity in a pilot subject during the pre and post-glucose periods (top and bottom left respectively) or the pre and post-fructose periods (top and bottom right respectively).

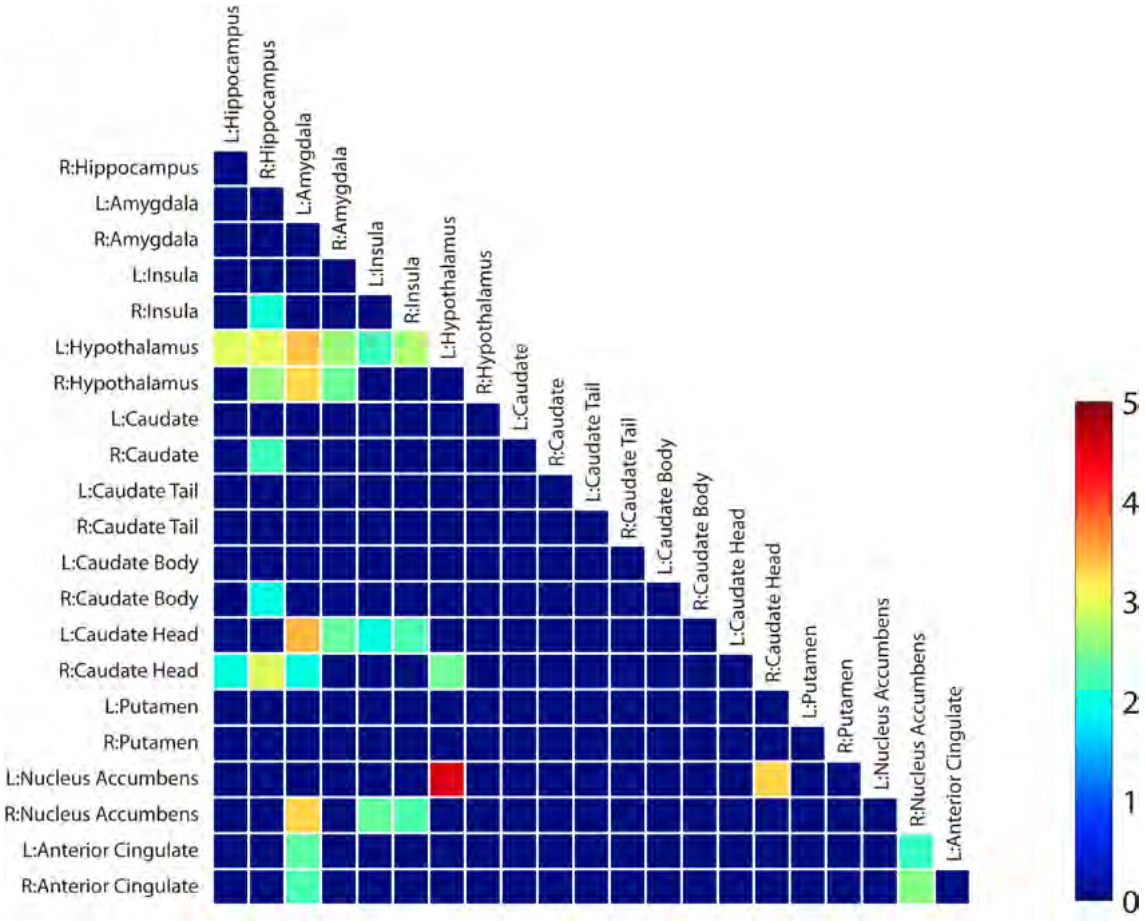

Figure 5.7: Matrix of thresholded t-scores ($t > 2$) from pair-wise functional connectivity between select ROIs averaged over 3 subjects; the color-bar gives the t-score to color mapping. The most prominent connectivity exists between the left hypothalamus and left/right hippocampus, left/right amygdala, left/right insula, right caudate head, and left nucleus accumbens. The highest t-score (4.57) is between the left hypothalamus and left nucleus accumbens.

Table 5.1: t-scores corresponding to the pair-wise ROIs shown in Figure 5.7 that exceed the threshold (t > 2).

ROI 1	ROI 2	t-Score	ROI 1	ROI 2	t-Score
L:Hippocampus	L:Hypothalamus	2.97	R:Insula	L:Caudate Head	2.30
L:Hippocampus	R:Caudate Head	2.02	R:Insula	R:Nucleus Accumbens	2.31
R:Hippocampus	R:Insula	2.08	L:Hypothalamus	L:Hippocampus	2.97
R:Hippocampus	L:Hypothalamus	3.01	L:Hypothalamus	R:Hippocampus	3.01
R:Hippocampus	R:Hypothalamus	2.64	L:Hypothalamus	L:Amygdala	3.41
R:Hippocampus	R:Caudate	2.23	L:Hypothalamus	R:Amygdala	2.68
R:Hippocampus	R:Caudate Body	2.02	L:Hypothalamus	L:Insula	2.22
R:Hippocampus	R:Caudate Head	2.99	L:Hypothalamus	R:Insula	2.76
L:Amygdala	L:Hypothalamus	3.41	L:Hypothalamus	R:Caudate Head	2.46
L:Amygdala	R:Hypothalamus	3.31	L:Hypothalamus	L:Nucleus Accumbens	4.57
L:Amygdala	L:Caudate Head	3.47	R:Hypothalamus	R:Hippocampus	2.64
L:Amygdala	R:Caudate Head	2.03	R:Hypothalamus	L:Amygdala	3.31
L:Amygdala	R:Nucleus Accumbens	3.31	R:Hypothalamus	R:Amygdala	2.45
L:Amygdala	L:Anterior Cingulate	2.36	R:Caudate	R:Hippocampus	2.23
L:Amygdala	R:Anterior Cingulate	2.27	R:Caudate Body	R:Hippocampus	2.02
R:Amygdala	L:Hypothalamus	2.68	L:Caudate Head	L:Amygdala	3.47
R:Amygdala	R:Hypothalamus	2.45	L:Caudate Head	R:Amygdala	2.41
R:Amygdala	L:Caudate Head	2.41	L:Caudate Head	L:Insula	2.05
L:Insula	L:Hypothalamus	2.22	L:Caudate Head	R:Insula	2.30
L:Insula	L:Caudate Head	2.05	R:Caudate Head	L:Hippocampus	2.02
L:Insula	R:Nucleus Accumbens	2.41	R:Caudate Head	R:Hippocampus	2.99
R:Insula	R:Hippocampus	2.08	R:Caudate Head	L:Amygdala	2.03
R:Insula	L:Hypothalamus	2.76	R:Caudate Head	L:Hypothalamus	2.46

is seen for the hypothalamic-nucleus accumbens connection, which is known to be a key component of the feeding circuit. The selected ROIs and their pair-wise connectivity results are shown in Figure 5.7. The t-scores for all ROIs above the threshold of $t > 2$ are listed in Table 5.1. No significant increases in pair-wise connectivity among the selected ROIs were detected for glucose compared to fructose ingestion.

6 Conclusion

After the publication of Liu et al. 2000's Nature article [49], there has been a lot of interest in being able to investigate how brain activity is influenced by food. The tool of choice has been fMRI. Liu et al 2000 showed how the use of the raw fMRI signal without deconvolution of the Hemodynamic Response Function (HRF) can give us repeatable detection of temporal changes in brain activations even though responses from HRF-based analysis can be seen [54, 33]. Recent developments of functional connectivity and better knowledge about the default mode network has given us a new framework from which to investigate the basis of these changes. This paper outlines our initial efforts at attempting to investigate food related functional connectivity changes using the premise that the default mode network somehow modulates these responses.

We know that the default mode network is crucial in our ability to maintain homeostasis [55]. Feeding behavior is one complex component of supplying nutrition to maintain homeostasis and therefore the default mode network should respond accordingly to food stimulus. The question is whether when and where do these stimuluses get translated into neurological pathways that solidify our behavior. In particular, how do these differences in default mode network responses reflect pathological states where the human body is

unable to regulate feeding behavior properly, leading to the development of obesity. To make matters more complex, the causality is unknown. In other words, does the pathological feeding behavior cause the differences in responses or do the responses indicate an underlying condition that causes the pathological behavior. This coupled with the differential activations between fructose and glucose raises a large number of questions about the neurological mechanisms that govern our feeding behavior. To our knowledge, no such results have been reported before and if these results can be verified in a larger study, they would represent a key discovery in how brain connectivity among key regions is altered by fructose compared to glucose ingestion.

With regards to fMRI processing and techniques, this study serves to show that there is still much work that needs to be done to properly understand the results of fMRI studies. The underlying biological mechanisms that lead to the partial correlations in functional connectivity are not well know [55]. Even if we were to be able to find changes that correlate well with parameters such as the ingestion of glucose versus fructose, we are not able to draw definitive conclusions unless the underlying mechanisms are better understood. Current glucose ingestion studies together with studies that use pharmaceuticals alter our homeostatic state [56] will help to elucidate some of these mechanisms. This together with other anthropometric techniques as well as PET studies will further clarify the phenomenon observed in our fMRI studies [54, 33]. Techniques that better utilize the temporal information within the fMRI signal will continue to push the envelope in terms of the information elicited from imaging studies. Functional Connectivity and other techniques will continue to push the evolution of techniques that do not use the HRF. This will hopefully help us establish a better understanding of how each part

of the brain responds vis-à-vis another part of the brain and not just be able to isolate individual activities as predicted by the BOLD HRF.

Acknowledgements

The authors would like to acknowledge Samuel Valencerina for his help with the MRI at USC. Lab-mates Darryl Hwang for helping with the development of the MRI protocol. In particular, his help with the glucose ingestion delivery system. I'd like to dedicate this work to the late Professor Manbir Singh PhD, my mentor, friend and inspiration who's sudden passing this past winter has been a tragic loss for us all. This study was partially supported by National Center of Research Resources (NCRR) grant 1S10RR019942 that provided the 3T MRI used in this study.

Part C

Structural Neuroimaging

Chapter 6

Quantification of Fornix Tracts in MCI and AD

D. H. Hwang[1], S. Tsao[1], and M. Singh[1]

[1] Depts of Biomedical Engineering and Radiology,
University of Southern California, Los Angeles, CA, United States

Proc. Intl. Soc. Mag. Reson. Med. 17 (2009)

1 Introduction

Numerous studies have shown a pattern of progressive hippocampal shrinkage as a result of mild cognitively impairment (MCI) and Alzheimer Disease (AD). One of the major pathways affected by the hippocampus is the fornix, and it has been recently shown that fractional anisotropy (FA) is reduced in normal controls verses AD [DeCarli et al., Alzheimers Imaging Consortium IC-P1,July 2008]. The purpose of this study was to (a) objectively define hippocampal ROIs as most previous studies rely on subjectively delineated ROIs to perform DTI analysis, (b) correct for varying subject head sizes using intracranial volume(ICV) of subjects in a novel way to equalize the number of seed points and their anatomical distribution so that total number of tracts becomes independent of the subject's head size, and (c) examine the differences in the equalized streamline fornix tracts.

Normal MCI AD

Figure 6.1: Normalized Fornix Tracts

2 Methods

Data were acquired on a 3T GE scanner from three groups (10 normal control, 8 MCI, and 7 AD probable) as classified by neuropsychological testing. Multi-slice ($2.04 \times 2.04 \times 4$

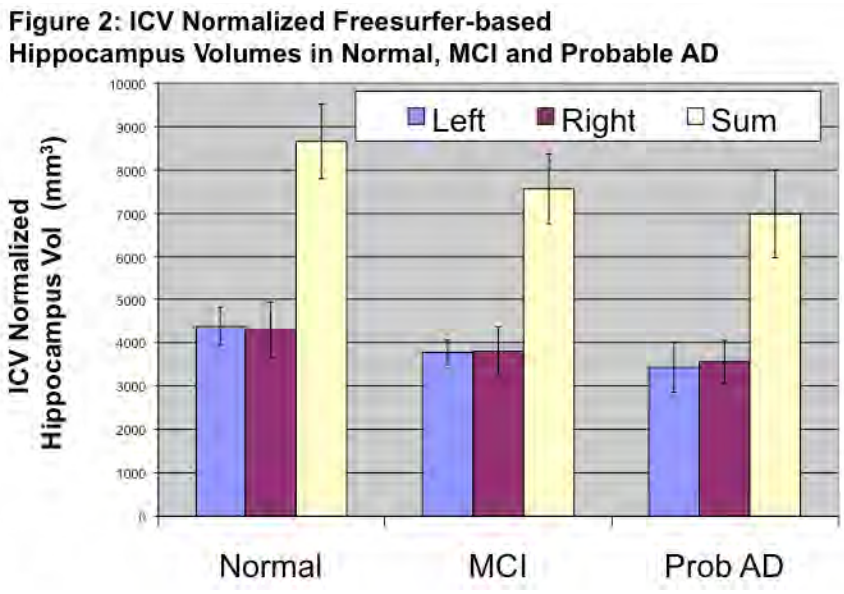

Figure 6.2: ICV Normalized Freesurfer-based Hippocampus Volumes in Normal, MCI and Probable AD

mm^3 voxel size, 4 mm thick slices no gap) DTI data were acquired using 25 encoding gradient directions at bvalues of 0 and 1000 sec/mm^2 with an acquisition matrix of 128×128. Anatomical data were acquired using a 256×256 acquisition matrix employing a SPGR sequence ($1 \times 1 \times 1$ mm^3 voxel size, 1 mm thick slices no gap) with TE=3.128ms, TR=7.832ms and TI=450ms. The hippocampi were identified using high resolution SPGR images via the Freesurfer software package (Harvard/MGH). The automatically segmented hippocampal ROIs were then co-registered back to the DTI subject space using SPM. Seed points where normalized by adjusting spacing according to subject intracranial volume (ICV). ICVs were calculated based on a weighted combination of grey and white matter, and CSF segmented volumes generated by SPM. By using a control average ICV of 1.5x106 mm3, all seed spacing was adjusted to compensate for ICV in individuals. Streamline tractography was performed using tensor interpolation with a 0.2 mm step-size utilizing in-house DTI software. Whole-brain tractography data were

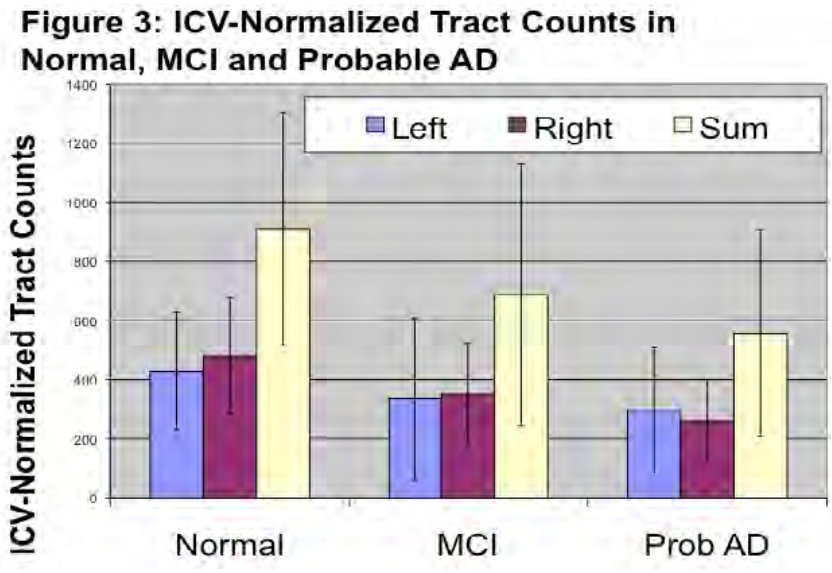

Figure 6.3: ICV Normalized Tract Counts in Normal, MCI and Probable AD

processed by several stages of filtering to obtain the fornix tracts. The steps are based on two known facts (1) fornix tracts connect the hippocampus and hypothalamus and (2) these tracts do not cross right/left hemispheres. First, only the tracts which intersect the hippocampal ROIs are considered. Next, all tracts originating from seed points outside of the fornix region are eliminated. Tracts originating from the fornix regions that progress out of the fornix region are kept for tract counting. However, the aforementioned tracts are cut back to where they deviate from the fornix for display purposes (fig. 1).

3 Results and Discussion

Results of hippocampal volume (fig. 2) confirm the progressive degenerative effects of MCI and AD and validate the usability of Freesurfer defined hippocampal ROIs without any subjective input. ICVNormalized tract counts for the fornix (fig.3) show a similar progressive reduction. Although there is a measurable decrease in connectivity based on

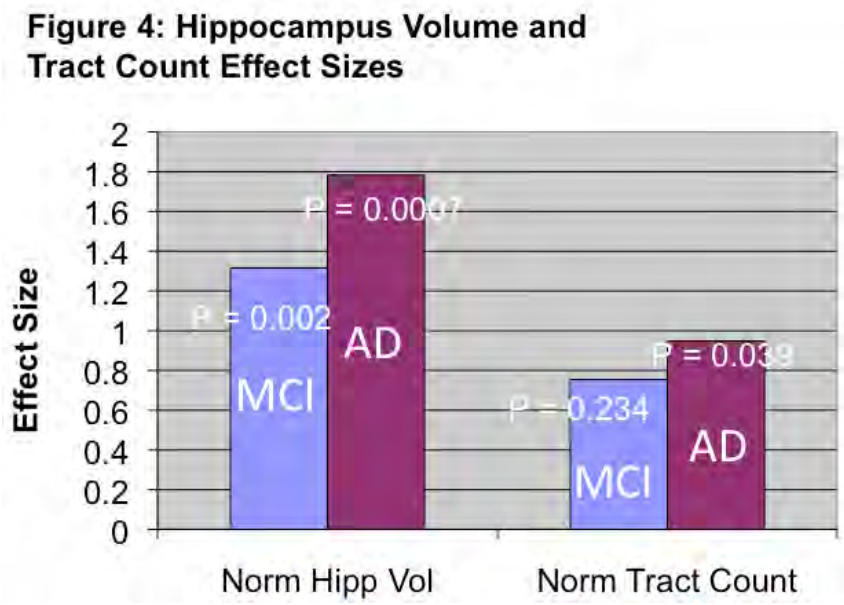

Figure 6.4: Hippocampus Volumes and Tract Count Effect Sizes

normalized tract count (Prob AD p=0.039,eff size = 0.9), the effect seems to be less than what is measured using normalized hippocampal volumes (Prob AD p=0.0007, eff size= 1.8) (table 1). Although the effect of Alzheimer Disease on hippocampal volume is known, its effects on the afferent and efferent connections between the hippocampus and other structures via the crucial fornix tract is relatively unknown. Relatively large voxel sizes were used in this study (2x2x4mm3) creating partial volume confounds. We expect that as higher resolution DTI data are acquired, the effects of partial volume will be reduced leading to better tract quantitation and improvements in effect sizes corresponding to fornix and other affected tracts.

Table 6.1: Table 1: Effect Sizes and t-test of Normalized Hippocampus Vol and Normalized Tract Count against Normal Population Normalized Tract Cou

		Normalized Hippocampus Volume	Normalized Tract Count
MCI			
Effect Size		1.315	0.754
t-score		3.553	1.246
df		24.822	13.435
Sig (P-value)		0.002	0.234
Mean Difference		1093.255	223.625
Std Error Difference		307.678	179.485
95% Confidence Interval	Lower	459.349	-162.857
	Upper	1727.161	610.107
Prob			
Effect Size		1.784	0.948
t-score		4.838	2.265
df		23.332	14.784
Sig (P-value)		0.001	0.039
Mean Difference		1650.224	353.167
Std Error Difference		345.224	155.870
95% Confidence Interval	Lower	956.635	20.513
	Upper	2383.812	685.820

Chapter 7

Comparison of Limbic Regions FA Using Tractography-defined ROIs in AD and MCI

D. H. Hwang[1], S. Tsao[1], and M. Singh[1]

[1] Depts of Biomedical Engineering and Radiology,
University of Southern California, Los Angeles, CA, United States

Proc. Intl. Soc. Mag. Reson. Med. 18 (2010)

1 Introduction

The fornix and cingulum (limbic regions) are suspected of being affected by mild cognitive impairment (MCI) and Alzheimer Disease (AD). Recent studies have reported observable reductions in FA of the cingulum between normal and AD populations. Most studies resort to manual tracing of the anatomy in patient acquisition space. Objective isolation of the fornix and cingulum has remained elusive. The purpose of this study was to (a) bring DTI including tractography to a common template space, (b) define the fornix and cingulum objectively using tractography, and (c) examine the FA changes among normal control, MCI and probable AD populations.

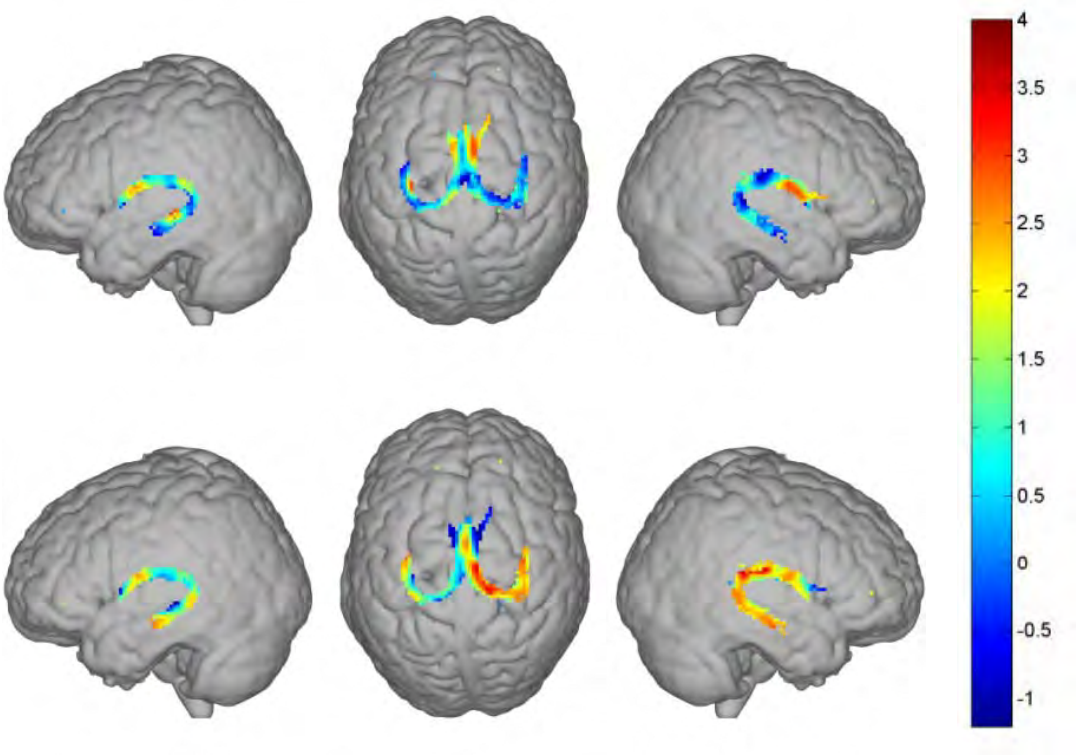

Figure 7.1: Fornix FA t-Score Comparison. MCI > AD (top row) NC > MCI (bottom row). Colors denote the t-score difference between the mean FA of the various populations.

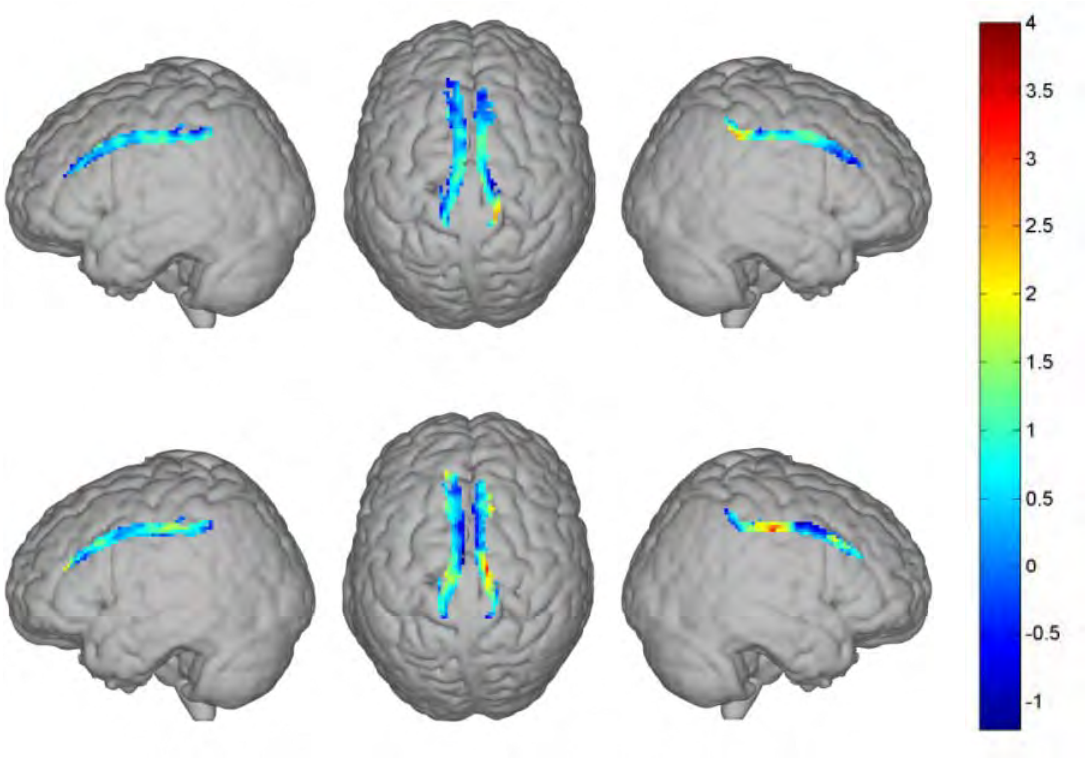

Figure 7.2: Cingulum FA t-Score Comparison. MCI >AD (top row) NC > MCI (bottom row)

2 Methods

Data were acquired on a 3T GE scanner from three populations (26 normal control, 16 MCI, and 13 AD probable) as classified by neuropsychological testing. Multi-slice (2.04 x 2.04 x 4 mm3 voxel size, 4 mm thick slices no gap) data were acquired using 25 encoding gradient directions at b-values of 0 and 1000 sec/mm2 with an acquisition matrix of 128x128. Anatomical data were acquired using a 256 x 256 acquisition matrix employing a SPGR sequence (1 x 1 x 1 mm3 voxel size, 1 mm thick slices no gap) with TE=3.128ms, TR=7.832ms and TI=450ms. SPM8 was used to co-register the DTI b-value = 0 data

to the SPGR images. A custom template was created using the 26 normal control scans. All anatomical scans were normalized to the template using SPM8's DARTEL suite. The custom template was then spatially normalized to MNI space. The three step transformation allows for the FA map to be warped into MNI space. Tractography was conducted in subject space using normalized seeds inversely mapped from the MNI space and individual tracts were mapped from subject space to MNI space thereby avoiding the problems associated with spatial warping of diffusion tensors. A single set of ROIs were defined in MNI space and applied to the normal control group whole-brain tractography to isolate the fornix and cingulum. Four processing masks were defined (left fornix, right fornix, left cingulum, and right cingulum) as voxels where tracts overlapped in at least 50% of the control group. A voxel-based comparison of the t-score statistics among the FA map difference of the three different populations was conducted using the four masks to highlight changes observed in the fornix and cingulum tracts.

3 Results and Conclusions

SPM8's DARTEL suite provided a much improved normalization of the aged brain populations. Visual inspection of the filtered fornix and cingulum tracts confirmed greatly improved alignment when compared to previous results. The t-score comparisons (Fig. 1 and 2) visually illustrate areas where FA in one population is higher than the other. There appears to be a progressive degeneration of the fornix and the cingulum. The right and left fornix branches both exhibit pattern of damage which begins at the hippocampal end of the fornix and propagates toward the hypothalamus with right greater than left reduction in FA. The cingulum shows less damage, but does appear to be show progressive

damage extending to the posterior end, more in right than left. The complete posterior cingulum portion could not be reliably identified in the common space for all subjects, suggesting a need for further improvement of normalization in AD. These preliminary results shows promise in tracking axonal damage with the progression of Alzheimer Disease. The right greater than left reduction of FA in the fornix and cingulum is consistent with several reports of white matter atrophy and hypometabolism in AD (e.g., Villain, N. et. al., J. NeuroSci. 28(24):6174-6181).

Chapter 8

CSF Contamination Correction in DTI Tractography of the Fornix in Elderly Subjects

S. Tsao[1], D. H. Hwang[1] and M. Singh[1]

[1] Depts of Biomedical Engineering and Radiology,
University of Southern California, Los Angeles, CA, United States

Proc. Intl. Soc. Mag. Reson. Med. 18 (2010)

1 Introduction

The microstructural integrity of the limbic regions is frequently compromised in neurodegenerative diseases such as Alzheimer Disease (AD). A key limbic region is the fornix located proximal to the ventricles. Given the relatively large voxel size used in most clinical DTI acquisitions, the probability of CSF contamination in the fornix is high, often leading to interruption of tracts due to either a reduction in FA or misdirection due to erroneous eigenvector estimation, particularly in AD where ventricles are enlarged. FLAIR DTI has been used by many investigators to suppress CSF (e.g. Kwong et al. MRM 21, 157-163, 1991) but at the expense of SNR and data acquisition time, and to our knowledge, FLAIR DTI is rarely used in clinical studies. Aiming toward eventual quantification of DTI metrics such as FA and tract density in the fornix and other limbic pathways in AD, the objective of this work was to develop a post-processing strategy to correct partial volume effects such that it could be used to analyze existing clinical DTI data.

2 Methods

Existing DTI data acquired on a 3T GE Signa HDx MRI using a multi-slice, twice refocused sequence with 128x128 single-shot EPI readout, 25 gradient directions with b=1000s/mm2, one b=0 image, TR/TE=8000ms/86.1ms, FOV 26cm, two averages, 4mm thick contiguous 28 slices covering the entire head in 2.03 x 2.03 x 4 mm3 voxels (scan time: approximately 7 minutes) were used. Relying on a straightforward bi-compartmental model (e.g., Koo et al. NeuroImage 44:136-144, 2009)

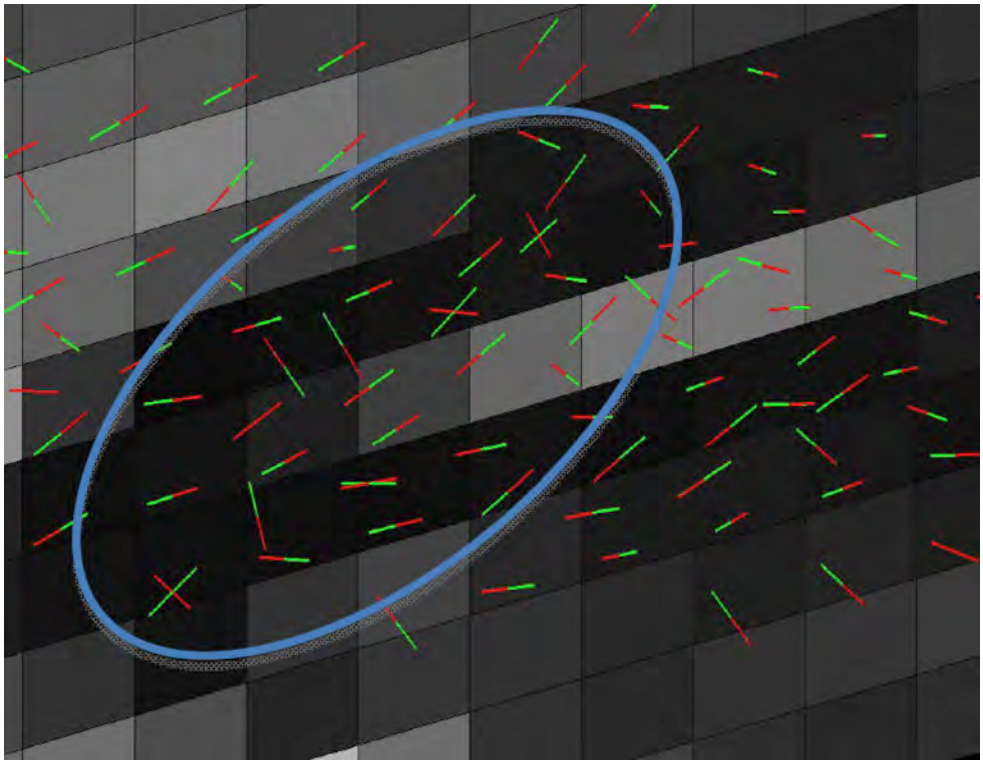

Figure 8.1: Corrected Primary Eigenvectors after CSF compensation correction in the anterior portion of the Fornix (Red Original Eigenvector) (Green Corrected Eigenvector)

$$S = f_{WM} S_{WM} + f_{CSF} S_{CSF} \tag{8.1}$$

where S_{CSF} , S_{WM} are the signals from a pure CSF and white matter (WM) voxel and f_{CSF} , f_{WM} are corresponding fractions of CSF and WM. We can isolate the white matter signal within any particular voxel by extending this model to the DTI signal for the 25 gradient directions given by

$$\frac{S^i}{S_0} = \frac{f_{WM} S^i_{WM} + f_{CSF} S^i_{CSF}}{f_{WM} S^0_{WM} + f_{CSF} S^0_{CSF}} \tag{8.2}$$

This allows us to extract the WM only DTI signal given by

$$\frac{S^i_{WM}}{S_{0WM}} = \frac{S - f_{CSF}S^i_{CSF}}{S_0 - f_{CSF}S_{0CSF}} \tag{8.3}$$

As we are only concerned with the mixing between CSF and white matter in this study, the gray matter (GM) fraction has been ignored but can be readily incorporated in a three-compartmental model. Derivation of f_{CSF} was based on using MD values of the voxel. K-means clustering was used to separate all voxels into three clusters: CSF, WM and GM. A linear interpolation was done between the CSF and the WM MD values as an estimate of CSF content. To get S_{CSF} and S_{0CSF} , we used only the voxels from the ventricles and with CSF content f_{CSF} greater than 99%. Correction was then performed only on voxels with f_{CSF} less than 70 percent to avoid problems with overcompensation and possible errors in our estimate of f_{CSF} .

3 Results

An increase in FA was found in tract-based ROIs of the fornix after correction, due to an increase in anisotropy after the isotropic CSF component has been removed (see table 1). Results also indicate that the primary eigenvector and therefore the tractographic vector orientation can also been corrected (see fig. 1), leading to less erroneous tracts and allowing for the tractography of fornix at a lower FA threshold (see fig. 2).

Table 8.1: Corrected FA scores of 4 Normal age matched elderly subjects

Subject	Right Fornix		Left Fornix	
	Corrected FA	Original FA	Corrected FA	Original FA
1	0.4150 ± 0.0372	0.3398 ± 0.0219	0.4428 ± 0.0312	0.3633 ± 0.0210
2	0.2149 ± 0.0182	0.1980 ± 0.0096	0.2801 ± 0.0355	0.2465 ± 0.0170
3	0.2179 ± 0.0344	0.1884 ± 0.0133	0.1997 ± 0.0094	0.1968 ± 0.0058
4	0.2476 ± 0.0370	0.2010 ± 0.0147	0.3175 ± 0.0405	0.2627 ± 0.0227

4 Conclusion and Discussion

Our results suggest that WM voxels that have been contaminated by CSF can be corrected via a simple compartmental model that boosts FA values (table 1) and corrects for primary eigenvector orientation estimation (fig. 1). This is particularly useful in aged subjects that have high degrees of cerebral atrophy that increases CSF contamination in a large number of voxels.

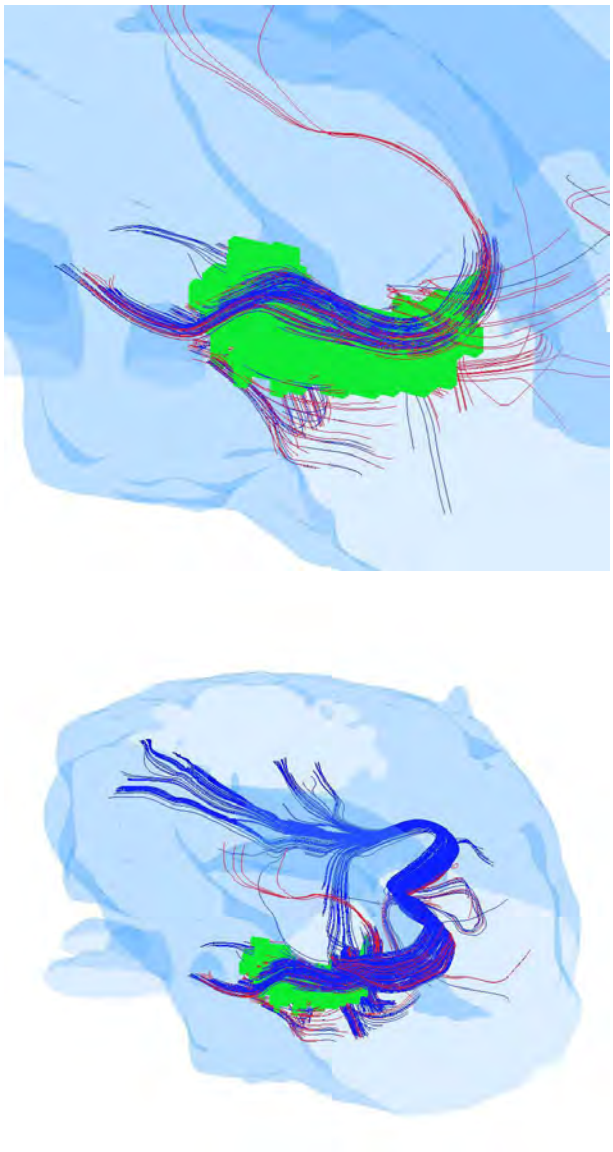

Figure 8.2: Corrected Tractography (RED) and uncorrected Tractography (BLUE) at FA threshold of 0.14 of tracts of the Hippocampus (green ROI). Figure shows (1) correction recovering the superior portion of the fornix (2) reduction of erroneous tract.

Chapter 9

ICA-based Multi-Fiber DWI Tractography in Neurosurgical Planning

Sinchai Tsao*[1,2] Niharika Gajawelli*[1,2] Peter A. Michels[1,2] Darryl Hwang[1,2] Yi Lao[1,2]
Fernando Yepes[1] Vidya Rajagopalan[1] Meng Law**[2] Natasha Lepore**[1,2]

[1] University of Southern California, Los Angeles, California, USA
[2]Children's Hospital Los Angeles, Los Angeles, California, USA
*,** These authors share equal contribution

Proceedings of MICCAI 2013 DTI Challenge Workshop (In Press Springer LNCS)

1 Abstract

Diffusion Tensor Imaging is a powerful imaging modality that allows us to investigate the underlying white matter fiber structure of the brain. However, it has many limitations, including its inability to resolving fiber crossings. Many multi-fiber techniques attempt to solve this problem, but they often require high power computation as well as High Angular Resolution Diffusion Imaging (HARDI) data [57]. Since diffusion imaging has the potential to contribute to the presurgical planning by clearly delineating white matter anatomy and integrity, it is important to determine methods that solve the crossing-fiber problem in the clinical setting. Here, we explore the use of a recently developed tractography technique that utilizes Independent Component Analysis (ICA)-based multi-fiber orientation estimation. This ICA-based technique leverages neighborhood voxel information for fiber estimation and has been shown to function especially well with clinical data that have small number of gradient directions and b-values, using limited computation power and time [58, 59]. We were able to reconstruct estimations of the white matter corticospinal tracts from both of the MICCAI 2013 Challenge neurosurgical cases. Patient 1 demonstrates penetration of the corticospinal tract by the mass, suggesting that complete retraction of the glioblastoma would result in severe distruption of the right CST. Any remaining right CST related function could be lost. Patient 2 shows some displacement of the right CST. When comparing to the contralateral left CST, the right CST seems to be relatively intact. The mass also seems to have displaced a small portion of the right CST. In conclusion, the ICA-based method performed relatively well in both patients, clearly delineating the CSTs relative to their respectives masses. Our method also showed marked improvements when compared with the single-fiber DTI model.

Keywords: MRI, ICA, DTI, Tractography, DWI, Neurosurgery, Multi-Fiber

2 Introduction

Radiological examinations play a crucial role in surgical planning and guidance. Magnetic Resonance Imaging (MRI), in particular, is of considerable use due to the lack of ionizing radiation, and can serve not only for treatment planning but also for evaluating outcomes. In surgical oncology, preoperative radiological examinations not only provide information about the extent of masses as well as indication of the degree of necrosis and edema, but also give a measure of tissue integrity not observable intraoperatively. In particular, preservation of white matter connectivity can severely affect postoperative outcomes in terms of both behavior and function. In this challenge, we attempt to mediate postoperative motor function loss by accurate delineation of the corticospinal tracts using diffusion weighted imaging and tractography.

Diffusion weighted imaging (DWI) is a unique modality in medical imaging which enables us to model the diffusion pattern of water in the brain. The most commonly used DWI method is diffusion tensor imaging (DTI), in which rank 2 tensors or 3 x 3 matrices are computed at each voxel using the diffusion weighted images. The primary eigenvector indicates the primary direction of unrestricted diffusion in a particular voxel and is thought to be aligned with neuronal fiber paths in the brain.

This model of diffusion, however, does not take into account fiber crossings which have been hypothesized to occur in the majority white matter voxels in the brain[60]. Currently, there are many other models using high b-values, and large numbers of gradient directions such as HARDI[57] or diffusion spectrum imaging[61] data, but these datasets are hard to acquire in a clinical settings due to limitations in acquisition time. Our method attempts to circumvent these issues by estimating multiple fibers in each voxel using clinical data

Table 9.1: DWI Information

	Patient 1	Patient 2
Number of Gradient Directions	20	20
Image Size ($mm \times mm$)	1.14 x 1.14	1.14 x 1.14
Slice Thickness(mm)	5.2	5.2
b-value (mm/s)	1000	1000
Number of Slices	30	29
Number of Repetitions	4	4

with limited b-values and gradient directions, and utilizing much lower computational resources when compared to methods such as spherical deconvolution[62].

3 Methods

3.1 Data

The 2013 MICCAI DTI Challenge provided participants with DWI datasets from two neurosurgical cases. Patient 1 has a recurrent/residual glioblastoma W.H.O Grade IV. Patient 2 is diagnosed as 'Infiltrated Glioma, no grade'. Diffusion weighted images were provided in the NRRD format with 20 gradient directions, each with a b-value of 1000 s/mm^2. Patient 1's image had 30 slices and Patient 2 had 29 slices. The acquisition was repeated 4 times with voxel dimensions: 1.14 mm x 1.14 mm x 5.2 mm. Co-registered anatomical images as well as a labeled tumor volume were also provided. Two additional datasets of Patient 3 with diffusive low grade WHO II glioma were released for further

evaluation. The Patient 3 data was aquired at 2 timepoints, 6 weeks and 2 weeks prior to surgery and acquired with 30 gradient directions and 20 gradient directions respectively.

3.2 Pipeline

All data including the DWI data was first converted to a NIFTI file format and checked for obliqueness and consistency in orientation. Next, we computed a mean DWI volume, using the 4 base volumes, as well as brainmask with AFNI[63]. We then use Independent Component Analysis to recover the directions of individual fibers from a mixture of fibers within a voxel. Display and render of tracts as well as filtering was done using TrackVis[64].

3.3 Independent Component Analysis

Consider the diffusion field of a fiber as the source, and the voxel as a sensor; in this formulation each voxel is considered to be "sensing" signals from multiple sources. The implementation of our multi-fiber "unmixing" paradigm is based on the paper by Singh et al 2010[58]. The attenuated diffusion signal from each of the gradient directions, X_i can be written written as $X_i = S_i/S_0$, where i is each gradient direction, S_i is the diffusion weighted image and S_0 is the non-diffusion weighted scan.

In using ICA, a few assumptions were made: (1) Fibers cross through multiple voxels maintaining their orientation and (2) Fiber signal sources are independent. The latter assumption is made considering the rather large size of voxels (on the order of mm) compared to the order of diffusion of water molecules in axons (on the order of 10um). Unless the diffusion time is extremely long, molecules diffusing around axons of one fiber will not have a significant interaction with those diffusing around axons of another fiber.

Therefore similar to the conventional ICA construction, assuming we have k fibers crossing in a small neighborhood of n voxels, we can formulate the fibers as k independent sources, $s_1, \ldots, s_k$ from $x_1, \ldots, x_n$ measurements:

$$x_i = \sum_{j=1}^{k} a_{ij} sj \; \forall i = 1, 2, \ldots, n \tag{9.1}$$

where a_{ij} is the mixing fraction of j-th source in the i-th voxel.

The aim in ICA is to find a linear transformation of the dependent sensor signal x_i that makes the outputs as independent as possible. In vector-matrix notation: $\mathbf{x} = \mathbf{As}$ *or* $\mathbf{s} = \mathbf{A^{-1}x}$. Each linear combination $y_j = \sum w_{ij} xi$ would be an estimate of a single source if each row of matrix $\mathbf{A^{-1}}$ is w_{ij}. ICA assumes that the sources are non-Gaussian and Singh et al 2010[58] showed that the S_i/S_0 distributions of a single fiber are approximately non-Gaussian. Therefore ICA should correctly assume that the sum of non-Gaussian variables would be increasingly more Gaussian than our original source. From this fact, we postulate that the W_{ij} that maximizes the non-Gaussianity of yi give an accurate estimation of the orientation of our sources. To solve for this linear transformation, we started with a random set of w_{ij}, and used a center voxel surrounded by $n-1$ voxels to maximize the non-gaussianity of y_j with the fastICA algorithm[65], which relies on negentropy to maximize non-gaussianity. After computing the sources using ICA, DTI processing was done to calculate the tensors and estimate the fiber directions.

Table 9.2: Tractography Parameters

Type:	Streamline
FA Stopping Threshold:	0.02
MD Stopping Threshold:	4.00
Track Step Length:	0.1 mm
Max Number of Steps:	4000
Maximum Change in Angle:	45°
Number of Neighborhood Voxels used in ICA Estimation:	8

3.4 Tractography

Whole-brain streamline tractography was performed from the ICA fiber estimations. At each point, the consecutive direction was estimated as the weighted sum of correlated directions from neighborhood voxels. The parameters used were as follows:

The ROIs used for tractography filtering includes a slice filter placed in the z-direction, to ensure tracts meet a certain length, a slice filter placed in Y-plane at the middle of the volume, and a large sphere filter posterior to the brainstem, both to remove spurious tracts.

4 Results

Figures 9.1 and 9.3 show the results of our ICA-based multi-fiber tractography for Patient 1 and 2, respectively. For comparison, we ran the exact same streamline algorithm but instead used the primary eigenvector orientation from single-fiber DTI as our estimate of fiber orientation in Figures 9.2 and 9.4. We rendered the tracts in front of a coronal color

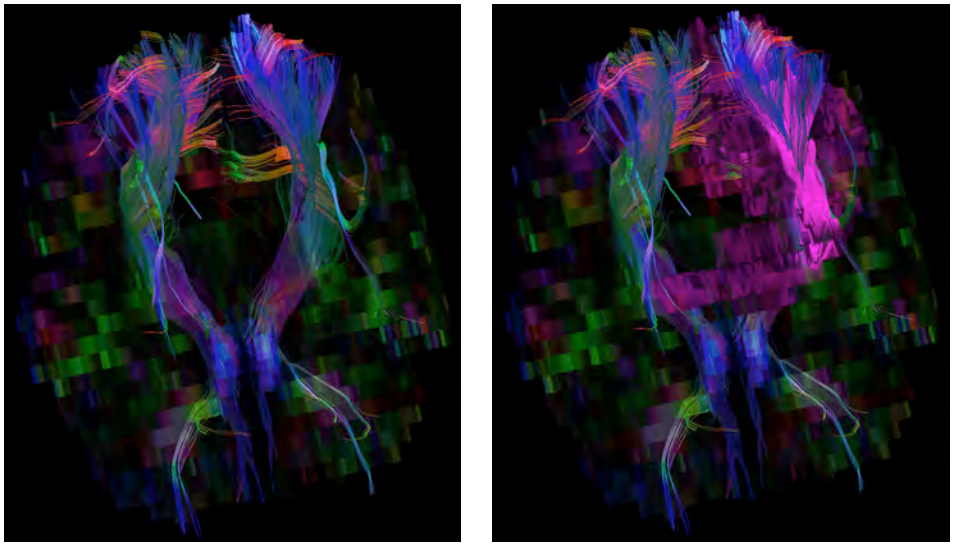

Figure 9.1: Patient 1 CSTs using multi-fiber ICA-based tractography with coronal slice showing color FA; without tumor volume (L) and with tumor volume (R).

FA slice to give a sense of overall orientation in the brain. The tumor volume is rendered as a semi-opaque volume on the right.

5 Discussion and Conclusion

This paper demonstrates the performance of ICA-based DWI tractography of the CST in two neurosurgery cases. Patient 1 has a tumor that is positioned central to the CST tract and is more challenging than Patient 2. In the former case, the differences between single-fiber tractography versus multi-fiber ICA-based tractography is more obvious. However, upon closer inspection the differences between single-fiber tractography versus multi-fiber tractography become increasingly stark in the peritumoral regions as well as regions of known crossings near the corpus collosum, cerebral cortex as well as lower down in the brain stem.

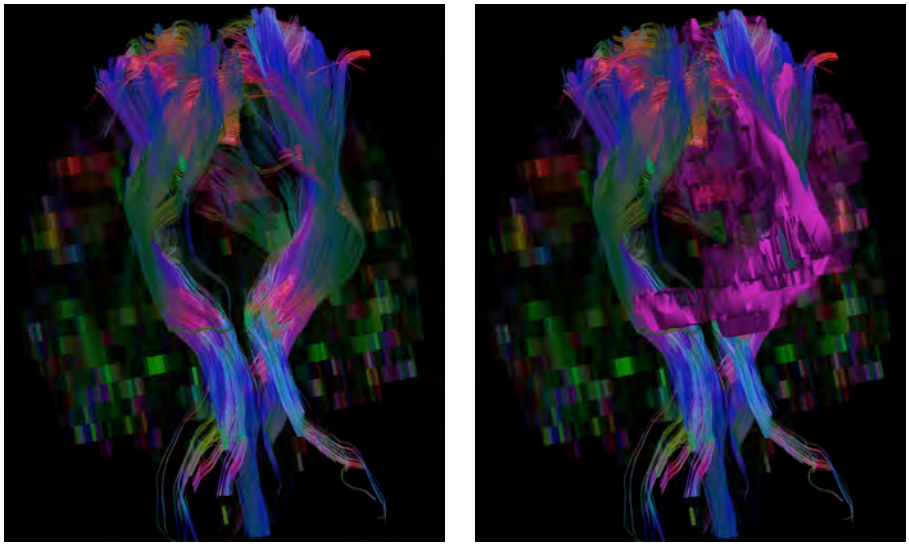

Figure 9.2: Patient 1 CSTs using single-fiber DTI tractography with coronal slice showing color FA; without tumor volume (L) and with tumor volume (R)

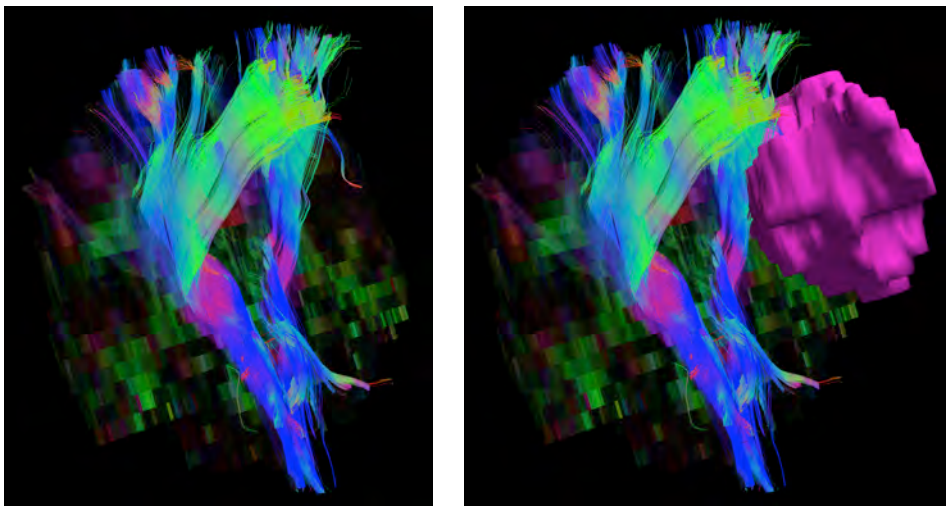

Figure 9.3: Patient 2 CSTs using multi-fiber ICA-based tractography with coronal slice showing color FA; without tumor volume (L) and with tumor volume (R)

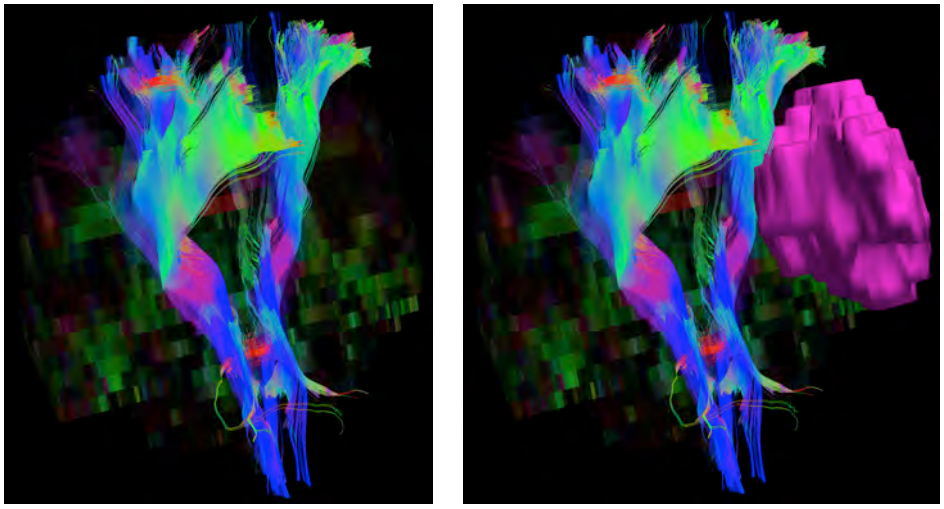

Figure 9.4: Patient 2 CSTs using single-fiber DTI tractography with coronal slice showing color FA; without tumor volume (L) and with tumor volume (R)

The authors believe that the multi-fiber neighborhood technique may have mitigated some of the effects of edema from the tumor. This is possible because the edema component can be seen as a independent source of signal consistent across neighborhood voxels close to the tumor. We also believe that the large 5.2 mm slice thickness may be causing severe partial volume effects. The non-isometric voxel sizes may also cause directional biases downstream from the tensor estimation and may affect tractography results. In previous work with non-isometric voxels, the authors observed differential performance from the ICA methodology between isometric and non-isometric voxels.

More work needs to be done to determine whether the increased signal-to-noise ratio of the larger slices outweigh the distortion effects it may have on multi-fiber and streamline tractography techniques that rely on neighborhood information. The geometry of the tracts in question may also determine the optimal geometric configuration of voxel sizes and location. In this case, the CST tractography may seem denser simply because of

the direction bias in the Ventral-Rostral direction caused by increased slice thickness in the Z-direction and may be mistaken for improved results. This can be seen in the comparison between our single-fiber and multi-fiber methods in patient 2, where the ICA-based methods seems to have decreased fiber density, but where there is also less noise at the peritumoral regions as well as the end points of the tracts.

In conclusion, this paper (1) demonstrates the application of a computationally thrifty multi-fiber orientation estimation methodology suitable for neurosurgical planning applications, (2) revisits and examines its performance against traditional tractograpy using DTI's primary eigenvector but in a clinical neurosurgical setting and (3) aims to be the first step towards fine tuning both imaging as well as tractographic parameters for eventual vetting of the ICA methodology as a viable multi-fiber tractographic tool for neurosurgical planning.

Acknowledgements

The authors would like thank their colleagues Alec CW Wong, PhD and Bryce Wilkins for all their efforts in developing and testing ICA-based tractography. This work would not be possible without their tireless dedication to science. We would also like to dedicate this publication in memory of their late advisor Professor Manbir Singh, PhD who championed the ICA methodology and whose guidance we miss dearly daily.

Chapter 10

The Power of Hybrid / Fusion Imaging Metrics in Future PACS Systems: A Case Study into the White Matter Hyperintensity Prenumbra using FLAIR and Diffusion MR

Sinchai Tsao[a,b] Samantha J. Ma[a,b] Peter A. Michels[a,b] Niharika Gajawelli[a,b] Meng Law[a] Helena Chui[a] and Natasha Lepore[a,b]

[a] University of Southern California, Los Angeles, California, USA
[b]Children's Hospital Los Angeles, Los Angeles, California, USA

Submitted SPIE Medical Imaging 2014

1 Abstract

Most white matter related neurological disease exhibit a large number of White Matter Hyperintensities (WMHs) on FLAIR MRI images. However, these lesions are not well understood. At the same time, Diffusion MRI has been gaining popularity as a powerful method of characterizing White Matter (WM) integrity. This work aims to study the behavior of the diffusion signal within the WMH voxels. The goal is to develop hybrid MR metrics that leverage information from multiple MR acquisitions to solve clinical problems. In our case, we are trying to address the WMH penumbra (as defined by Maillard et al 2011[66]) where WMH delineates a foci that is more widespread than than the actual damage area presumably due to acute inflammation. Our results show that diffusion MR metrics may be able to better delineate tissue that is inflamed versus scar tissue but may be less specific to lesions than FLAIR. Therefore, a hybrid metric that encodes information from both FLAIR and Diffusion MR may yield new and novel imaging information about the progression of white matter disease progression. We hope that this work also demonstrates how future PACS systems could have image fusion capabilities that would be able to leverage information from multiple imaging series to yield new and novel imaging contrast.

Keywords: DTI, Diffusion MRI, MRI, Alzheimer's Disease, Dementia, WMH, White Matter, FLAIR, Neuroimaging

2 Purpose

White matter hyperintensity (WMH) burden as detect on FLAIR MR images has been associated with cognitive impairment[67]. However, the degenerative process that leads to such lesions is not well understood. In this study, we investigate the diffusion properties of white matter lesions using diffusion MRI at 3T. To this end, a segmentation and coregistration routine was developed to segment WMHs and coregister them to diffusion measurements. The objective of this work was to characterize the diffusion characteristics of WMHs to allow for more accurate staging of white matter disease as well as to differentiate between early-stage lesion formation and end-stage white matter scars.

Table 10.1: Summary of Subject Demographics

Subject	WMH Voxels	Total WM Voxels	Percent WMH	Sex	Age
1	6,230	1,168,404	0.53%	M	73
2	1,411	1,113,728	0.13%	F	70
3	9,767	1,146,941	0.85%	F	86
4	13,546	1,334,280	1.02%	M	75
5	1,282	1,096,588	0.12%	F	78

3 Methods

Diffusion tensor imaging (DTI) data was acquired on a 3T GE Signa HDx MRI using a multi-slice, twice refocused sequence with 128x128 single-shot EPI readout, 25 gradient directions with b=1000s/mm2, three b=0 images, TR/TE=8000ms/86.1ms with 2.03 x 2.03 x 2 mm3 voxels. 3D T1-weighted and FLAIR images from 5 cognitively normal aged

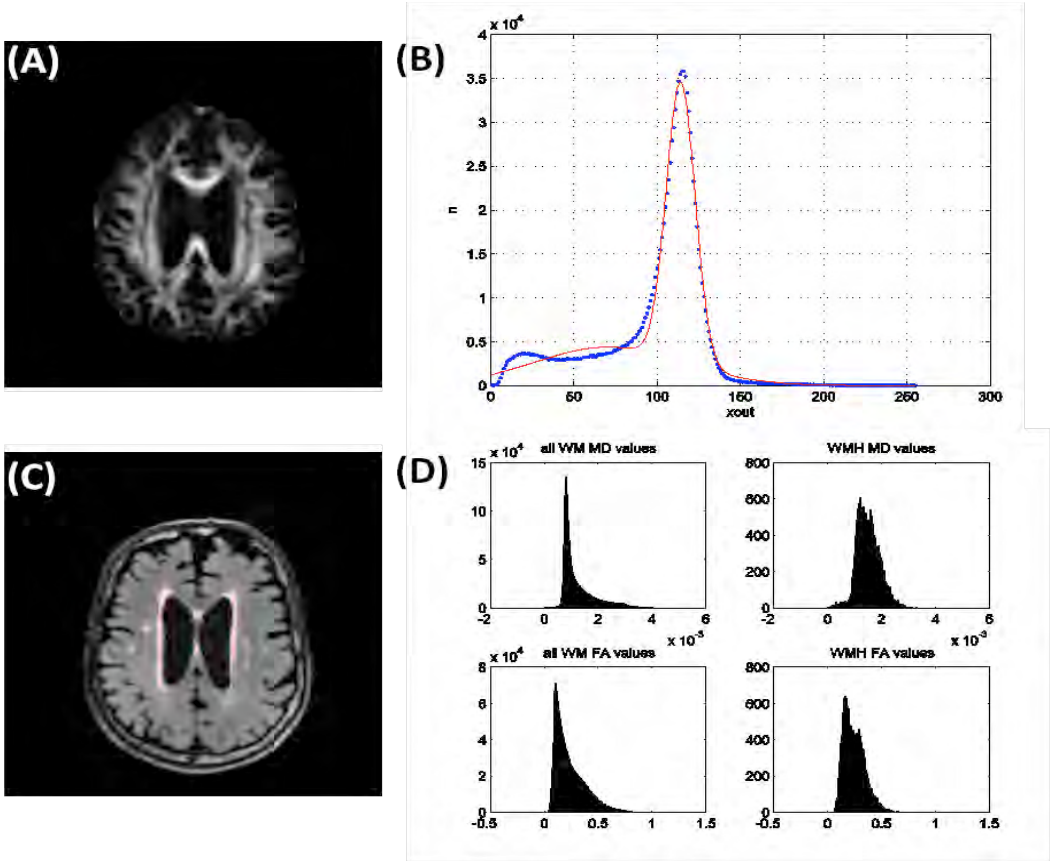

Figure 1 – Data for subject with very high WMH load. (A) FA image for WMH candidate region mask. (B) Histogram fitting for dynamic thresholding. (C) WMH image (Red). (D) MD and FA histograms in WMH regions vs. all WM regions.

Figure 10.1: Data for subject with very high WMH load. (A) FA image for WMH candidate region mask. (B) Histogram fitting for dynamic thresholding. (C) WMH image (Red). (D) MD and FA histograms in WMH regions vs. all WM regions.)

subjects. Initial preprocessing involved several standard toolkits available in the public domain. FreeSurfer was used for intensity non-uniformity correction and the removal of non-brain tissues. SPM8 was used to coregister the DTI b=0 data to the T1-weighted and FLAIR images. A WMH candidate region mask was generated using an in-house written MATLAB code that was driven by DTI fractional anisotropy (FA) measurements. WMH segmentation was processed in the WMH candidate region using dynamic thresholding based on histogram analyses (see Fig. 10.1: A, B, C). Diffusion measurements were taken

in the WMH regions and compared to those measured in all white matter regions of the brain.

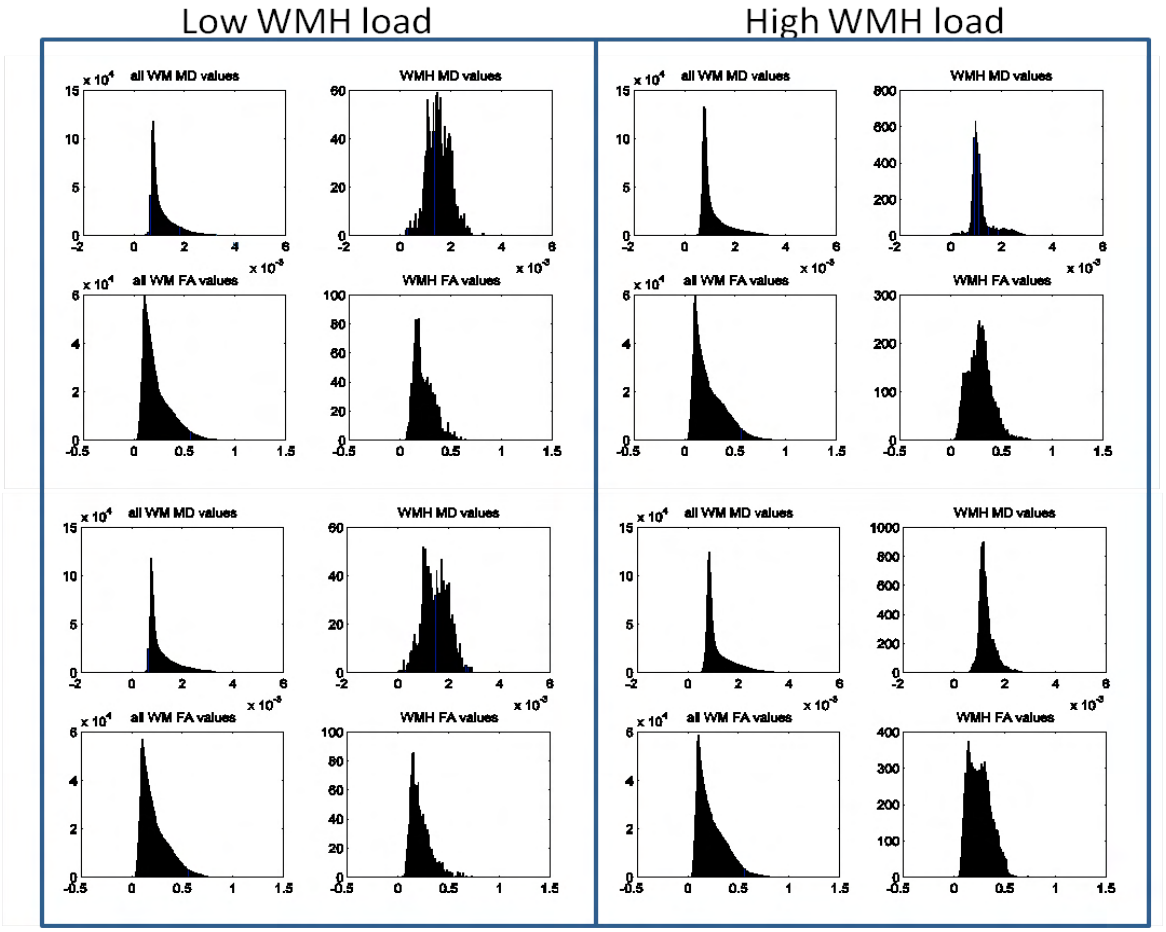

Figure 2 – MD and FA histograms for low WMH load and high WMH load subjects compared with MD and FA in all WM for each subject.

Figure 2 – MD and FA histograms for low WMH load and high WMH load subjects compared with MD and FA in all WM for each subject.

4 Results

For subjects with low WMH load, mean diffusivity (MD) values within the WMH regions were distributed differently in the histogram compared to MD values in all white matter

(WM) regions. The histogram of WMH FA values for these subjects maintained a similar distribution to all WM regions. Histograms for subjects with high WMH load exhibited the opposite relationship (see Fig. 10.2). For the subject with a very high WMH load, the MD and FA histograms for WMH regions were similar (see Fig. 1 D).

5 Conclusion

Our results suggest that early-stage lesion formation is may be characterized by MD changes, while regions with long-term lesions display FA changes. End-stage WM scars exhibit similar DTI measurement distributions, indicating stabilization of the tissue. This is consistent with previous observations of what investigators have termed WMH penumbra[66], where the WMH delineated a foci of more widespread and subtle white matter damage that can be characterized with Diffusion MRI.

Acknowledgements

This work has been supported by USC ADRC's National Institutes of Aging Program Grant 5P01AG012435-18 as well as National Institute of Biomedical Imaging and Bioengineering grant 5R21EB013456-02.

Chapter 11

FreeSurfer Parcellation of Brains Containing Large Infarcts

Niharika Gajawelli[1] Sinchai Tsao[1] Darryl H. Hwang[1] Bryce Wilkins[1]
Stephen Kriger[2] Susanne Mueller[2] Diana Truran[2] Meng Law[3]
Helena Chui[4] Michael Weiner[2] Manbir Singh[1,3]

[1]Department of Biomedical Engineering, University of Southern California,
Los Angeles, California, United States
[2]Center for Imaging of Neurodegenerative Diseases, VA Medical Center,
San Francisco, California, United States
[3]Department of Radiology, University of Southern California,
Los Angeles, California, United States
[4]Department of Neurology, University of Southern California,
Los Angeles, California, United States

Resubmission in Progress

1 Abstract

Purpose: To compensate for imaging changes in areas of cerebral infarct to facilitate successful brain segmentation in FreeSurfer.

Materials and Methods: A non-linear co-registration method to and from an atlas space allowed for voxel intensities from the contralateral hemisphere to fill in areas of cerebral infarct in order to facilitate successful segmentation. A validation study was conducted using T1 volumes of 5 normal age-matched subjects, with known he FreeSurfer analysis, were simulated with cerebral infarcts from 8 stroke patients.

Results: Before application of our method, FreeSurfer had a completion rate of 50% with our data. Application of our method yielded 100% completion rate in FreeSurfer.

Conclusion: Our method allows for the inclusion of data with cerebral infarcts into automated brain segmentation workflows.

Keywords: FreeSurfer, stroke, infarct, parcellation

2 Introduction

Volumetric analyses of brain images play an important role in investigating cerebral diseases that affect brain structure such as Alzheimers disease or Vascular dementia in elderly subjects (1). Brain volumes decrease with age, and changes in particular regional volumes may be associated with certain neurological disorders. For example, it is shown that the hippocampal volumes are particularly affected in patients with Alzheimers disease (2). Segmentation of brain volumes into various regions requires a good deal of anatomical knowledge and has traditionally been done manually by experts trained in this area (3). However, this process is tedious, requires the resources of skilled experts, and is prone to human error, making it unfeasible for large scale studies, especially those that require the processing of data of hundreds of subjects.

As an alternative to manual segmentation, there exist several software packages that facilitate automatic brain segmentation. Many packages are capable of segmenting the brain volume into white matter, gray matter and cerebrospinal fluid, but only a few are capable of segmentation and parcellation into more specific regions. FreeSurfer (4), frequently used in the neuro-imaging community, is a robust, validated package that utilizes volumetric methods for the cortical and sub-cortical segmentation of structural MRI. In the processing pipeline, FreeSurfer incorporates prior probabilities of tissue classes (the probability that an anatomical feature exists at a certain global position), as well as the relative spatial positioning pattern of various tissues for the segmentation and parcellation processes (5), (6). Therefore, the classification of various brain regions is highly dependent on the integrity of neighborhood voxels and their structure, which leads to frequent failure of FreeSurfer processing in the presence of pathologic lesions or cerebral

infarcts often present in elderly subjects. For these volumes, not only structures within, or in the vicinity of infarcts are affected, but distal regions may also be misclassified.

Classification of brains with infarcts is indeed important in order to gather information pertinent to brain volumes with stroke. In addition, neglecting such data would not only accrue unnecessary costs, but would also hinder analysis for regions not affected by the stroke. Efforts have been made to segment stroke volumes using multimodal image information (7); however, this information may not always be available. An important pre-processing step for large-scale studies is registration to a common template. Brain volumes with stroke have a significant amount of missing tissue as well as sulcal and morphological variability, thus, affecting the registration precision (8), (9). Registration of brain volumes with lesions using SPM (Statistical Parametric Mapping) software can be facilitated by filling-in the lesion with tissue from the contralateral hemisphere (10). The accuracy of this method, however, depends on the symmetry of the brain, and therefore is impractical in large-scale studies involving brain volumes of the elderly.

Taking into account the issues stated above, Solodkin et al. (11) proposed filling-in the stroke region using tissue from the homologous region of the contralateral hemisphere as follows. First, a mask was created by manually outlining infarct boundaries. This mask was used to acquire voxels from the contralateral hemisphere to transplant and morph into the infarct region. The alignment to the region surrounding the infarct was improved by adding manually traced sulci in the hemisphere with the infarct. The brain was then transformed into the Talairach space, where hemispheres were separated, interchanged, and rigidly registered to the ipsilateral hemisphere before being inversely deformed back into the native subject space. The scar lines created due to lack of continuity of tissue were removed using suturing software and an expanded lesion mask. Validation in this study

was done by comparing voxel differences between hemispheres, under the assumption that the overall structure would be the same for both hemispheres in a normal brain.

In this paper, we have demonstrated a similar technique that simplifies the filling process by completely eliminating the labor-intensive manual sulci-drawing step. It is shown below that generating a filled volume by automatically replacing the region from the contralateral hemisphere produces results reasonably similar to the original volume. To validate our technique, we manually simulated strokes in brain volumes of healthy elderly normal subjects and compared ratios of the cortical and sub-cortical volumes to their ground truth respectively, before and after filling the stroke. This approach requires minimal manual intervention and therefore facilitates analysis of large-scale volumetric studies requiring FreeSurfer parcellation of cortical/sub-cortical regions. In this method, we used SPM as it is a widely accepted MATLAB based tool, which can be used on any operating system.

As subjects undergoing an MRI scan are typically not positioned exactly symmetrical with respect to the midline of the brain, identification of homologous regions in the contralateral hemisphere requires an accurate realignment and spatial normalization of the brain. Spatial normalization of T1-weighted images being subjected to FreeSurfer analysis was accomplished by SPM affine and non-linear transformations (12) that map the coordinates of the subjects brain to the MNI template. First, the infarct boundaries were outlined manually to create a mask. The infarct was then filled-in with the mean intensity of the gray and white matter of the contralateral hemisphere of the T1 brain volume, as without such uniform filling, normalization often failed (10). The template used for spatial normalization was the MNI152 template acquired from the Montreal

Neurological Institute website. The result of the normalization in MNI space was manually compared to the template to check the correspondence of major features. After satisfactory correspondence between the two brain volumes was confirmed, the left and right hemispheres of the brain were interchanged (in MNI space) and normalized a second time. This step is equivalent to co-registering the contralateral hemisphere to the infarct-containing hemisphere and reduces the inter-hemispherical differences from morphological distortions likely to be caused by the infarct.

The volume was then mapped back to the subject space using the inverse deformation field. Finally, voxels corresponding to the infarct were inserted into the original subject data from this inverse mapped image. The output after each step along with the procedure is shown in Figure 1.

3 Validation

To validate our technique, cerebral infarcts from 8 stroke patients were simulated one at a time in T1 volumes of 5 normal elderly subjects in whom the FreeSurfer analysis was known. The normal elderly brains were determined by visually confirming no strokes were present and by checking the CDR scores of the subjects. Insertions of infarcts into the normal brains were done in normalized MNI space to account for the variances in brain symmetry and shape in native space. To simulate a realistic case, the infarct intensities were normalized to match that of the volume they were being placed into. After infarct insertion was completed in the MNI space, the inverse deformation field was applied to transform the volume back into the subjects native space. The infarct region was then transferred and placed into the original healthy brain. This final volume was

used as the starting point to apply the steps of our filling technique described earlier in the Methods section. To avoid inaccuracies caused by interpolation, we avoided directly using the deformed volumes. FreeSurfer was then run on all the original normal elderly brain volumes, all the un-filled volumes generated after various stroke insertions, and all of the filled volumes after implementing our approach. The outputs from all studies were evaluated quantitatively by comparing ratios of the cortical and sub-cortical volumes to their ground truth respectively, before and after filling the stroke. The regions entirely or partially within the infarct mask, as well as regions not relevant for this study such as ventricles and vesicles were discarded from the final cortical and sub-cortical volumes. This was done by using the FreeSurfer command mri_segstats with the –mask option to find regions that are partially or completely included in the mask. The mean and standard deviation of the ratios for the various brain regions acquired from the 40 validation studies were computed and the histograms were fit to a Gaussian distribution for comparison.

4 Results

An example of FreeSurfer brain parcellation in a validation study from a subject with a relatively large infarct is shown in Figure 2. Significant changes were seen before and after filling-in the infarcted region. Fig. 2(a) shows an example of a simulated stroke/infarct region. This particular infarct was in the right pre-frontal region and therefore results for the right hemisphere are displayed. The regions encompassed within the infarct are the Caudal Middle Frontal Gyrus, the Precentral Gyrus, the Superior Frontal Gyrus, the Insula, and the Parsopercularis. Fig.2 (b) displays the ground truth parcellation, while (c) the result after inserting this infarct. The yellow circles indicate regions outside

the infarcted region that show high deviation from the ground truth. The similarity of the parcellation between the ground truth and the result after filling, shown in (d) is remarkable. Brain volumes inserted with the same infarct had in general many overlapping areas, which were eliminated when calculating the aggregate ratios for analysis. Regions that had a partial infarct were also eliminated and the average was computed only with volumes that did not have any infarct in the regional volume. Fig. 3(a) shows the ratios for one simulation study using one infarct in five different normal brain volumes. Less variation exists between the parcellated brains as exhibited by the smaller error bar for the filled case and the case when smoothing is also applied after filling. Histograms generated from averaged ratios of all combined simulation studies (8 brains x 5 lesions) for the filled, filled and smoothed, and unfilled cases are fit to a Gaussian distribution and shown in Fig. 4 (b). The filled volumes have a mean slightly closer to 1.0 and about 30% smaller standard deviation, reflecting the closeness of the reconstruction to the ground truth. Although the mean for all cases is close to 1, it is important to note that larger strokes limit the reconstruction affecting distal regions as well as the proximal, causing the standard deviation for the unfilled brain volume ratios to increase. A comparison of our SPM-based approach was made to using the symmetric diffeomorphic mapping normalization option (SyN) included in ANTs (Advanced Normalization Tools) software (13). ANTs provides open-source functionality for deformable normalization with large deformations. SyN was placed as the top performer amongst 14 other tools in an independent evaluation of ANTS normalization tools (14) and therefore is used for comparison.

For this evaluation, the brain volume was first normalized to a template space and then separated into the left and right hemispheres and inverse normalized to the subject space. The hemisphere without the lesion is then normalized to the hemisphere with the

lesion using the SyN option in the ANTS tool. The procedure outlined in the paper by Solodkin et. al (11) was followed except for the manual delineation of sulci. FreeSurfer was run again on these volumes and volume ratios from various regions of the original to the filled using our SPM based method was compared to that using ANTs diffeomorphic mapping. For this comparison, fewer subjects were used (4 infarcts in 3 different normal brains) but as shown in Figure 4, the histogram and the distributions are very similar, with the standard distribution acquired by ANTS being slightly better. Our approach, when applied to the stroke subject volumes, works well even in brains with larger lesions. Although for this comparison, the ground truth is unknown, FreeSurfer parcellations and segmentations are manually examined for quality and there improvement noticed after filling in the infarct region. The results of infarct filling in a stroke subject are shown in Figure 5. The dotted yellow circle indicates the stroke and we can clearly observe that there is a significant difference in some of the distal as well as proximal volume regions before and after the technique is applied.

5 Discussion

Out of 16 stroke brain volumes investigated in this study, FreeSurfer failed to complete processing on half of them before our technique was applied. All 16 volumes were processed successfully after filling. Therefore, our SPM-based approach is useful as a simple, automated pre-processing step before running FreeSurfer analysis for brain volumes containing infarcts. This method is very important in AD volumetric analysis as it would help quantify the regional volumes more accurately. Our FreeSurfer comparisons were also done with infarcts filled with uniform grayscale intensity, which was the mean of the

gray and white matter. However, the accuracy of the output varied widely depending on the stroke location (i.e. brain volumes with infarcts located in regions with greater intensity changes had inaccurate segmentation/parcellation). The location and size of the stroke is a limitation to be considered in future work. These factors affect the amount of sulci the stroke spans and may limit the accuracy of FreeSurfer results as our current process does not correct for the mismatch of sulci.

6 Conclusion

In conclusion, the results above suggest that our filling approach is a promising technique to conduct accurate volumetric analyses of brain structure even in the presence of cerebral infarcts, uses the widely accepted SPM software, requires minimal manual interaction, and is thus suited to automate processing of large-scale clinical studies. The methods discussed in this paper enable us to improve the ability of template methods to work when there exist pathologies that either remove or distort the brain in a major way. This is not limited to stroke and can be utilized for brain tumors, surgical removal, traumatic brain injury, as well as other neurological pathologies. Also, this method could be used to improve the functionality of any template based method with not only FreeSurfer but other software as well.

7 Acknowledgements

I would like to thank all members of the Biomedical Imaging Lab in the University of Southern California and the VA Medical Center in San Francisco for their help and support.

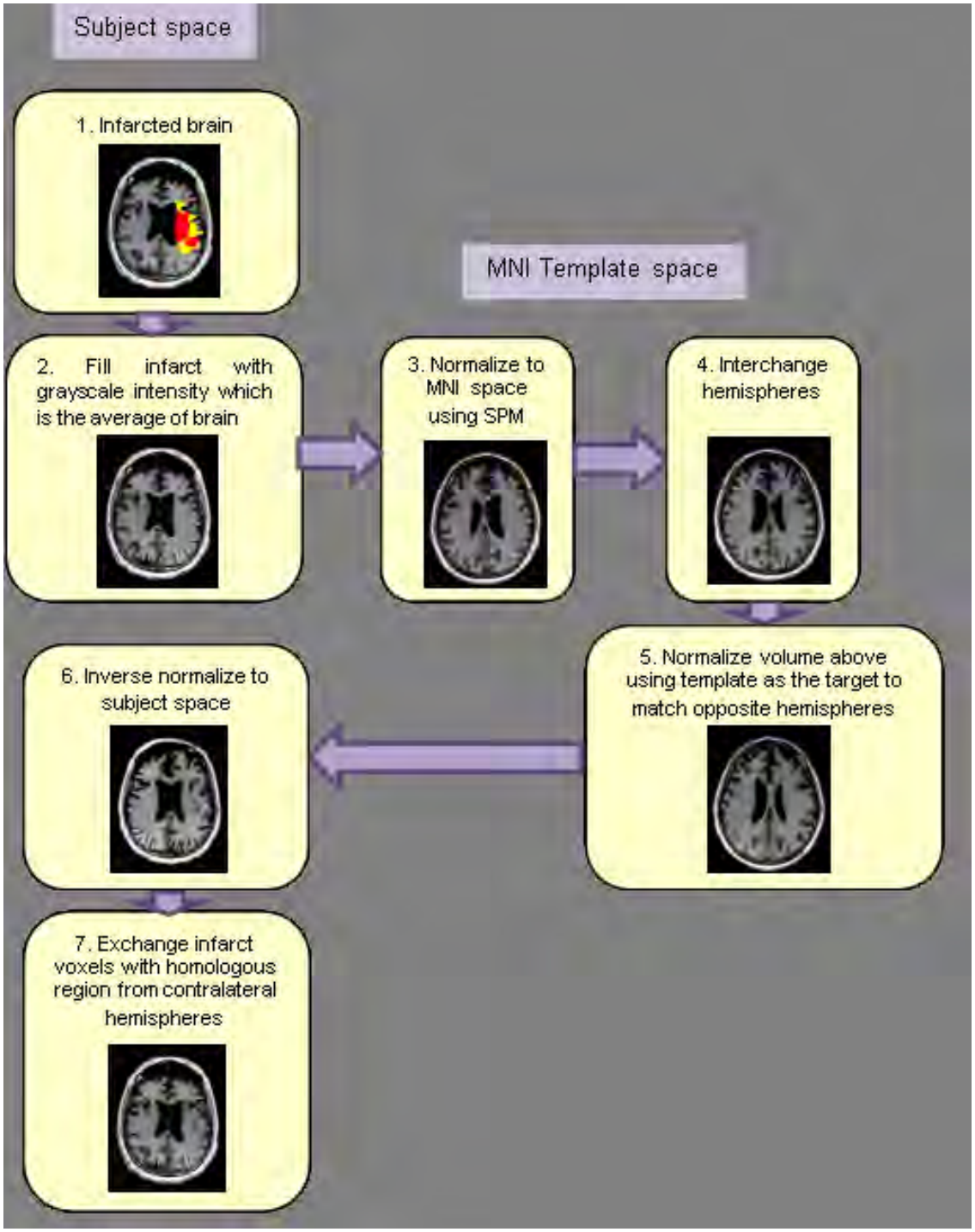

Figure 11.1: Diagram showing the process for filling in the brain infarct and the output after each step.

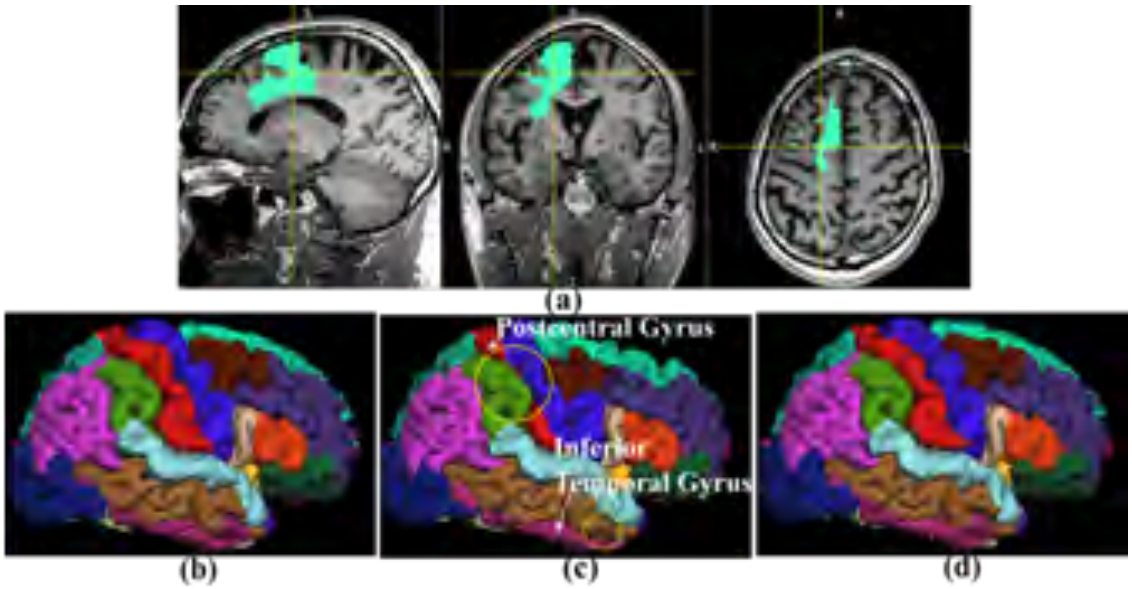

Figure 11.2: FreeSurfer parcellation result for validation study. (a) T1 slices showing simulated infarct; (b) Ground truth FreeSurfer parcellation; (c) FreeSurfer parcellation before filling simulated stroke; (d) FreeSurfer parcellation after filling. Circles highlight regions where significant distortions have been corrected after filling.

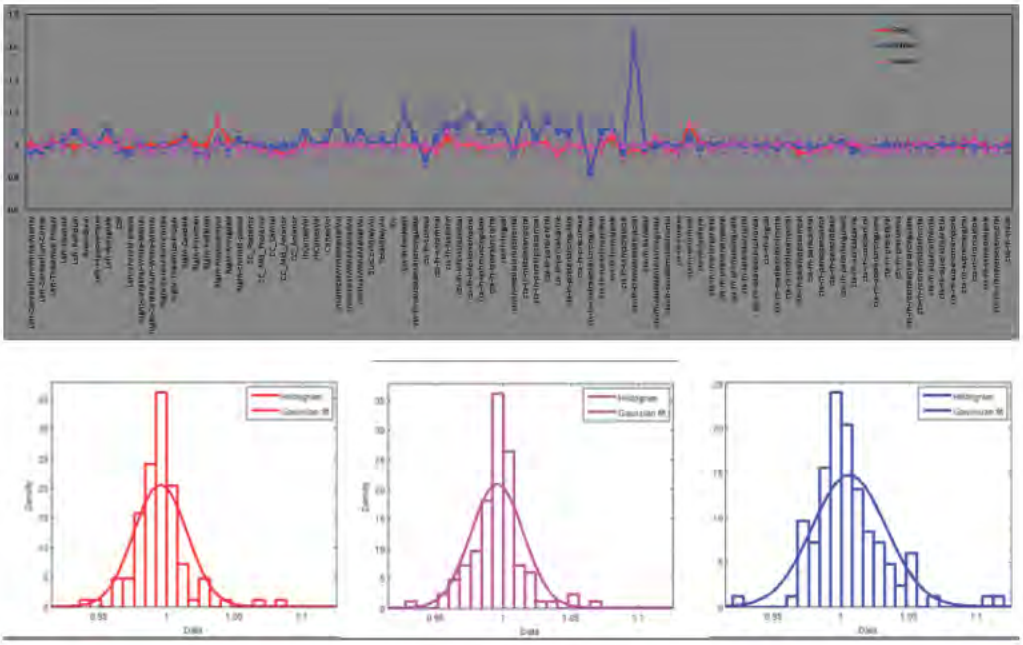

Figure 11.3: Ratios of various volumes of the FreeSurfer parcellation of the simulated infarct with respect to the ground truth. (a) Averaged volumes ratios of the before and after filling of cortical and subcortical regions in one simulated lesion using 5 different normal brain volumes. The red curve is the filled, the blue the unfilled and the pink the filled and smoothed. The red and pink plots are comparable. The figures on the lower rows are the Histograms and Gaussian fits of volume ratios of the (b) original to the filled brain, (c) original to the filled and smoothed brain, and (d) original to the unfilled brain.

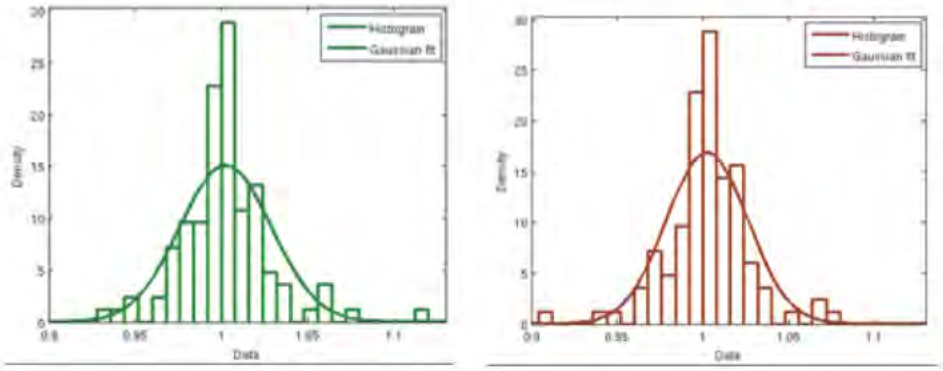

Figure 11.4: Comparison of ratios of various volumes in the FreeSurfer parcellation after filling in with the (a) SPM based method and (b) ANTS based method. The results are quite similar with both showing a mean close to 1 and similar standard deviation.

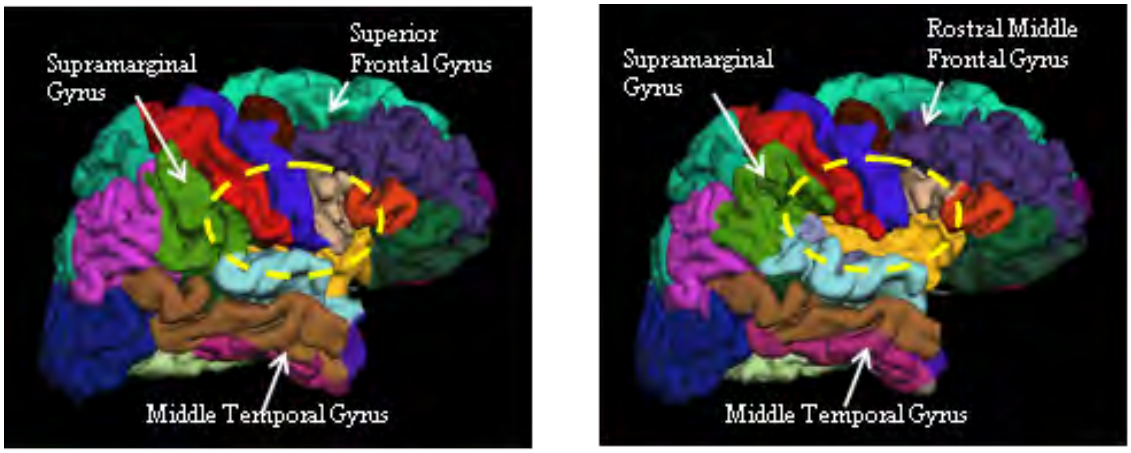

Figure 11.5: Comparison of FreeSurfer parcellation before and after filling in the stroke using SPM based approach. Dotted yellow circle indicates regions where infarct was present. Distal regions as well as proximal regions are observed to be affected significantly.

Part D

Statistical Analysis and Machine Learning

Chapter 12

Is Greulich and Pyle Atlas still a Good Reference for Bone Age Assessment?

Aifeng Zhang [a], Sinchai Tsao [a], James W. Sayre[b], Arkadiusz Gertych[a], Brent J. Liu[a], H.K. Huang[a]

[a] Image Processing and Informatics Lab, Department of Radiology, ISI/USC, Marina Del Rey, CA USA 90292;
[b] Department of Biostatistics and Radiological Sciences, UCLA School of Public Health, Los Angeles, CA USA 90095-1772

Medical Imaging 2007: PACS and Imaging Informatics, edited by Steven C. Horii, Katherine P. Andriole, Proc. of SPIE Vol. 6516, 65160T, (2007) 1605-7422/07/$18 doi: 10.1117/12.710160

1 Abstract

The most commonly used method for bone age assessment in clinical practice is the book atlas matching method developed by Greulich and Pyle in the 1950s. Due to changes in both population diversity and nutrition in the United States, this atlas may no longer be a good reference. An updated data set becomes crucial to improve the bone age assessment process. Therefore, a digital hand atlas was built with 1,100 children hand images, along with patient information and radiologists readings, of normal Caucasian (CAU), African American (BLK), Hispanic (HIS), and Asian (ASI) males (M) and females (F) with ages ranging from 0 18 years. This data was collected from Childrens Hospital Los Angeles. A computer-aided-diagnosis (CAD) method has been developed based on features extracted from phalangeal regions of interest (ROIs) and carpal bone ROIs from this digital hand atlas. Using the data collected along with the Greulich and Pyle Atlas-based readings and CAD results, this paper addresses this question: Do different ethnicities and gender have different bone growth patterns? To help with data analysis, a novel web-based visualization tool was developed to demonstrate bone growth diversity amongst differing gender and ethnic groups using data collected from the Digital Atlas. The application effectively demonstrates a discrepancy of bone growth pattern amongst different populations based on race and gender. It also has the capability of helping a radiologist determine the normality of skeletal development of a particular patient by visualizing his or her chronological age, radiologist reading, and CAD assessed bone age relative to the accuracy of the P&G method.

Keywords: Bone Age Assessment, Digital Hand Atlas, Web-based application, Computer-aided-diagnosis

2 Introduction

Pediatric bone age assessment is an important procedure that allows a physician to judge the degree of a patients skeletal bone development relative to the patients chronological age. Discrepancies between bone age and chronological can occur due to growth disorders that can stem from endocrine disorders or malnutrition. Accurate diagnosis is required to help determine proper treatment. The most commonly used method for bone age assessment in clinical practice is the book atlas matching method developed by Greulich and Pyle [80, 81]. This method is based on visual comparison of the patients hand x-ray with images collected in the atlas. The closest match is subjectively selected by the radiologist and yields the bone age of the patient (Figure 1). However the book atlas has not been updated since its initial publication in the early 1950s. The data collected in the original atlas was derived solely from upper middle class Caucasian populations residing in the midwest of the United States. Due to changes in both population diversity and nutrition in the United States, this atlas may no longer be a good reference. An updated data set has become crucial to improve the bone age assessment process. For this purpose, left hand X-ray films of normal children along with pertinent data related to patient growth factors were acquired at Childrens Hospital Los Angeles. [82, 83, 84] The data was divided into eight categories by race and gender. A computer aided diagnosis (CAD) method was developed based on features extracted from phalangeal regions of interest (ROI) and carpal bone ROI. [85, 86, 87, 88, 89] For data analysis, a web-based statistical visualization application was developed to help address the following issues: 1) Does each race have distinct bone growth patterns? and 2) More importantly, is the G & P atlas still a good reference for bone age assessment of todays children?

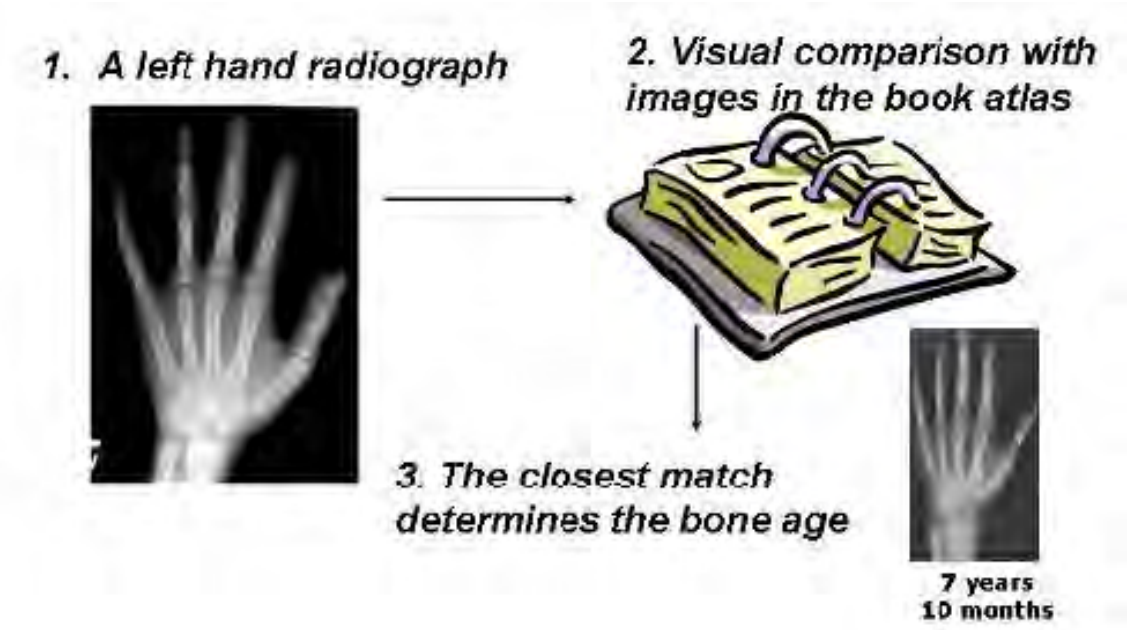

Figure 12.1: Bone age assessment procedure in clinical practice.

3 Methods and Materials

3.1 Data Collection

Building of the Digital Hand Atlas A digital hand atlas was developed with data from eleven hundreds children. This consisted of hand images collected from Childrens Hospital Los Angeles accompanied by patient information and radiologists readings. The data consisted of normal Caucasian (CAU), African American (BLK), Hispanic (HIS), and Asian (ASI) males (M) and females (F), with ages ranging from 0 18 years. [82, 83, 84] Each hand image and the subjects demographic data, along with two radiologists readings and CAD-based bone age were populated into a mysql database. The database was integrated with a web server at the Image Processing and Informatics Laboratory, USC. To simplify statistical testing as well as data visualization, the two radiologists readings

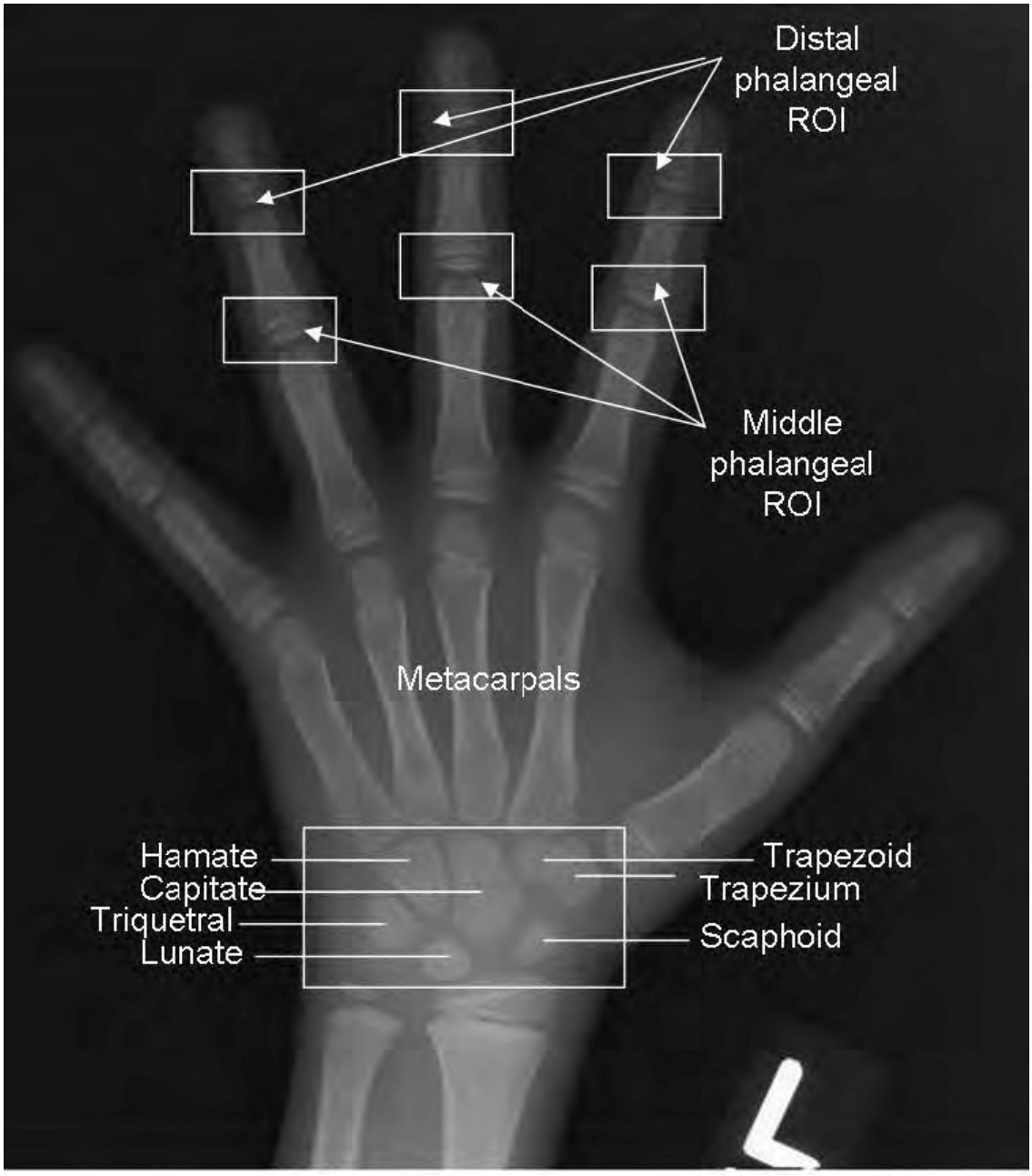

Figure 12.2: Sample Hand Image from the CHLA data collection process. All pertinent bones that were used as ROIs in the CAD program are labeled.

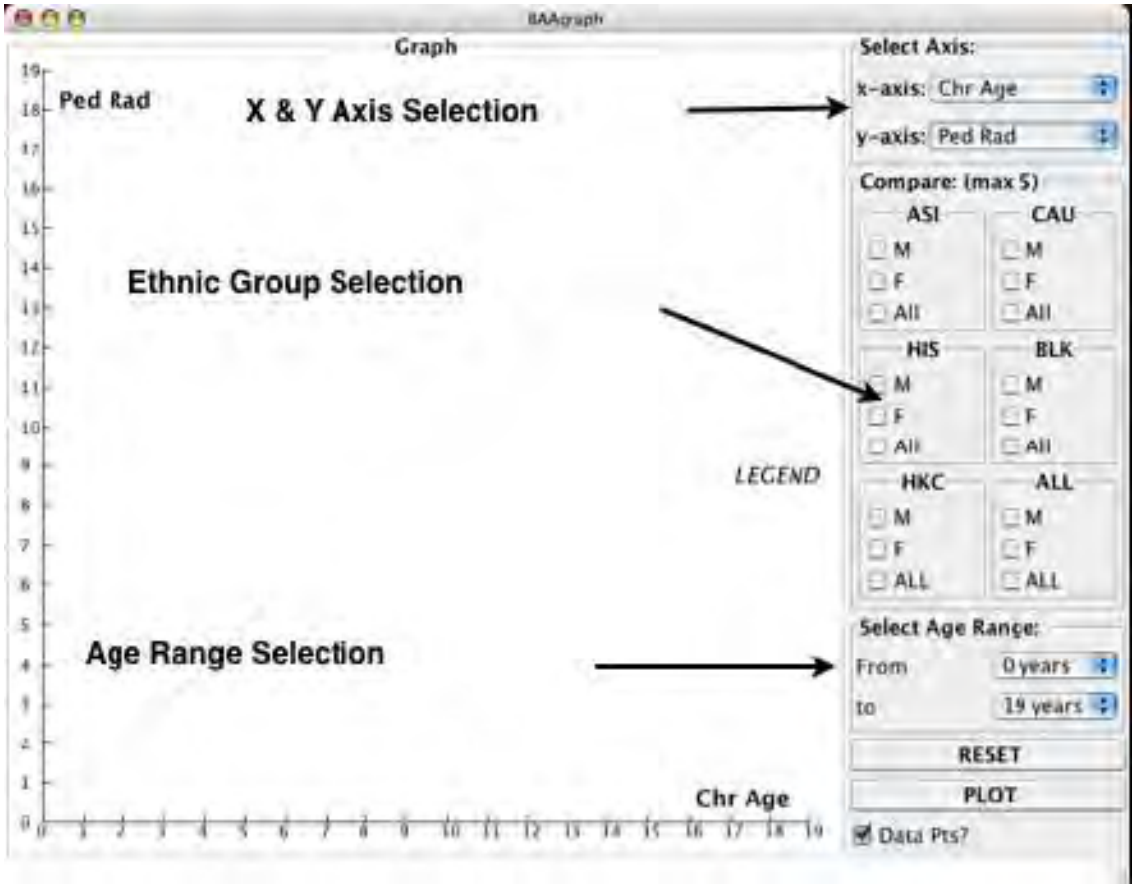

Figure 12.3: Simple GUI to visualize differences between the different Study Groups.

were averaged to get one reading-based age per subject. Figure 2 is a sample hand image with phalangeal and carpal ROIs outlined.

3.2 Data Visualization - Web GUI (Graphical User Interface) Development

A separate JAVA applet-based platform-independent software was developed to assess relevant data in the Digital Hand Atlas database and to plot results. The GUI programs

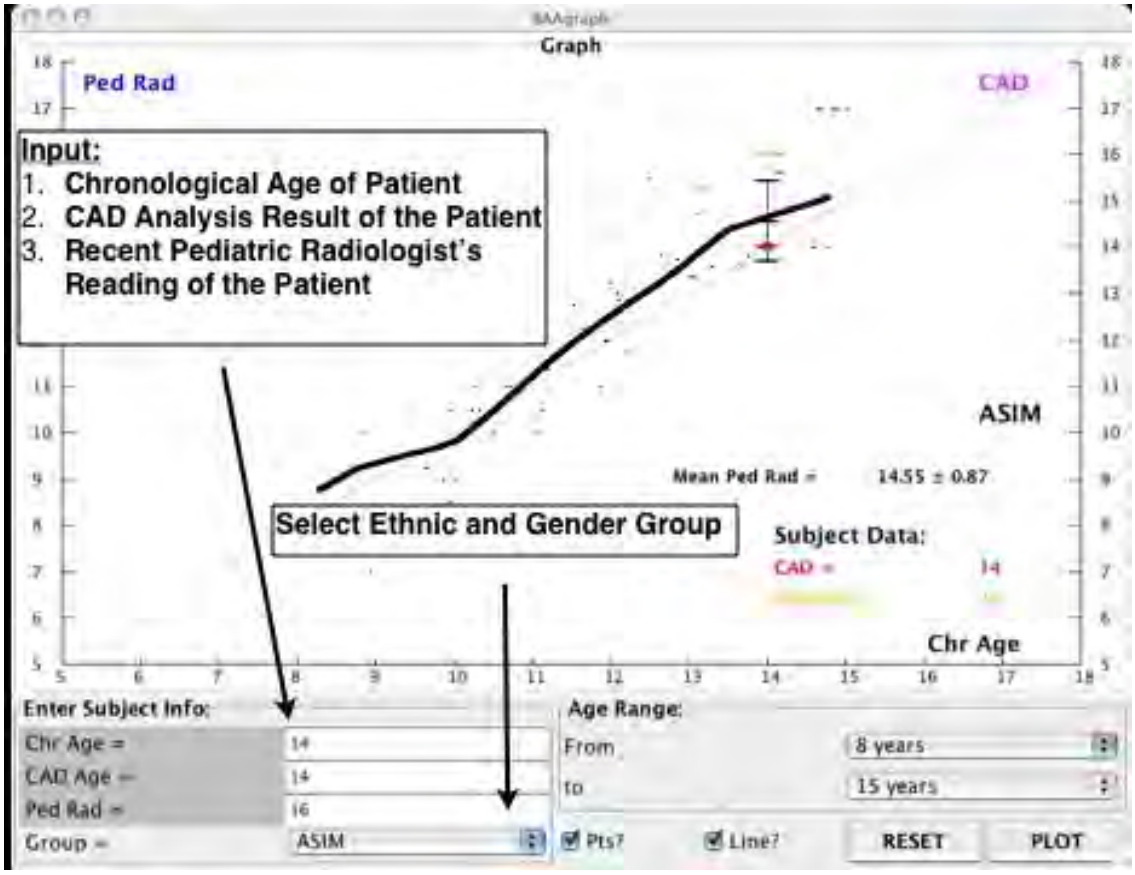

Figure 12.4: Clinical GUI to compare a patients CAD and Radiologists Readings relative to the accuracy of the Radiologists Readings from the Digital Hand Atlas Database. The three black horizontal lines bisected by the vertical line marks the mean as well as the upper and lower standard deviation of the pediatric radiologists G&P-based readings of normal cases with that specific chronological age. The yellow marker represents the radiologist reading of the current case. The red marker represents the CAD output of the current case. The GUI allows the user to assess the CAD and Pediatric Radiologists readings against the accuracy of the gold standard - the accuracy of G&P readings of the normal cases in the database. Any reading variation away from the chronological age that is greater than the accuracy as set by the gold standard indicates a possible growth disorder.

were developed to compare Pediatric Radiologist Readings, CAD results with Chronological Age amongst different racial and gender groups. The first GUI program (see figure

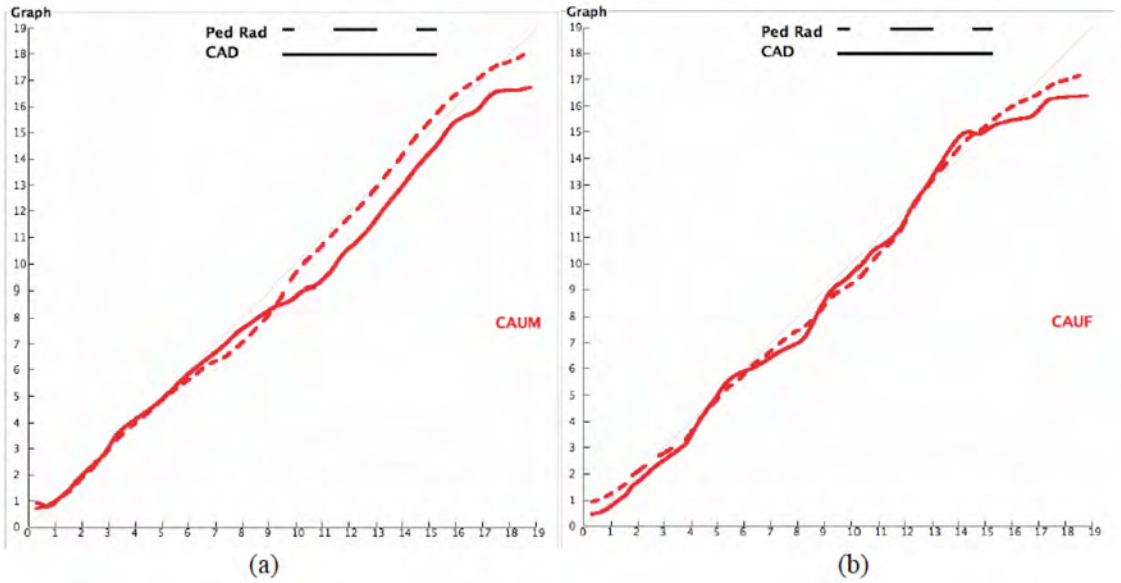

Figure 12.5: The figure illustrates that gender effects bone age assessment with both reading and CAD methods. (a) Caucasian male; (b) Caucasian female. The x-axis is chronological age and the y-axis is either radiologists reading or CAD result.

2) was used as a tool to plot graphs with the users choice of Radiologists Readings, CAD-based result or Chronological age as the X or Y axis. The JAVA applet runs on a web server of choice and connects to a mysql database on the same machine for its input data. [90, 91] A php script that connected to the mysql database was used as an intermediary data source for the JAVA applet. The JAVA applet passes the necessary inputs to the php script, which then retrieves the relevant information from the database without compromising data integrity. One feature of this design is that as the data is updated in the database, the graphing output will change accordingly. In this study, four comparison studies based on the specific population combinations were conducted using this GUI: 1) All eight categories are individually compared, 2) Male and Female are combined to form four ethnic groups for comparison, 3) All male and all female are combined to form

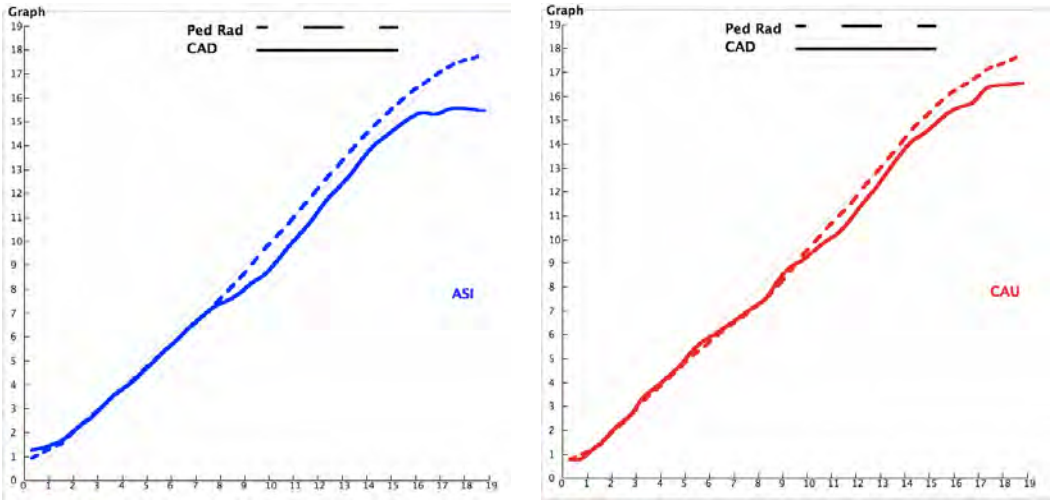

Figure 12.6: The figure illustrates that ethnic or racial origin effects bone age assessment with both the reading and CAD methods. (a) Asian; (b) Caucasian. The x-axis is chronological age and the y-axis is either radiologists reading or CAD result. The x-axis is chronological age and the y-axis is radiologists reading.

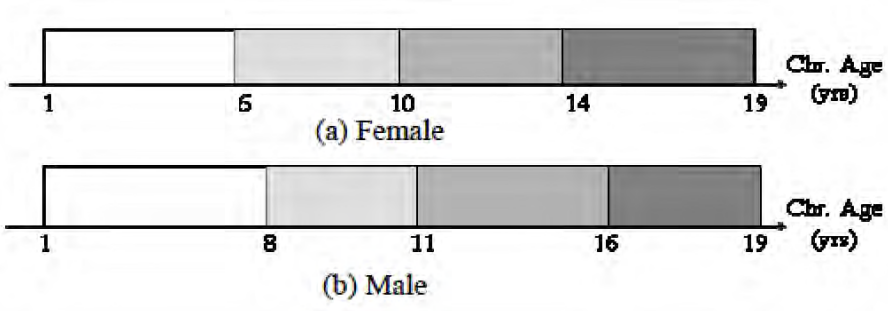

Figure 12.7: The divided age sets in evaluation. (a) for female and (b) for male.

two gender groups for comparison, and 4) All eight categories were combined to form one group.

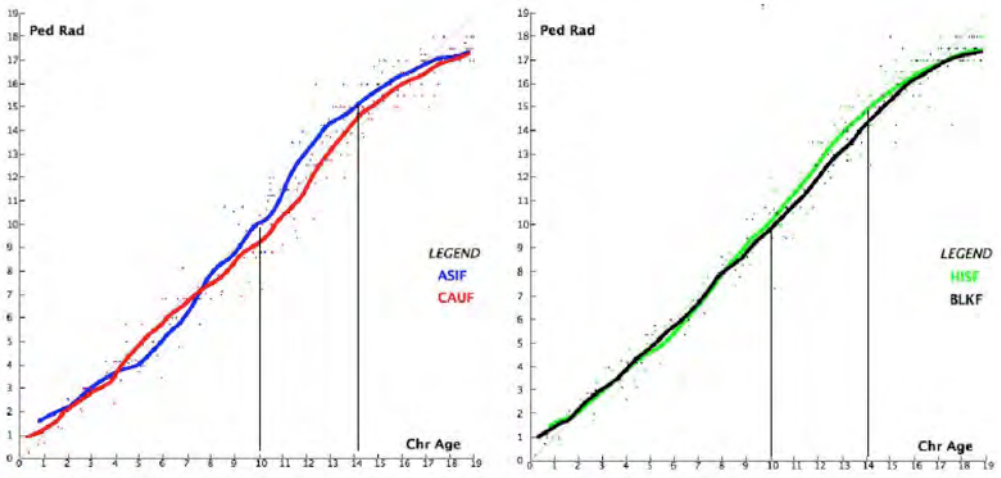

Figure 12.8: Plots of readings between race pairs (a) Asian female and Caucasian female; (b) Hispanic female and African American female. The x-axis is chronological age and the y-axis is radiologists reading.

3.3 Prototype of a Clinically Applicable GUI

To demonstrate the clinical viability of the CAD methodology, a second GUI was developed to allow the user to visualize the current patients data against information in the database. The mean and standard deviation of the radiologists readings of the normal cases in the database for that particular chronological age is shown along with the current patients results. If the CAD assessed bone age or the Pediatric Radiologist Readings falls outside of the range of error, the patient could have a case of suspected abnormal bone development. (see figure 3)

4 Results

4.1 Plots

The plotting application allows users to visualize the normal data from the digital hand atlas, by race, gender or combination among race and gender. Figures 4-5 shows the output of the web applet when using CAD and Readings against Chronological Age. However, the user can compare a particular patient using any three inputs: Chronological age, Radiologists readings and CAD assessed bone age. In this section, general trends shown from the graphical plots will be outlined. Statistical studies will be outlined in the following section. Comparing radiologists readings and CAD results versus chronological age, the graphs show that ethnicity and gender does have influence on the growth pattern as shown by the variability of both CAD results as well as radiologists reading in figure 4. Variation in both the radiologists reading and the CAD results between the different gender (figure 6) and different ethnic groups (figure 5) show that both ethnicity and gender have an independent effect on bone age assessment. With gender, it is well documented that females bone structure variations end earlier, making it more difficult to differentiate between the later age groups. However, the use of different ethnic groups / populations is novel. Assessing the G&P-based Radiologists readings, it can be seen that it correlates well with chronological age (see figure 7), except at later ages. This can be primarily attributed to the lack of variation in older females (see figure 6). The CAD method sensitivity decreases at age 15+ (see figure 7). This is attributed to the lack of variation in the current ROIs. At the time of writing of this paper an addition ROI, the Radius, with known variation from 15-19 years is being added to remedy this problem.

4.2 Statistical analysis between races

To study the discrepancy between races, paired-samples t-test was performed between the chronological age and the average of two readings. Table 2 shows the mean difference between average reading and chronological age for eight categories by race and gender. The numbers with an asterisk represents a difference with a significant p-value of $<$ .05. As we can see from Table 2, radiologists using the G&P atlas are able to assess bone age very accurately for the African American sample population and the Caucasian male sample population. However, significant discrepancies were observed in Asian and Hispanic groups. To study this in greater detail, the entire age range was divided into four age groups. The Males and Females were divided in differently according to Figure 6. Comparisons of the difference between radiologists average reading and chronological age for two races was conducted by analysis of variance (ANOVA). The results for the four age sets are presented in Table 3 for female and Table 4 for male. As the data in Table 3 shows, significant mean differences of readings between races are observed at age group from 10-14 years old. Radiologist over-read Asian cases by approximately 0.80 years compared with their African American and Caucasian peers. In the same fashion, over-reading was observed between the Hispanic and African American groups. Figure 6 shows the plots of readings between the Asian female population and the Caucasian female population as well as the Hispanic female and African American female populations. For the male populations from the digital atlas, significant differences were the groups ranging from 11 to 16 years of age. In comparison with the African American population, Radiologists tends to over-read Asian and Hispanic cases about a year. (Figure 7)

5 Conclusions

The aforementioned study represents a novel statistical analysis of bone age assessment for differing gender and ethnic populations. Through the study we attempted to answer the following questions: 1) Does each race have distinct bone growth patterns? and 2) Is the G & P atlas still a good reference for bone age assessment of todays children? Addressing the first question, the hypothesis is that genetic differences with influences from diet and nutrition may cause variation in growth patterns, thereby influencing the bone age assessment process. The statistical analysis (Section 3.2) discovered significant differences for Asian and Hispanic ethnic populations, which to a certain extent nullifies the null hypothesis. This therefore illustrates that the accuracy of the Greulich and Pyle atlas can indeed be improved by taking ethnic population and gender into account. This potential can be captured by a CAD trained to adapt to reading images of different genders and populations as previously outlined. The answer to the latter question is that until this CAD methodology is complete and compared against the Greulich and Pyle method, the extent of which patient demographic background can be exploited to give a more accurate bone age assessment cannot be fully determined.

Acknowledgements

This work has been supported by NIH R01 EB 00298

Table 12.1: Total of 1,103 cases from first Cycle Data Collection

Age group/Category	ASIF	ASIM	BLKF	BLKM	CAUF	CAUM	HISF	HISM
00	1	2	4	5	3	3	1	4
01	5	5	5	5	5	5	5	5
02	5	5	5	5	5	5	5	5
03	5	5	5	5	5	5	5	5
04	5	5	5	5	5	5	5	5
05	5	5	5	5	5	5	5	5
06	5	5	5	5	5	5	5	5
07	5	5	5	5	5	5	5	5
08	5	5	5	5	5	5	5	5
09	5	5	5	5	5	5	5	5
10	10	10	10	10	10	10	10	10
11	10	10	10	10	10	10	10	10
12	10	10	10	10	10	10	10	10
13	10	10	10	10	10	10	10	10
14	10	10	10	10	10	10	10	10
15	10	10	10	10	10	10	10	10
16	10	10	10	10	10	10	10	10
17	10	10	10	10	10	10	10	10
18	10	10	10	10	10	10	10	10
Total	136	137	139	140	138	138	136	139

Table 12.2: CAD evaluation for eight categories by race and gender. Values in the table represent the mean difference between chronological age and the average reading in year. Significant mean difference is indicated by an asterisk.

Mean Difference	**ASI**		**BLK**		**CAU**		**HIS**	
with Chr. Age	**F**	**M**	**F**	**M**	**F**	**M**	**F**	**M**
Average Reading	-.20*	-.45*	-.02	.01	.16*	-.03	-.22*	-.37*
No. of Cases	129	132	127	124	134	130	128	126

* p value < 0.05

Table 12.3: Cross racial comparison of chronological age vs. reading for female. Each block was divided into four subblocks, each of which encompasses one age set. (unit: year, -: over read)

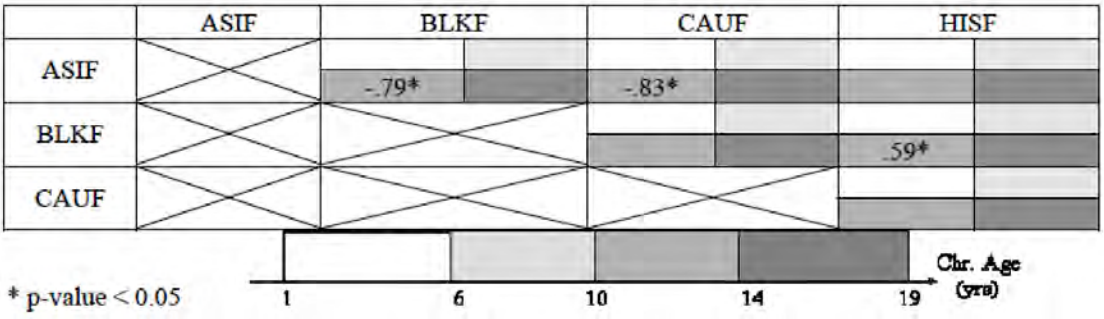

* p value < 0.05

Chapter 13

Automated Bone Age Assessment of Older Children using the Radius

Sinchai Tsao [a], Arkadiusz Gertych[b], Aifeng Zhang [a], Brent J. Liu[a], H.K. Huang[a]

[a] Image Processing and Informatics Lab, Department of Radiology, ISI/USC, Marina Del Rey, CA USA 90292;
[b] Department of Surgery, Minimally Invasive Surgical Technologies Institute, Cedars-Sinai Medical Center, 8700 Beverly Blvd, Davis 4021, Los Angeles, CA 90048, USA

Medical Imaging 2008: PACS and Imaging Informatics, edited by Katherine P. Andriole, Khan M. Siddiqui, Proc. of SPIE Vol. 6919, 69190E, (2008) 1605-7422/08/$18 doi: 10.1117/12.770018

1 Abstract

The Digital Hand Atlas in Assessment of Skeletal Development is a large-scale Computer Aided Diagnosis (CAD) project for automating the process of grading Skeletal Development of children from 0-18 years of age. It includes a complete collection of 1,400 normal hand X-rays of children between the ages of 0-18 years of age. Bone Age Assessment is used as an index of skeletal development for detection of growth pathologies that can be related to endocrine, malnutrition and other disease types. Previous work at the Image Processing and Informatics Lab (IPILab) allowed the bone age CAD algorithm to accurately assess bone age of children from 1 to 16 (male) or 14 (female) years of age using the Phalanges as well as the Carpal Bones. At the older ages (16(male) or 14(female) -19 years of age) the Phalanges as well as the Carpal Bones are fully developed and do not provide well-defined features for accurate bone age assessment. Therefore integration of the Radius Bone as a region of interest (ROI) is greatly needed and will significantly improve the ability to accurately assess the bone age of older children. Preliminary studies show that an integrated Bone Age CAD that utilizes the Phalanges, Carpal Bones and Radius forms a robust method for automatic bone age assessment throughout the entire age range (1-19 years of age).

Keywords: Bone Age Assessment, CAD, Image Processing, Skeletal Imaging

2 Introduction

2.1 Current Issues in Bone Age Assessment Methods

Bone Age Assessment is used in Pediatrics to determine the stage of a subjects bone maturity during its growth from 0 to 19 years of age. Delayed or accelerated bone growth relative to a childs chronological age may be an indication of a pathological growth pattern. Examples of diseases that may cause pathological growth patterns include growth hormone deficiency, hypothyroidism, Sotos syndrome and other genetic and non-genetic pathologies. The Greulich and Pyle atlas published in 1950 form the basis of clinical bone age assessment. Radiologists use the hand radiographs of children from the GP atlas along with descriptions of hand bone growth stages to assess a patients bone age. Other more recent but less commonly used methods include the Tanner and Whitehouse or TW2 Method developed in 1975. However both methods require the Radiologist to compare and manually judge stages of growth relative to an atlas. Our CAD method attempts to quantify features that correlate well with bone maturity and growth and completely automate the process of bone age assessment.

2.2 Previous Work

Previous work by Pietka, Gertych, Pospiech-Kurkowska, et al [92] used the Phalanges as the ROI for feature extraction. The dynamic changes in the Phalanges in children between the ages of 7 to 16 (male) or 14 (female) years of age provided information for bone maturity assessment within this age range. Later work by Zhang et al [89] using size and shape-based features of the Carpal Bones allowed for assessment of younger children. To allow for complete assessment of Bone Age in all children, another ROI was necessary.

The Radius was chosen as the ROI of choice for older children because of its late fusion of the proximal Metaphysis and distal Epiphysis. This phenomenon is documented in the Greulich and Pyle Atlas as being later in the Radius as compared to the Phalanges. Thus allowing for assessment in the degree of fusion at the older age range using wavelet transformation based features similar to those used in the Phalanges. Due to the differing morphology between the Phalanges and the Radius, however, a new methodology is still necessary to extract the smaller sub-image of the growth plate region that will be used for feature extraction via wavelet transform. This segmentation technique is based on knowledge about the generalized morphology of the wrist. Using this knowledge along with defined landmarks, the Radius is identified and the bounding box for the sub-image is segmented from the larger wrist ROI.

3 Methods

3.1 Localizing the Radius

This initial methodology was developed based on previous work in the phalangeal ROI in the hand. The wrist region is segmented from the overall image via a set of landmarks based on the location of the Phalanges and the hand midline. The wrist ROI is then extracted as shown in figure 1. Through textural analysis, the pixels are grouped into three subtextures (Bone, Soft Tissue and Background) as shown in the second image in figure 1. The bone-based texture is then removed from the other two textures. A binary image shows the location of all pixels that are part of that texture group. Using knowledge of the morphology of the wrist, the Radius is selected from all other bone structure and an overall outline of the bone is formed using image processing techniques such as erosion

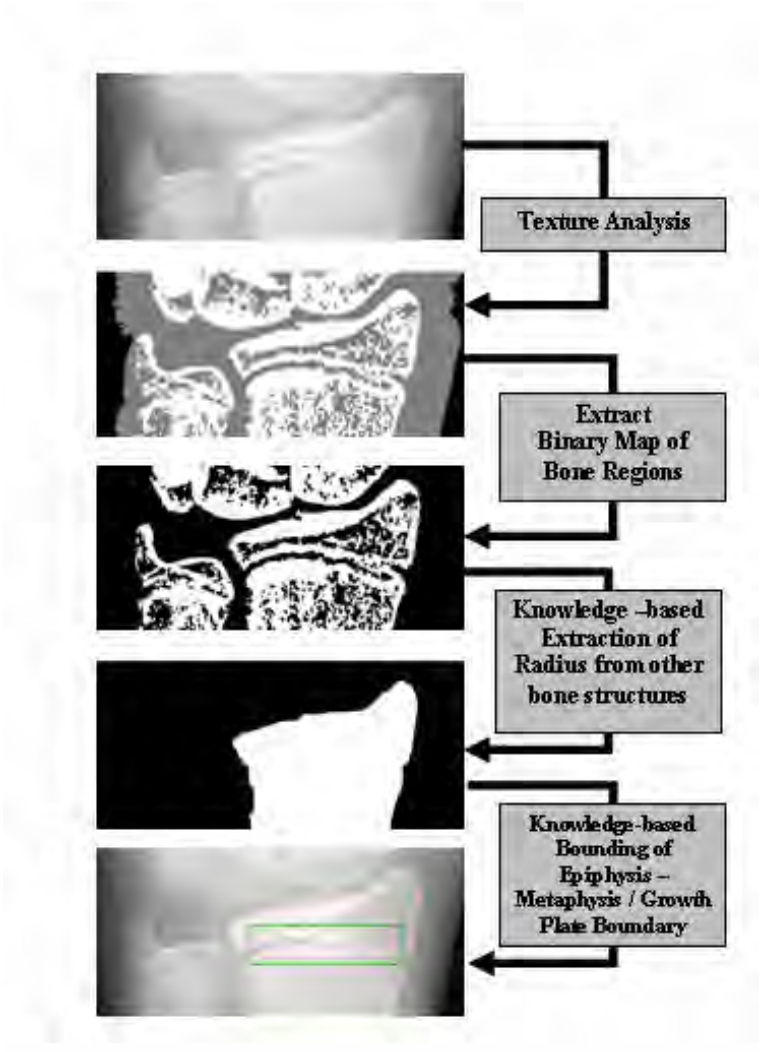

Figure 13.1: Outline of Image Processing algorithm to extract Growth Plate ROI from the larger Wrist ROI.

and dilation. In addition, knowledge of the location of the Epiphysis and Metaphysis of the Radius allows missing smaller structures that may be identified as separate objects to be merged to form the image of the Radius as seen in image number 4 in figure 1. Using the width and centerline of the Radius, a box containing the growth plate is drawn

Figure 13.2: Enlarge Image showing the extracted Growth Plate ROI. Note the horizontal pattern that denotes the boundary between the epiphysis and metaphysis. This boundary lessens and eventual disappears as the child grows.

automatically by the CAD algorithm. The subimage extracted from the segmentation process illustrated by figure 1 is shown in figure 2.

3.2 Features Extraction

After the growth plate ROI is segmented (figure 2), the sub-image is then passed onto the features extraction algorithm, which calculates the energy, orientation and number of edges in the sub-image and provides 12 quantitative measurements using the wavelet transform developed for the phalanges [92]. Six of the features that show most correlated variation with bone maturity are selected and passed on to a Mamdani fuzzy inference system. For each feature, a set of membership functions are formed from training using 48 images from males of ages 14 to 18 years of age. Using statistical analysis of feature values between age groups of 14, 15,16,17,18 and 19 years, groups that showed too much variation were merged.

3.3 Fuzzy Classification and Computation of Bone Age

The feature set for the images are divided into the two male and female cohorts for bone age computation, since the growth patterns and in male and female children are different[93]. For each feature, a set of 3 to 6 Gaussian membership functions were formed using the standard deviation and means from the data. Each of these membership functions represented a specific age group and depending on the feature value will contribute to each of the computed bone age output differently. A set of simple aggregation rules dictated how the membership functions were aggregated into the output membership function. The output membership functions were also Gaussian-based and depended on the standard deviation and mean of the chronological age of the 149 image training set. For our preliminary system testing we used the same image set for training and testing.

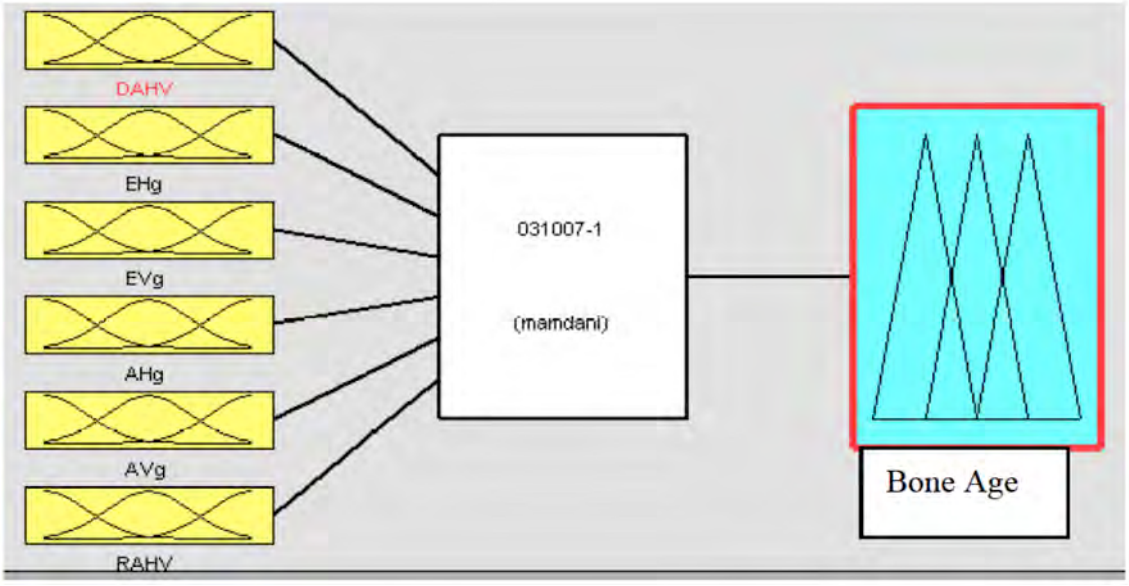

Figure 13.3: Mamdani Fuzzy Inference System used to aggregate the feature values and derive a Bone Age based on feature values. The system requires training with a data set of normal children.

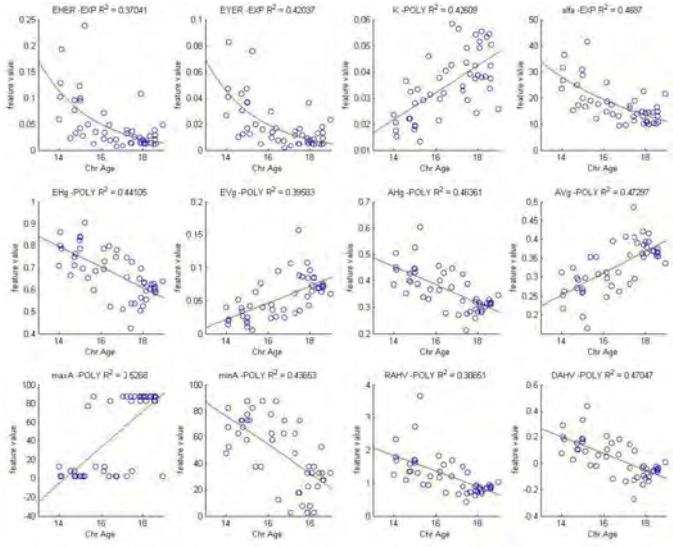

Figure 13.4: Feature values for the male cohort.

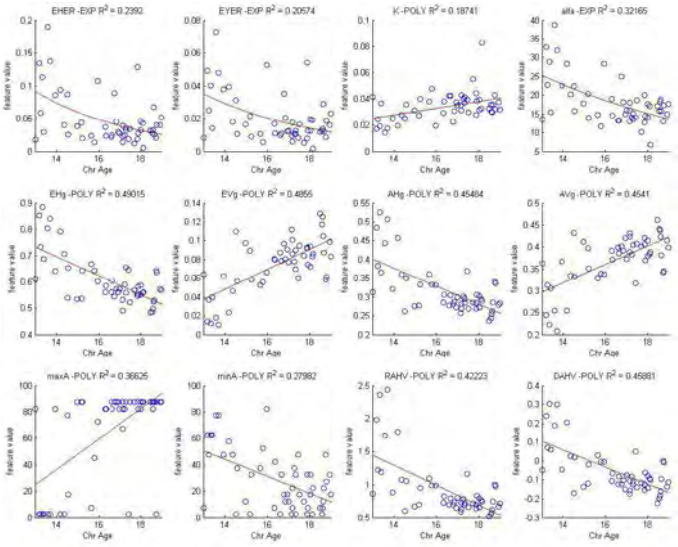

Figure 13.5: Feature values for the female cohort.

4 Results

With our initial test group of Caucasian Children between the ages of 14 and 19, there were 149 images that were used for testing. The chronological age of these children does

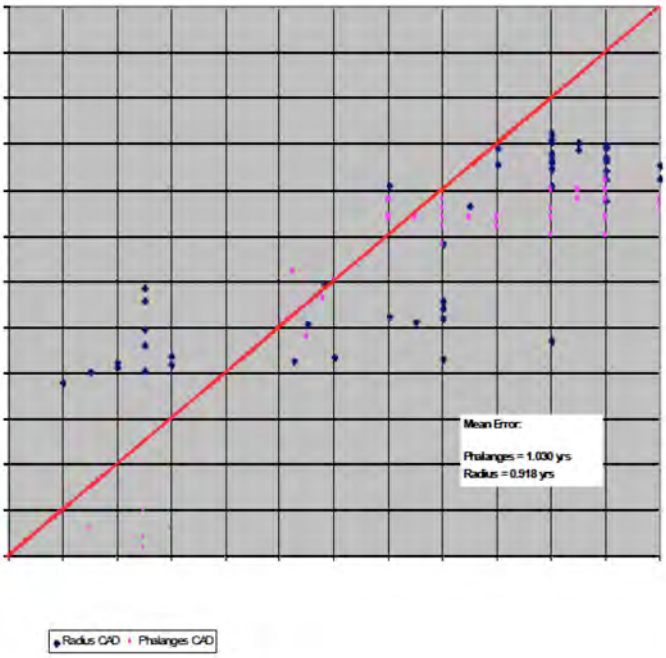

Figure 13.6: CAD Age versus Pediatric Radiologist's Reading for the Male Cohort

Table 13.1: Mean Absolute Error of the system for the Male Cohort using Phalanges and Radius based on the Chronological Age and Reading of the Pediatric Radiologist as the gold standards. The absolute mean difference for the male cohort between the Pediatric Radiologists reading and the normal childs chronological age is 0.650 years.

	Phalanges	Radius
ChrAge	1.246 yrs	0.814 yrs
Reading	1.030 yrs	0.918 yrs

not differ more than 3 years from the projected bone age that the Pediatric Radiologist determined. The Caucasian Children also provide us with homogeneity in ethnic background in our dataset in case there are differences in growth patterns due to ethnic background. From previous experience we also found that the Caucasian dataset has

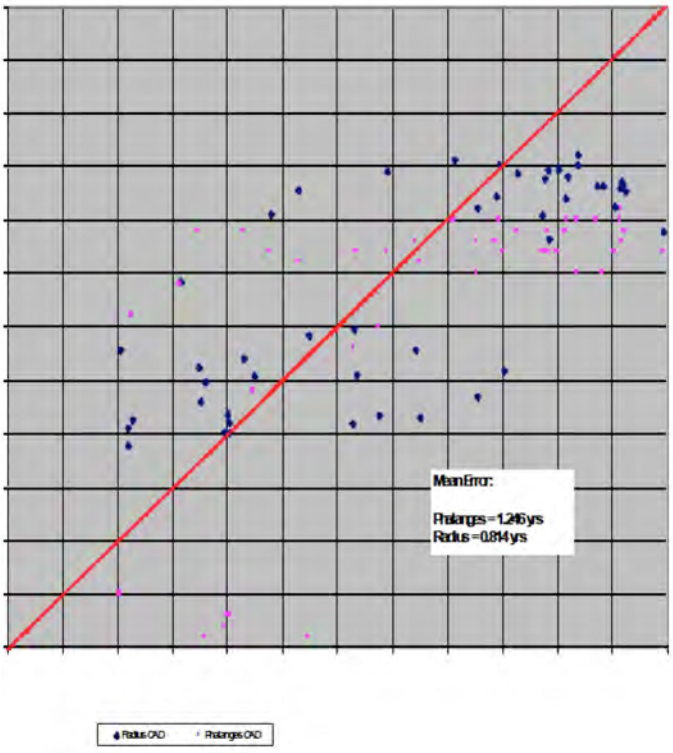

Figure 13.7: CAD Age versus Chronological Age for the Male Cohort

Table 13.2: Mean Absolute Error of the system for the Female Cohort using Phalanges and Radius based on the Chronological Age and Reading of the Pediatric Radiologist as the gold standards. The absolute mean difference for the female cohort between the Pediatric Radiologists reading and the normal childs chronological age is 0.700 years.

	Phalanges	Radius
ChrAge	1.583 yrs	1.156 yrs
Reading	1.181 yrs	0.908 yrs

the most consistent in image quality. Our initial results show that we were able to correctly segment out the growth plate region approximately 50% of the time. Errors were a result from (1) an inability to differentiate between the carpal bones and the radius

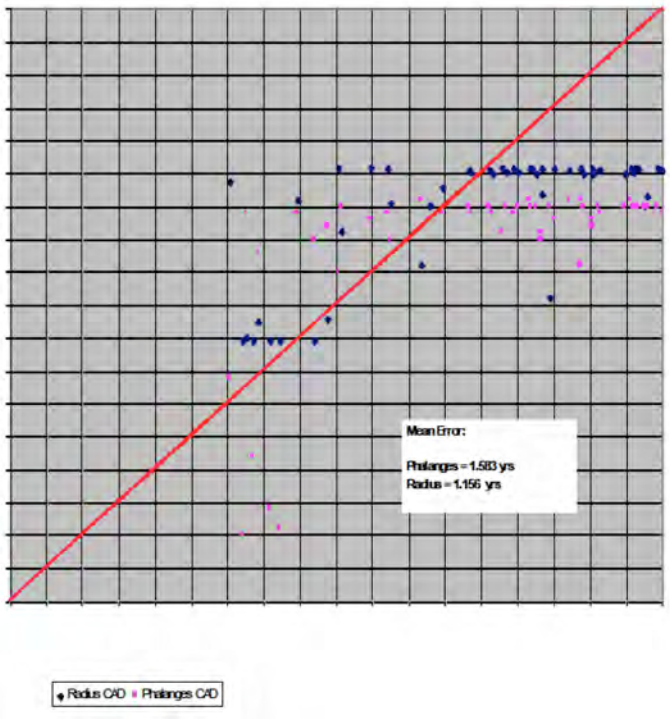

Figure 13.8: CAD Age versus Pediatric Radiologist's Reading for the Female Cohort

(2) mistaking the Ulna for the radius (3) unable to locate the growth plate sub-region of the carpal bone accurately. More work needs to be done to improve the accuracy of segmentation or have fail safe mechanisms when the Radius or the growth plate region cannot be segmented. In the final integrated system, images where the Radius cannot be used will rely on the phalangeal data for bone age assessment. The results of the feature extraction are shown in figure 3 and 4, correlation coefficients are calculated from either a linear regression or exponential regression depending on the feature and were indicated by either POLY for linear polynomial or EXP for exponential. We chose to use both measures because the fuzzy inference system was able to mimic both types of trends during training. The trends indicate that the features allow for differentiation between the lower

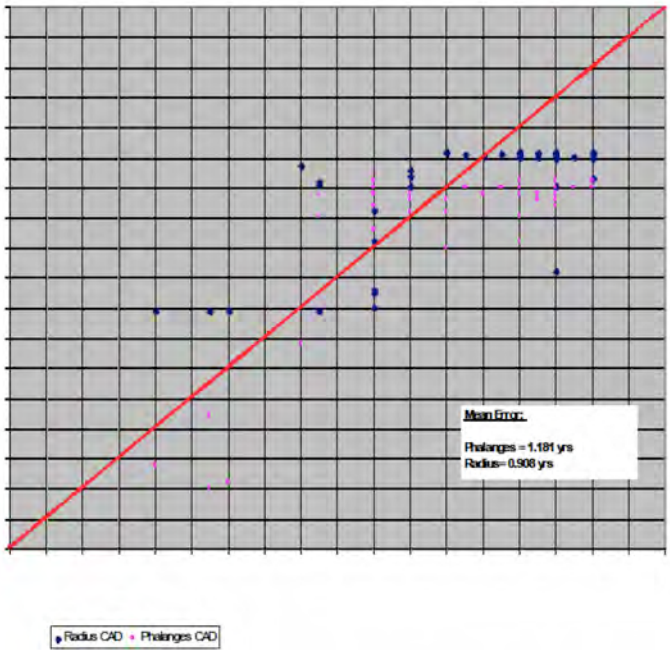

Figure 13.9: CAD Age versus Chronological Age for the Female Cohort

age range of 14 to 15 and the higher age range of 17 to 19 years of age but not any higher in age range resolution. Figures 6 to 9 shows our preliminary results of the system after the fuzzy inference engine has computed the bone age based on the radius features. The computed CAD bone age for the new Radius results and the previous Phalangeal results are compared to the chronological age as well as the Radiologists Readings. Tables 1 and 2 show the generalized error for the overall testing set. Relative to chronological age, the new system showed a decrease of about 0.3 years for males and 0.4 years for females.

5 Discussion

The GP atlas acknowledges natural growth variation in males from 14 to 17 years of age to have a standard deviation of 10.72 to 13.05 months. [93] Therefore, any variation of

our result to within the order of 1 year can be attributed to natural variation in the population. In addition, our current system based on the Phalanges tapers off at 16 years of age for females and 17 years of age for males. Therefore any ability to differentiate between the pre-16 or pre-17 years of age and the higher age group of 18 and 19 will be contributed significantly to the overall fuzzy bone age result. This is because final system integration will allow the Phalangeal features to be aggregated with the Radii features and weighed using the fuzzy inference system to yield a final CAD bone age result. The R-squared correlation coefficients for Radius are much lower than that of the Phalanges (approx 0.8 and above) for their optimal operational age range from 5 to 14 years. The computed bone age results show the effects of the lack of correlation in the features. Relative to the gold standard of the chronological age, it shows a stepwise output, with many of the computed bone ages clustered at 15.5 years and 17.5 years. The system however still show improvements over the Phalanges in this age range but most likely reflect the fact that Phalanges have already fully developed at this age range and no longer have enough variability for bone age assessment.

6 Future Work

The current image segmentation techniques have a high failure rate (50 %), improvements can be made looking at current error cases. Common problems include mistaking the Ulna for the Radius and having an incomplete segmentation of the Radius. Adding improvements to the current image segmentation algorithm will decrease the failure rates and increase the accuracy of the segmentation. The features are highly sensitive to whether

the demarcation of the epiphysis and metaphysis is captured therefore better segmentation will yield better feature values. For CAD system to have accuracy over the entire 0-19 year age range, the radii information has to be integrated with the current system that uses the carpal and phalangeal information for Bone Age Assessment. How this will be done and to ensure maximum reliability and performance has yet to be determined. The difficulty lies in the fact that at lower age ranges the current Radii methodology will not work as a method to determine bone age, similarly the carpal data will not work on older children, therefore, a reliable method must be developed to cover the whole age range by efficiently aggregating information from each of the different regions.

Acknowledgements

The authors would like to thank National Institutes of Health for their support of this research as well as the Society of Imaging Informatics in Medicine for their continuing support for this project through their imaging informatics training grant.

Chapter 14

Evaluating the Predictive Power of Multivariate Tensor-based Morphometry in Alzheimers Disease Progression via Convex Fused Sparse Group Lasso

Sinchai Tsao[a] Jiayu Zhou[b] Jie Shi[b] Jieping Ye[b] Yalin Wang[b] Natasha Lepore[a]

[a]University of Southern California and Children's Hospital Los Angeles, Los Angeles, California, USA
[b]Arizona State University, Phoenix, Arizona, USA

Submitted SPIE Medical Imaging 2014

1 Abstract

Previous work by Zhou et al. 2013[100] has shown that a multi-task learning framework can be used to encode both sparsity as well as temporal smoothness in predicting cognitive outcomes of Alzheimer's Disease Neuroimaging Initiative (ADNI) subjects based on MRI baseline features as well as other subject information. Wang et al. 2013[101] has developed a multivariate tensor-based morphometry (mTBM) features based on parametric surface analysis for sparsifying machine learning methods. They have shown these features when applied to the cortical surface outperforms standard volumetric or other features when used for disease classification. This study aims to combine this multi-task framework with novel multivariate tensor-based morphometry applied on to hippocampus surface to improve prediction performance of cognitive scores 6, 12, 24, 36 and 48 months from baseline. The hippocampus has been well studied in relation to AD and suggests that mTBM analysis should give us a highly accurate assessment of cognitive outcomes. We also assess the predictive power of these novel features relative to existing imaging-based features provided by FreeSurfer as well as non-imaging features such as age, sex, baseline test scores and genetic information.

Keywords: Alzheimers Disease, Disease Progression, Multi-task learning, fused Lasso, ADAS-Cog, Tensor-based Morphometry, Hippocampus, Feature Selection

2 Introduction

Recent work in psychological testing[102], genetic studies[103], magnetic resonance (MR) imaging[104], positron emission tomography (PET) imaging[105], cerebral spinal fluid (CSF) measurements[106], cardiovascular status[107] and others have yielded tremendous amounts of diagnostic data for diagnosing and staging dementias, especially Alzheimers disease (AD). Moreover, many of these studies now also include longitudinal information[108, 102]. This has lead to a problem often referred to as the curse of dimensionality, where the size (number of dimensions) of the dataset make it difficult to do various numerical analysis on the data, thereby making it to draw all-inclusive conclusions from the dataset. Statistical analysis together with clinical disease models have helped with determine how the different sets of diagnostic information interacts with one another but they require a large number of ad hoc assumptions and therefore does not lend itself well to large scale Medical Imaging-based features. These problems become even more important when trying to use Machine Learning techniques because the predictive power of the machine learning model decreases as the number of dimensions increases when the number of dimensions becomes too large. The question is then about how to select the "correct" features to maximize predictive power. This paper leverages existing sparsifying machine learning techniques with temporal priors[100], built specifically for progressive disease models, such as AD, together with multivariate tensor-based morphometric (mTBM) features [101] of the Hippocampus to try and predict AD progression up to 48 months from the baseline MRI measurement. The goal is to evaluate the predictive power of mTBM against those of cortical thickness and other FreeSurfer-based features, demographic information (sex and age) as well as genetic information (ApoE-ϵ4 Copies).

There are a variety of machine learning methods that can be used to predict cognitive outcomes using large-scale imaging features. A number of single task techniques such as Ridge and Lasso have been used to predict different future time points from baseline data. These single task operations, however ignore, useful temporal priors such as temporal smoothness in cognitive scores. Multi-task learning offers an opportunity to include temporal information but only perform well with a small number of features. To this end, Zhou et al 2013[100] formulated a multi-task learning framework that incorporated temporal smoothness of the output estimates of cognitive score changes in time as well as encodes sparsity in it's feature selection by employing a fused Lasso penalty that is smooth in time.

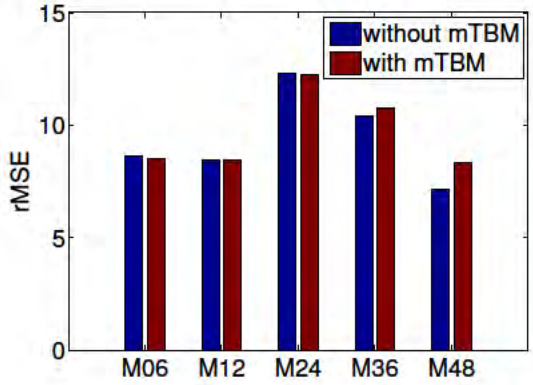

Figure 14.1: Bar Chart of the rMSE of predictions with and without mTBM features by time point

3 convex Fused Sparse Group Lasso (cFSGL)

Zhou et al 2013 [100] has proposed a powerful multi-tasked learning technique that incorporates sparsity as well as temporal smoothing for modeling a progressive disease model.

In their formulation, each tasked can be though of a single forward predictor from baseline measurement to a measurement at a certain future time point. In their case, they used the ADNI dataset and predicted ADAS cognitive scores 6 months after baseline (M06), 12 months after baseline (M12), 24 months after baseline (M24), 36 months after baseline (M36) and 48 months after baseline (M48). In our study we aim to use the same ADNI dataset but also incorporate mTBM hippocampus features and compare it to features used in their study. We also attempt to combine the different feature sets to try to evaluate the predictive power of each set of features.

The proposed cFSGL can be considered a multi-task regression problem with t time points and from n subjects each with d features, where $\{x_1, x_2, \ldots, x_n\}$ represents each of the d input features for each subject at baseline (i.e. $x_i \in \mathbb{R}^d$). Similarly, $\{y_1, y_2, \ldots, y_N\}$ represents the target cognitive scores for each subject at N time points (i.e. $y_i \in \mathbb{R}^N$). For a single subject (n) each task can be seen as a projection of MR / demographic / genetic baseline measurements at $t = 0$ represented at x_n to a future cognitive score measurement at time $t = t_1$ (e.g. at 48 months) given by $y_n(t_1)$. We can extend this formulation to a multi-task one by performing projections of all time points simultaneously. In other words, each set of baseline measurements at $t = 0$ given by x_n is projected to a vector ($\mathbb{R}^N$ with N time points) given by y_1. The entire mapping can be summarized as a linear operation using matrices X and Y. X and Y is formed by arranging the patient feature space row-wise, each row being x_n or y_N, and yields a $\mathbb{R}^{n \times d}$ X matrix and a $\mathbb{R}^{n \times N}$ Y matrix. Since this is a linear model, a set of weights W ($\mathbb{R}^{d \times N}$) is trained to map x_n to y_n or X to Y. To achieve a set of weights that encodes both sparsity and temporal smoothness. The following cost function is minimized during training.

$$\min_{W} \|XW - Y\|_F^2 + \lambda_1 \|W\|_1 + \lambda_2 \left\|RW^T\right\|_1 + \lambda_3 \|W\|_{2,1} \tag{14.1}$$

where $\|W\|_1$ is the L1-norm or lasso penalty that encodes for sparsity, $\|W\|_{2,1} = \sum_{i=1}^{d} \sqrt{\sum_{j=1}^{t} W_{ij}^2}$ is the group Lasso penalty that encodes for temporal grouping of features, $\left\|RW^T\right\|_1$ is the fused lasso penalty, $R = H^T$ and $H \in \mathbb{R}^{t \times (t-1)}$ where $H_{ij} = 1$ if $i = j$, $H_{ij} = -1$ if $i = j+1$, and $H_{ij} = 0$ otherwise that encodes for temporal smoothness.

Table 14.1: Results showing rMSE and R for M06 through M48 with and without mTBM features. (* $P < 10^{-3}$)

	without mTBM		with mTBM	
	rMSE	R	rMSE	R
M06	8.4452	0.6124*	6.5315	0.6499*
M12	8.2058	0.6989*	6.7600	0.6948*
M24	12.3285	0.6975*	6.7292	0.7704*
M36	10.4104	0.6225*	7.1673	0.7323*
M48	7.2023	0.6223	7.1232	0.6075

4 Multivariate Tensor-based Morphometry (mTBM) features

Previous work by Wang et al 2013[101] has provided a strong framework for extracting parametric surface-based features for sensitive detection of pathological changes across multiple subjects. In this study we apply this framework but on the hippocampal surface instead of the cortical surface.

5 Results

The results shown are from 2 simulation experiments where data from ADNI was used to to both train and test the cFSGL model. Experiment 1 used demographic information (Age and Gender), Freesurfer volumes and cortical thicknesses (326 features), the number of ApoE-$\epsilon - 4$ alleles as well as a baseline MMSE score as features used in the model. Experiment 2 added the mTBM features from each of the vertices of the hippocampus segmentation using Freesurfer. The vertex information from mTBM was scaled down by a factor 10 using bicubic interpolation to yield a total of 2100 features. 90 percent of the 624 subjects were used for training and the remaining 10 percent were used for testing. The results shown are from the 10 percent of our dataset allocated for testing. We calculated the root mean square error $\text{rMSE}(y, \hat{y}) = \sqrt{\frac{\|y-\hat{y}\|_2^2}{n}}$ as well as a the correlation coefficient between the pairs of predicted values and actual values at each of the time points.

Table 14.1 shows how predictive performance has improved by incorporating mTBM features into our dataset.

6 Discussion and Conclusion

Current results are from simple single iteration experiments. The performance of cFSGL is sensitive to model parameters and more work needs to be done in carefully choosing optimizing model parameters. However, this work goes to show that mTBM features has the potential to improve predictive power of cFSGL models especially for later time points.

Whether or not this approach provides more statistical power in disease progression research requires careful validation for each application. More importantly, we anticipate that the mTBM and multi-task learning framework may provide new insights on imaging biomarker and machine learning in medical imaging research. In the future, we plan to combine them for MCI or other types of disease progression studies. If our proposed combinational framework helps improve classification accuracy, it would then support the further use and development of mTBM measurements together with multi-task learning for predictive applications in the medical imaging field.

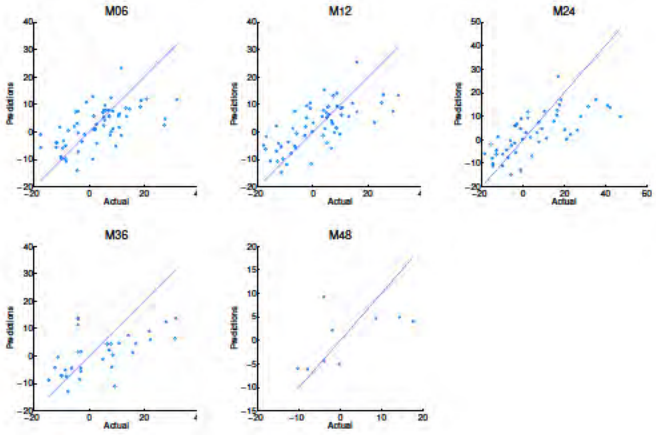

Figure 14.2: Results without mTBM Features - Scatter plots of Predictions versus Actual ADAS Cognition Scores at M06 through M48

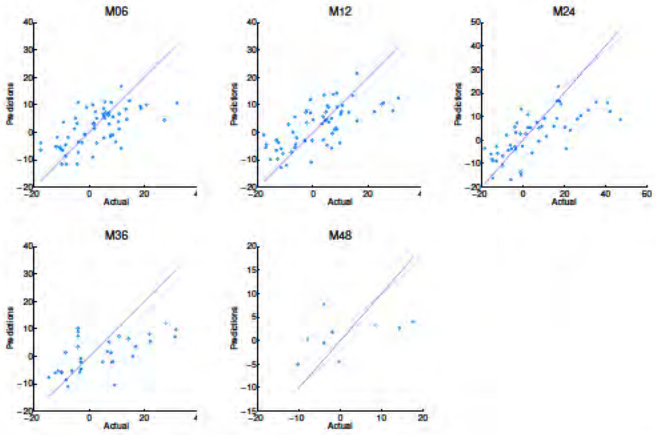

Figure 14.3: Results with mTBM Features - Scatter plots of Predictions versus Actual ADAS Cognition Scores at M06 through M48

Chapter 15

Mapping of ApoE4 Related White Matter Damage using Diffusion MRI

Sinchai Tsao[a,b] Darryl Hwa Hwang[a] Niharika Gajawelli[a,b] Stephen Kriger[c] Meng Law[a] Helena Chui[a] Michael Weiner[c] and Natasha Lepore[a,b]

[a] University of Southern California, Los Angeles, California, USA
[b]Children's Hospital Los Angeles, Los Angeles, California, USA
[c]Center for Neurodegenerative Disease, San Francisco VA Medical Center San Francisco, California, USA

Submitted SPIE Medical Imaging 2014

1 Abstract

ApoliopoproteinE $\epsilon 4$ (ApoE-$\epsilon 4$) polymorphism is the most well known genetic risk factor for developing Alzheimers Disease. The exact mechanism through which ApoE $\epsilon 4$ increases AD risk is not fully known, but may be related to decreased clearance and increased oligomerization of Aβ. By making measurements of white matter integrity via diffusion MR and correlating the metrics in a voxel-based statistical analysis with ApoE-$\epsilon 4$ genotype (whilst controlling for vascular risk factor, gender, cognitive status and age) we are able to identify changes in white matter associated with carrying an ApoE $\epsilon 4$ allele. We found potentially significant regions ($P_{uncorrected} < 0.05$) near the hippocampus and the posterior cingulum that were independent of voxels that correlated with age or clinical dementia rating (CDR) status suggesting that ApoE may affect cognitive decline via a pathway in dependent of normal aging and acute insults that can be measured by CDR and Framingham Coronary Risk Score (FCRS).

Keywords: DTI, Diffusion MRI, MRI, Alzheimer's Disease, Dementia, ApoE, Neuroimaging

2 Introduction

ApoliopoproteinE $\epsilon 4$ (ApoE $\epsilon 4$) polymorphism is the most well known genetic risk factor for developing Alzheimers Disease[109]. The exact mechanism through which $\epsilon 4$ increases AD risk is not fully known, but may be related to decreased clearance and increased oligomerization of Aβ. By making measurements of white matter integrity via diffusion MR and correlating the metrics in a Voxel-based Statistical Analysis with $\epsilon 4$ genotype

(whilst controlling for vascular risk factor, gender, cognitive status and age) we are able to identify changes in white matter associated with carrying an ApoE $\epsilon 4$ allele.

3 Methods

59 subjects with ages ranging from $70 - 86$ years were recruited from 3 different sites in a prospective longitudinal study of vascular contributions to aging and cognitive impairment, alone or in combination with AD. $\epsilon 4$ positive (29 subjects carrying at least one $\epsilon 4$ allele) and $\epsilon 4$ negative (30 subjects). Vascular risk was assessed using the 10 year Framingham Coronary Risk Score (FCRS) and the subjects were categorized either as high or low vascular risk. Dementia staging was performed using the Clinical Dementia Rating (CDR) system. MR imaging was performed on four>3T scanners. A rigorous image harmonization routine was performed to ensure all sequences produced comparable images from the different scanners. T1 weighted anatomical images (SPGR / MPRAGE) were used to coregister all the images to a common space using SPM's DARTEL Algorithm. b0 maps from the Diffusion images were registered to the T1 images using an affine transformation. Both the affine as well as non-affine transformations were concatenated to achieve coregistration for FA across all the subjects. Statistical Parametric Mapping was performed using SPM8. $\epsilon 4$ status, CDR scores, FRCS Category, Age as well as gender were used as covariates and factors in the Design Matrix.

4 Results

ApoE-$\epsilon 4$ related loss of FA was found most prominently in the parahippocampal regions (figure 15.1) and did not overlap with regions that correlated with Age and CDR (figure

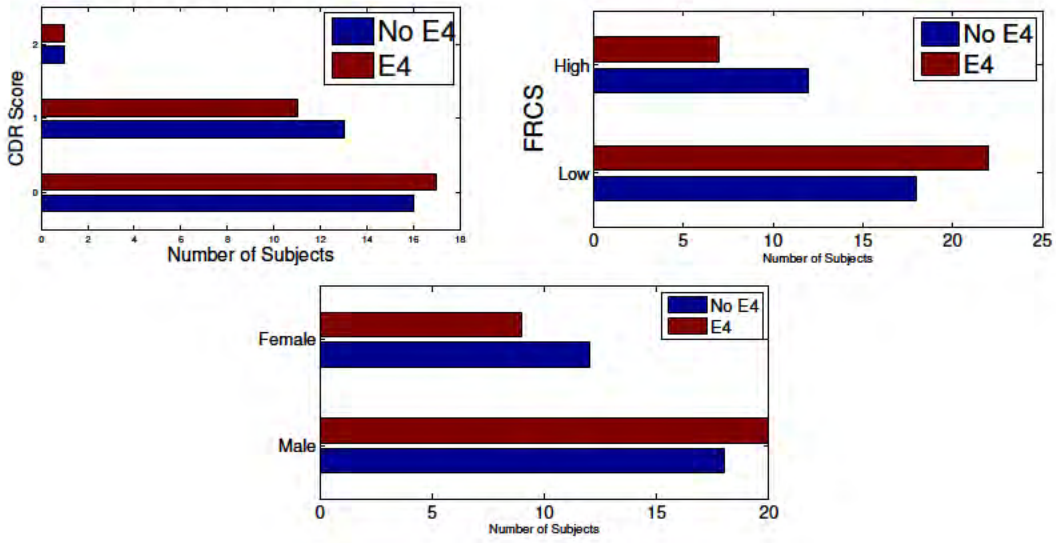

Figure 15.1: Demographic Distribution of the Subjects

15.3). CDR scores correlated most with the posterior fornix tracts (figure 15.3) in blue whereas the significant voxels for both ApoE-ϵ4 (red) as well as Age (green) resided more in the anterior regions surrounding the fornix and corpus collosum. A hemispheric asymmetry was observed with more age-related significant voxels on the left hemisphere, consistent with previous studies[109].

5 Conclusion

Our study shows promising results for separating the effects of ϵ4, Normal Aging and dementia severity when performing large scale MR imaging studies using Diffusion MR. Both the ApoE ϵ4 and CDR effects (parahippocampal gyrus and fornix) are integral components of the episodic memory system, which is highly vulnerable to neurofibrillary degeneration in AD. The involvement of the medial temporal diencephalic system in

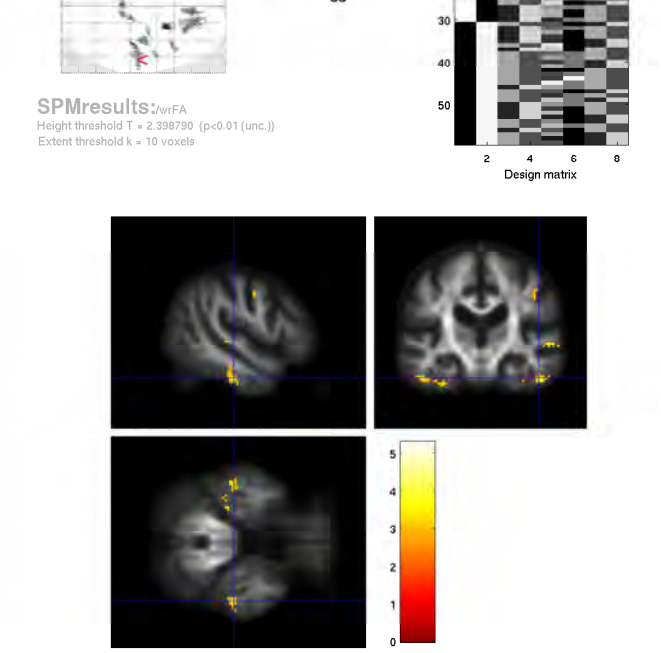

Figure 15.2: SPM of ParaHippocampal FA values with ApoE-ϵ4 < no ApoE-ϵ4 with $P_{uncorrected} < 0.01$ and extent threshold < 10 voxels (all other covariates were set as nuisance variables and controlled)

Vascular Cognitive Impairment is less prominent and more variable. Future work in analyzing the complete N>200 dataset will give us the statistical power to investigate the anatomical effects of vascular factors as well as differentiate the cognitive effects of WM damage by correlating individual ROIs with cognitive scores.

Acknowledgements

This work has been supported by USC ADRC's National Institutes of Aging Program Grant 5P01AG012435-18 as well as National Institute of Biomedical Imaging and Bioengineering grant 5R21EB013456-02.

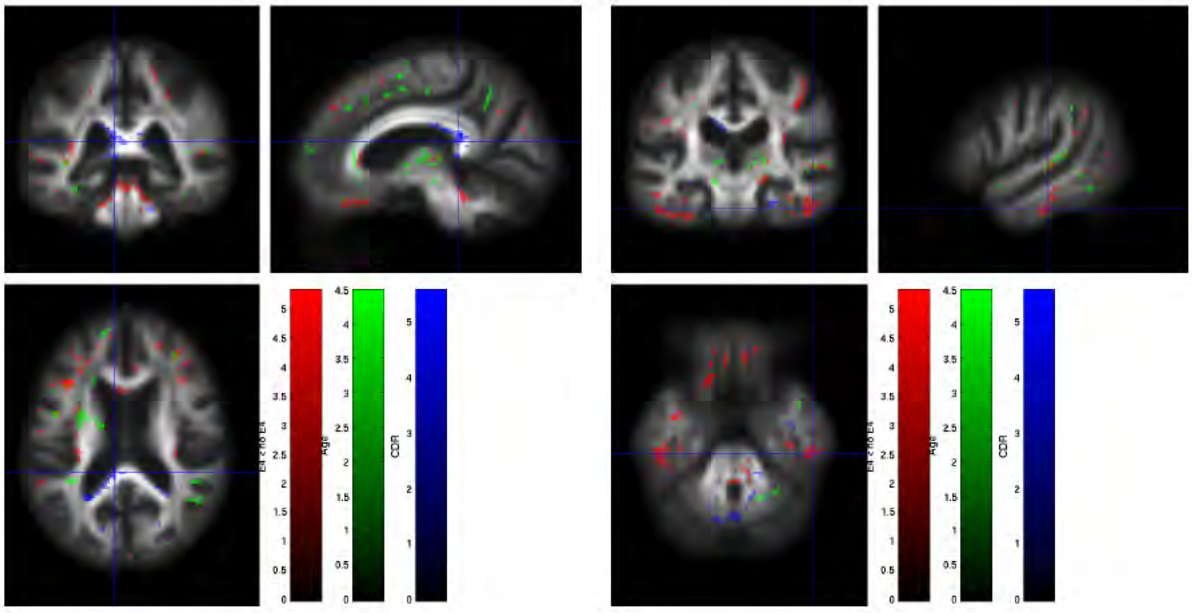

Figure 15.3: SPM of t-scores of the Posterior Cingulum (left) and Hippocampus (right) using FA values for ApoE$-\epsilon 4 <$ no ApoE$-\epsilon 4$ (Red), Age (Green) and CDR (Blue) with $P_{uncorrected} < 0.05$ and extent threshold < 20 voxels.

Chapter 16

Insulin sensitivity and brain reward activation in overweight Hispanic girls: a pilot study

Tanja C. Adam[1], Sinchai Tsao[2], Kathleen A. Page[3], Houchun Hu[4,5], Rebecca E. Hasson[6], Michael I. Goran[7]

[1] Department of Human Biology,
Maastricht University, 6200 MD Maastricht
[2] Department of Biomedical Engineering,
University of Southern California, Los Angeles, CA 90089
[3] Department of Endocrinology, Keck School of Medicine,
University of Southern California, Los Angeles, CA 90033
[4] Department of Radiology,
Childrens Hospital Los Angeles, Los Angeles, CA 90027
[5] Department of Electrical Engineering,
University of Southern California, Los Angeles, CA 90089
[6] Department of Family and Community Medicine,
University of California San Francisco, San Francisco, CA 94118
[7] Department of Preventive Medicine,
University of Southern California, Los Angeles, CA 90033

Submitted April 2013, Under Revision in **Pediatric Obesity**

1 Abstract

Context: The alarming prevalence of childhood obesity poses a significant health problem for the pediatric population and future generations. Insulin resistance is thought to be a link between obesity and the associated increased disease risk. In addition to its role as an energy regulatory signal to the hypothalamus, insulin acts to decrease food reward possibly through a direct alteration of dopaminergic signaling.

Aim: In the current study we examined the association of insulin sensitivity (SI) with cerebral activation in response to food and non-food cues.

Design: Twelve Hispanic girls (age: 8-11; BMI (kg/m2): 29.9 $\pm$ 5.7) participated in two study visits. The first visit included a frequently sampled intravenous glucose tolerance test. The second visit included a functional neuroimaging (fMRI) session (GE HDxt 3.0 Tesla)) with visual stimulation tasks. Blocks of images (high calorie (HC), low calorie (LC) and non-food (NF)) were presented in randomized order.

Results: For the comparison HC with NF, SI was inversely associated with activation in the anterior cingulate (r^2 = 0.65; p $<$ 0.005), the insula (r^2 = 0.69; p $<$ 0.005), the orbitofrontal cortex (r^2 = 0.74; p $<$ 0.005), and the frontal and rolandic operculum (r^2 = 0.76; p $<$ 0.001). Associations remained significant after adjustment for body adiposity. No differences in brain activation were observed comparing LC and NF. Conclusion: Peripheral insulin sensitivity is associated with cerebral activation in response to food cues. Insulin resistance may lead to overeating and the exacerbation of the development of obesity through over-activation of brain reward circuits.

Keywords: insulin sensitivity, pediatrics, brain reward, childhood obesity, functional imaging

2 Introduction

The alarming prevalence of childhood obesity is not only a significant health problem in the pediatric population, but poses a risk factor for adult morbidity and mortality as well (Must and Strauss 1999). One of the most common complications associated with obesity is type 2 diabetes caused in part by the effects of adiposity on insulin resistance (Boyko, Fujimoto et al. 2000). Insulin resistance is thought to be a link between obesity and the associated increased disease risk (Lee 2006). While body adiposity and insulin resistance are strongly associated in the adult population, the pediatric population of overweight and obese children still present with a wide variety of insulin sensitivity (Goran, Lane et al. 2008). Converging evidence shows that insulin as well as sensitivity to insulin is of major importance for homeostatic, but also for the hedonic, mesolimbic regulation of hunger and satiety (Figlewicz, Bennett et al. 2006). In addition to being an energy regulatory signal to the hypothalamus, insulin acts within the central nervous system (CNS) to decrease food reward possibly through a direct alteration of dopaminergic signaling (Figlewicz, Evans et al. 2003). In mouse cells with intact insulin reception, insulin was shown to increase the firing frequency of dopaminergic neurons in the ventral tegmental area (VTA), a prominent structure of the brain reward circuit (Konner, Hess et al. 2011). The effect was abolished, when insulin reception was inactivated. While CNS insulin production cannot be ruled out, converging evidence suggests that the majority of insulin enters the brain through active transport from the periphery (Banks 2004). It is therefore not surprising that manipulations of peripheral insulin concentrations were reflected in CNS insulin alterations (Schwartz, Sipols et al. 1990). One hypothesis referred to as the Central Resistance Model is that genetic or acquired resistance to adiposity-regulating

hormones occurs quite commonly and undermines the ability of those hormones to biologically protect against the development of obesity (Schwartz and Niswender 2004). In human research, the existence of brain insulin resistance along with peripheral insulin resistance was suggested after the observation of a reduction in insulin induced changes in the global cerebral metabolic rate for glucose in insulin resistant research participants compared to insulin sensitive participants (Anthony, Reed et al. 2006). Since insulin resistance is so closely intertwined with body fat, it has been difficult to tease apart the individual contribution of either one to alterations in brain reward activity. More detailed study designs comparing lean and obese individuals found specific associations of either body mass index (BMI) or insulin sensitivity with activity in food related resting state networks (Kullmann, Heni et al. 2012). Results show that, especially for reward related processing, insulin sensitivity might be of particular importance. Considering the range of insulin sensitivity despite obesity, children appear to be well suited for a more specific investigation of the individual contribution of insulin sensitivity and body adiposity to altered food related brain processing, specifically highly palatable foods. Central insulin resistance may contribute to altered food related reward perception even in the pediatric population (Adam, Toledo-Corral et al. 2009). An uninhibited, overactive reward circuit would then lead to overeating, setting children up for a chronic weight issue in the future. Purpose of the current study was to assess the importance of insulin sensitivity for brain reward activation in response to visual food cues in a pediatric population. It was hypothesized that lower insulin sensitivity in the periphery is associated with stronger activation of brain reward areas in response to high calorie food images compared to control images. The association was furthermore expected to be independent of body fat mass.

3 Methods

3.1 Participants

Twelve Hispanic, overweight girls were recruited through flyers and presentations at schools and boys and girls clubs in the greater Los Angeles area. Inclusion criteria for participants were female gender, Hispanic ethnicity, defined by all four grandparents being of Hispanic descent, Tanner stage 1 or 2, a body mass index above the 85th percentile for age and gender (Kuczmarski, Ogden et al. 2000) and right handedness. Participants were excluded from the study if they had diabetes, suffered from a major illness since birth, had a condition known to affect insulin sensitivity or had a neurological illness. Written informed consent was obtained from parents and youth assent from participants. The study was approved by the USC IRB committee.

3.2 Procedures

TAfter obtaining informed consent, participants came to the laboratory for two separate visits. The first visit included anthropometric and body composition measurements as well as an overnight stay in the USC Clinical trials unit, followed by a frequently sampled intravenous glucose tolerance test (FSIVGTT). The FSIVGTT took place at 8 am following a 10-h overnight fast. The second visit included a fMRI session with visual stimulation tasks. Visits were scheduled one week apart. All imaging sessions took place at 3pm with the participants being instructed to not eat anything after 12 noon.

3.3 Anthropometric measures

A pediatric health care provider conducted a medical history and physical examination and determined maturation using the criteria of Tanner (Tanner 1981). Height was measured to the nearest 0.1cm by a wall-mounted stadiometer and weight was recorded to the nearest 0.1kg by a balance beam medical scale. BMI and BMI percentiles for age and gender were determined based upon established CDC normative curves using EpiInfo 2000, Version 1.1 (Flegal, Ogden et al. 2004).

Table 16.1: Anthropometric measures describing mean ± standard error of the means (SE) and range (n = 10).

Table 1. Anthropometric measures

	Mean ± SE	Range
Age (years)	9.9 ± 1.1	8-11
Weight (kg)	59.3 ± 13.4	38.7 - 74.8
Height (cm)	144.06 ± 7.11	129.3 - 152.1
BMI (kg/m^2)	29.9 ± 5.7	23.3 - 36.8
Waist (cm)	87.7 ± 11.93	71 - 103
Hip (cm)	90.8 ± 8.1	82 - 101
Fat mass (kg)	24.21 ± 8.2	13.8 -34.5
Lean mass (kg)	33.2 ± 5.8	22.8 - 41.11

3.4 Body Composition

Body composition (total body fat and total lean mass) for all participants was determined with dual-energy x-ray absorptiometry (DXA) using a Hologic Discovery A model (82702, Hologic, Bedford, MA).

3.5 Measures of Insulin Sensitivity

All girls participated in a FSIVGTT, assessing insulin sensitivity (SI), the acute insulin response (AIR), and disposition index (DI). After a 12h fasting period intravenous catheters were placed in an anticubital vein of both arms. Two fasting blood samples (-15 and -5 minutes) were followed by a 0.3g/kg body weight intravenous (iv) glucose administration at timepoint 0. At 20 minutes, insulin (0.02 U/kg body weight, Humulin R; Eli Lilly, Indianapolis, IN) was administered iv. Blood samples were taken at 2, 4, 8, 19, 22, 30, 40, 50, 70, 100 and 180 minutes. SI, AIR and DI as an indicator for -cell capacity was calculated with MINMOD MILLENIUM 2003 (Bergman, Phillips et al. 1981). Blood samples from the FSIVGTT were centrifuged for 10 minutes at 2500rpm and plasma aliquots were frozen at -80 C until further analysis.

3.6 Analysis of blood parameters

Blood samples from the FSIVGTT were centrifuged and aliquots were stored at -80 C until further analyses. Blood for glucose analysis was collected in fluoride tubes and blood for insulin analysis was collected in lithium heparin tubes. Plasma was assayed in duplicate for glucose using the glucose oxidase method and a Yellow Springs Instrument 2700 analyzer (YSI Inc., Yellow Springs, OH). Insulin was assayed in duplicate using an ELISA kit from Linco (St. Charles, MO).

3.7 Food picture exposure paradigm

Design of the study was a block design consisting of two visual activation blocks and control blocks presented in randomized order. All images were chosen based on previous studies (Page, Seo et al. 2011) or through the International Affective Picture System

(Lang 1995). Activation task blocks consisted of 10 pictures of either high calorie (i.e. pizza, cheeseburger, candy) or low calorie food items (i.e. asparagus, broccoli, carrots). Before, between and after activation task blocks, control blocks of 10 non-food items were presented in randomized order (i.e. book, bus, bicycle). Compared to stimulation task items, control items were selected based on similarity in object complexity, as well as color, texture and shape variety. All visual stimuli were presented for 2.5 seconds with a 0.5 second inter-stimulus interval. Pictures were projected from a Macintosh computer onto a screen placed near the foot of the scanner, where they were viewed through a mirror mounted on the head coil. Participants were instructed to view the series of pictures with the intention to recall them after the scanning procedure.

3.8 Imaging and statistical analysis

MRI acquisition was conducted on a 3.0 Tesla scanner (GE HDxt) equipped with an eight-channel head coil. Foam padding and surgical tape were used to reduce motion of the subjects head. A functional echo-planar T2*(BOLD)-weighted sequence (TR: 3000 ms, TE: 25 ms, flip angle: 90°, FOV: 192 mm, matrix: 64×64, voxel size: $3.4375 \times 3.4375 \times 5mm$) was used to acquire 50 volumes during the visual stimulus presentation. A T1-weighted anatomical volume (TR: 500 ms, TE: 9.88 ms, flip angle: 90°, FOV: 192 mm, matrix: 256×256, voxel size: $0.8594 \times 0.8594 \times 5mm$) was also acquired at the same slice locations as the functional sequence to allow for functional-anatomical co-registration. Visual stimuli were presented by PsychToolbox for Matlab (Brainard 1997). The functional images were corrected for motion in SPM8 (Wellcome Trust Centre for Neuroimaging, London, UK) smoothed and co-registered to the standard Montreal Neurological Institute (MNI) template for comparison. Through the co-registration process images were sliced into 2

x 2 x 2 mm isotropic voxel space using sinc interpolation. A statistical parametric map was generated for each subject using the general linear model (GLM) with the stimulus as the primary parameter of the model. To eliminate activation due to movement, 6 movement parameters were also included in the model. A box-car waveform was used as the reference paradigm. For the statistical analysis, one participant was excluded due to the inability to participate in the IVGTT. Another participant was excluded due to too much head motion during the scanning process, leaving a total of 10 participants for the final analysis. Contrast images of each subject were used for group statistics calculated as random effects analysis at the second level, which takes variances between subjects into account. The statistical threshold used to report group activations was set at $p < 0.005$. All activated regions were identified by the Automated Anatomical Labelling software (Tzourio-Mazoyer, Landeau et al. 2002). Variables were tested for normality and log transformed if necessary. To assess the effect of SI and fasting insulin on brain activation in response to high calorie, low calorie and control images, conditions were contrasted in an ANCOVA using SI and fasting insulin as a covariate. Regression analysis was utilized to assess the association between brain activation, body adiposity, SI and fasting insulin concentrations. First, we computed Spatial Parametric Maps produced by either high or low calorie activation tasks versus the non-food control condition. In a next step we performed a 2nd level analysis by comparing maps produced by high and low calorie activation tasks. Regions of interest were established through their correlation with SI and fasting insulin ($p < 0.005$; uncorrected) and a cluster threshold of 10 voxels.

4 Results

Mean values (±SD) of anthropometric measures and range are described in Table 1. Three of the participating girls were in Tanner stage 1 and seven were in Tanner stage 2 at the time of study completion. All girls were of Hispanic descent (as defined by all four grandparents identifying as Hispanic) and overweight (body mass index above the 85th percentile for age and gender). Mean fasting glucose concentrations were 91.4± 9.5 mg/dl (ranging from 79−109.5 mg/dl). Three participants had impaired fasting glucose (IFG) according to the standards of the American Diabetes Association and therefore qualified as pre-diabetic (2000). Fasting insulin concentrations were on average 26.69 ± 19.6 μU/ml (ranging from 3.52−50.90 μU/ml).

4.1 Brain responses to visual stimulation and SI

Significant differences in BOLD activation in response to high calorie foods and non-food pictures (Table 2) were observed in the left caudate, left orbitofrontal cortex, the left insula, the frontal and rolandic operculum, and the left anterior cingulate. SI was inversely associated with activation in insula ($r^2 = 0.69$; $p < 0.005$, Figure 1A), orbitofrontal cortex ($r^2 = 0.74$; $p < 0.005$), anterior cingulate ($r^2 = 0.65$; $p < 0.005$, Figure 1B), frontal, and rolandic operculum ($r^2 = 0.76$; $p < 0.001$). When comparing high calorie food images with low calorie food images, significant differences in BOLD signal were observed for the putamen and the insula. More specifically, SI was negatively correlated with activation in putamen ($r^2 = 0.74$; $p < 0.005$, Figure 2A) and insula ($r^2 = 0.66$; $p < 0.005$, Figure 2B). Body adiposity was significantly associated with activation in all of the areas previously listed, but was not associated with SI ($p > 0.05$). In a next step body adiposity was

considered as a covariate in the regression analysis. With body adiposity as a covariate, SI stayed independently associated with activation in all areas listed above. No differences in brain activation were observed comparing low calorie food with non-food images.

4.2 Brain responses and fasting insulin

Significant differences in BOLD activation were observed comparing high calorie food images with non-food control images. Fasting insulin concentrations were related to activation in the caudate (($r^2 = 0.70$; $p < 0.005$; Figure 3A) and the insula ($r^2 = 0.69$; $p < 0.005$; Figure 3B). No differences in activation were observed in areas associated with reward comparing high calorie food images and low calorie food images, nor did we find differences comparing low calorie food images with non-food control images. Body fat was not associated with activation in caudate and insula comparing high calorie food images and non-food control images.

Table 16.2: Comparison of regional brain activation in response to high calorie food > non food stimuli in 10 overweight Hispanic girls.

Table 2. Increases in regional brain activity in response to high calorie pictures vs. control pictures

	Reference coordinates							
	x	y	z	kb	Hemisphere	Max z	Effect size	P < 0.005
Caudate	-20	22	16	10	L	3.27	1.03	0.002
Insula	-32	-24	22	12	L	3.12	0.98	0.002
Orbitofrontal cortex (OFC)	-48	24	-4	34	L	3.45	1.09	0.001
Insula	38	-32	6	82	R	3.15	0.99	0.001
Insula	-46	4	-6	37	L	3.02	0.95	0.002
Rolandic operculum	-56	10	4	17	L	3.18	1	0.001
Anterior Cingulate	-4	42	4	36	L	2.92	0.92	0.004

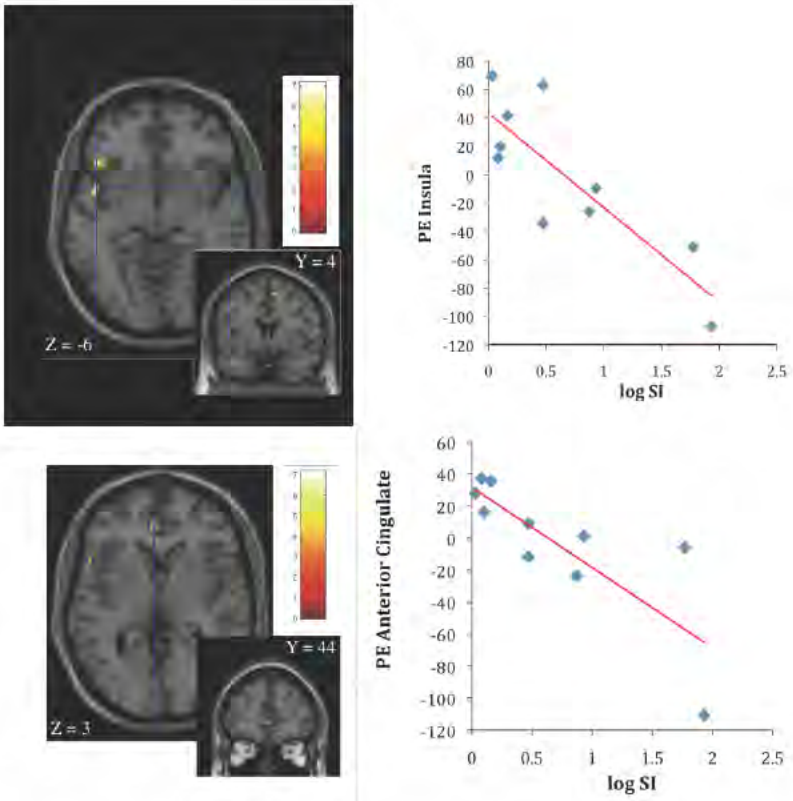

Figure 16.1: Association of insulin sensitivity (SI), insula activation (parameter estimates, PE) (Figure 1A (top): r2 = 0.69; p < 0.005) and left anterior cingulate activation (Figure 1B (bottom): $r^2 = 0.65$; p < 0.005), contrasting cerebral activation in response to high calorie visual stimuli > non-food visual stimuli.

5 Discussion

Results of the current study show that even in children peripheral insulin sensitivity appears to be associated with the cerebral response to food cues. Stronger cerebral activation was associated with lower insulin sensitivity and higher fasting insulin concentrations, particularly in brain areas associated with motivation and reward. Insulin sensitivity was also inversely associated with activation of gustatory (frontal operculum) and somatosensory (rolandic operculum) regions encoding food taste and texture. Our results lend support

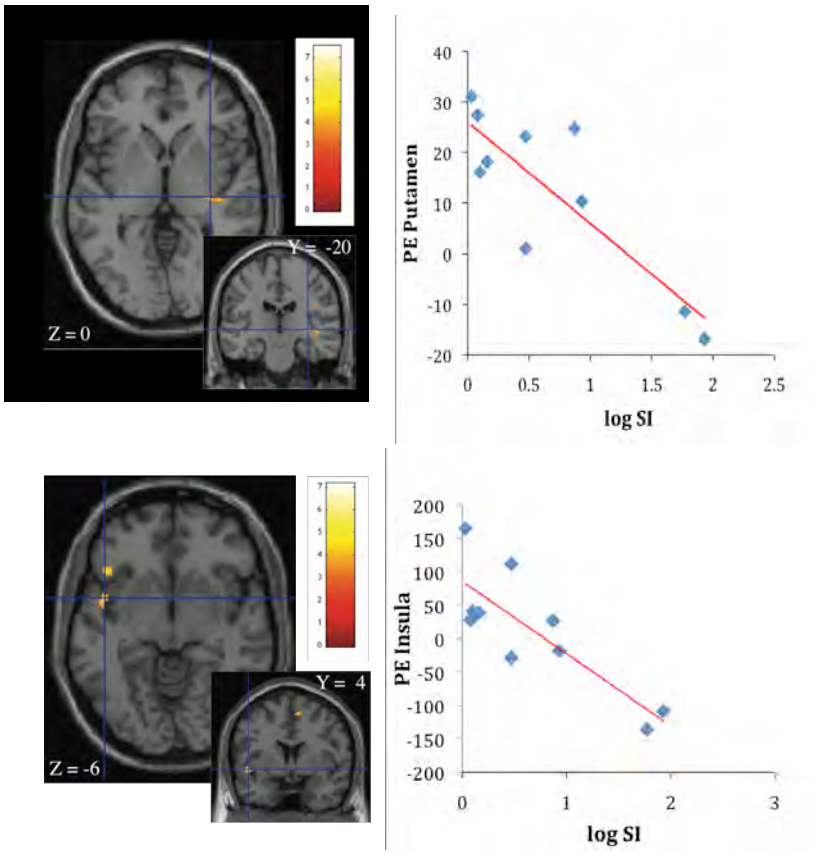

Figure 16.2: Association of Insulin Sensitivity, putamen activation (parameter estimates, PE) (Figure 2A: $r^2 = 0.74$; $p < 0.005$) and insula activation (Figure 2B: $r^2 = 0.66$; $p < 0.005$), contrasting cerebral activation in response to high calorie visual stimuli > low calorie visual stimuli.

to the idea of a co-occurrence of peripheral and central insulin resistance, which was previously suggested by other authors (Anthony, Reed et al. 2006). Insulin has been long known as an important signal for homeostatic food intake regulation. With the increasing utilization of brain imaging technology it became apparent, that the disruption of insulin signaling may play an important role for overeating and the development of obesity, i.e. through a disruption of insulin signaling in the brain reward circuit.

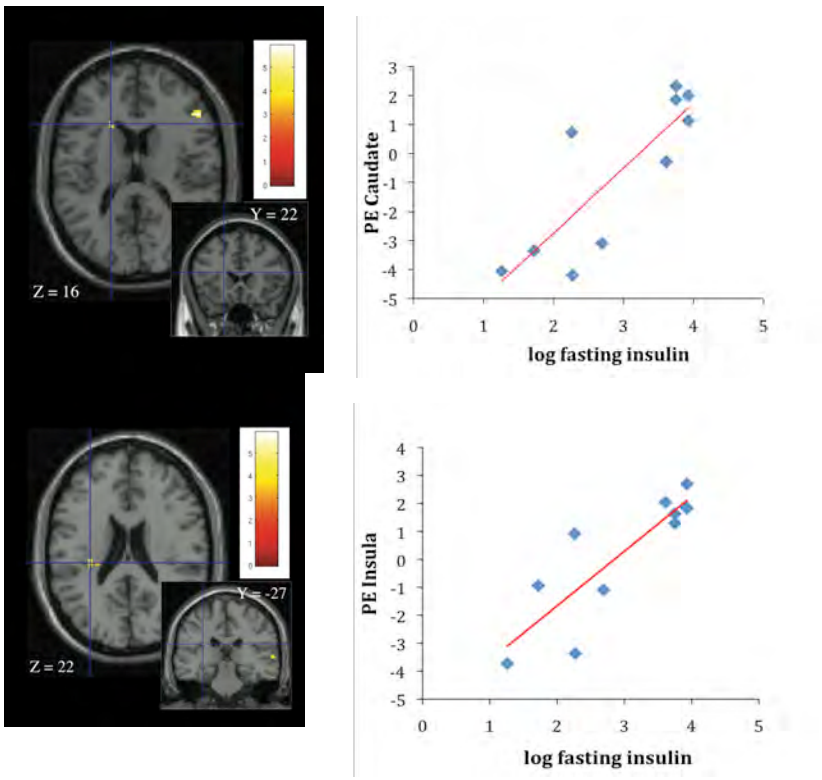

Figure 16.3: Association of fasting insulin concentrations, caudate activation (parameter estimates, PE) (Figure 3A: $r^2 = 0.70$; $p < 0.005$) and insula activation (Figure 3B: $r^2 = 0.69$; $p < 0.005$), contrasting cerebral activation in response to high calorie visual stimuli > non-food visual stimuli.

In rodent studies the intraventricular administration of insulin and leptin decreased sucrose self-administration, a task frequently utilized to measure food reward (Figlewicz, Bennett et al. 2006). After receiving a high fat diet for five weeks, the ability of both adiposity signals to decrease food reward was abolished, supporting the idea of central resistance to the same.

Strikingly, the high fat animals did not gain weight different than the chow-fed control rats, excluding weight as the responsible variable for the results.

It has been difficult in the past to tease apart whether associations between obesity and brain reward activity are due to obesity or are due to the insulin resistance accompanying obesity. Insulin sensitivity is strongly related to body weight and insulin resistance is often thought of as the linking factor between obesity and disease risk (Cruz, Shaibi et al. 2005). There are a few recent studies that support the idea of insulin sensitivity affecting the brain reward response to food cues, rather than obesity alone (Kullmann, Heni et al. 2012; Jastreboff, Sinha et al. 2013). Given the fact that children present with a wide range of insulin sensitivity despite obesity, a pediatric group of research participants seems to be an ideal group to investigate the importance of insulin sensitivity, obesity, or both for brain reward signaling.

Body adiposity was also positively related to activity in all of the listed areas of the brain. However, when statistically considering body adiposity in the relationship between insulin sensitivity and brain reward activity, we find the relationship to be independent of body adiposity.

It is an ongoing discussion if obesity is associated with increased or decreased activity in response to food cues and the question if obese individuals eat for compensation of reward deficiency or due to over-activity of reward signaling, remains unanswered.

Traditionally, insulin resistance has been approached as a consequence of obesity. Studies demonstrating the consequences of disrupted insulin signaling suggest however, that overeating and obesity might very well be a consequence of insulin resistance, forming a vicious cycle that becomes increasingly hard to break.

Body mass and body adiposity have been well investigated regarding their association with cerebral activity in response to food cues. However, reports on the direction of the

association have been controversial. While one group described a positive BMI dependent activation of regions associated with food reward comparing visual high calorie with neutral stimuli (Rothemund, Preuschhof et al. 2007), others find negative associations of BMI and brain reward area activation (Stice, Spoor et al. 2008). So far, controversial results often have been explained by the concept of sensitivity to reward, a personality trait that is strongly implicated in the risk for addiction and overeating (Davis, Strachan et al. 2004). Lower cerebral reward sensitivity may be an inherent predisposition prompting the individual for constant overstimulation in order to reach average stimulation levels. It may however also be a long-term consequence of overstimulation through an abundance of high calorie, highly palatable food, resulting in neuroadaptations, i.e. receptor downregulation. This hypothesis finds support in studies investigating dopamine, a major brain reward transmitter. Findings from animal studies suggest that midbrain dopamine neurons are direct targets of insulin and leptin, and that they participate in mediating the effects of these hormones on reward-seeking behavior (Figlewicz, Evans et al. 2003). Several studies demonstrated a lower availability of dopamine 2 receptor (D2) in striatal regions of obese research participants (Wang, Volkow et al. 2002) or polymorphisms associated with the D2 receptor gene (Stice, Spoor et al. 2008). In recent studies insulin was found to play an important role for dopaminergic signaling (Konner, Hess et al. 2011), possibly through protein kinase B (Speed, Saunders et al. 2011). Insulin receptors are widely distributed throughout the limbic brain. We were not able to measure dopamine activity in our research participants, but results from other studies suggest that differences in dopamine activity and reception may in part explain the results from the current study.

Functional imaging studies in children are often criticized due to the difficulties of children to not move during the scanning process. We only had to exclude one participant due to too much head movement. Other studies support that large scale fMRI studies are feasible in children as young as five years (Byars, Holland et al. 2002). Therefore, the advantage that young age offers for research regarding the cause and effect of health issues weighs out practical issues of the study execution. Research studies in adults show that abnormal neural responses to food cues persist in participants after weight loss and that successful dieters are characterized by a strong prefrontal activation in response to food cues (DelParigi, Chen et al. 2004; DelParigi, Chen et al. 2007; Bruce, Hancock et al. 2011). The prefrontal cortex is involved in self-control and behavioral monitoring, emotion regulation and salience attribution. In children, the implementation of inhibitory choices regarding food intake is in part dependent on the morphological and physiological development of the brain during childhood and adolescence (Gomez-Perez, Ostrosky-Solis et al. 2003) and a progressively greater focal activation in the prefrontal cortex during adolescent development has been observed regarding tasks that require inhibition of behavioral responses (Tamm, Menon et al. 2002). Results from our study suggest that chronic activation of the brain reward system may develop before the prefrontal cortex is developed enough to inhibit the detrimental behavior of overeating, establishing neurological patterns that predispose children for overweight and lifelong weight struggle. Our study shows the association of peripheral insulin sensitivity with cerebral activation in response to food cues independent of adiposity. The results therefore demonstrate the importance of treatment of insulin resistance in addition to weight loss as a measure to regulate neural responses to food cues to prevent excessive weight gain through overeating and obesity.

Chapter 17

Conclusion

1 Bone Age Assessment

In my earlier work on computer vision-based Bone Age Assessment (Chapter 12), I studied the development of the skeletal system as it progresses from infancy to adult. I used the qualitative and descriptive information from the Greulich and Pyle Atlas, Tanner and Whitehouse methods and translated it into extracting imaging features. In this case, the skeletal system was relative simple and features were based on either (1) the existence or non-existence of a particular bone (2) the size and shape of growing bones through development and lastly, (3) the appearance of the growth plate as it starts to fuse at the end of development. The contrast in this case was from X-ray so image intensity is related to bone density but most of the image processing was performed on binary images. The conclusion from this work was that the Radius bone did provide some improvement in detecting age changes at later age ranges. However, it is not sufficient since the system still under performs at the later age ranges. Possible solutions include (1) Adding the Ulna as another bone of interest and (2) Use the overall size of all the bones as a feature to measure bone growth.

2 Obesity

The next system we probed was the interaction between the nervous system and the endocrine system and how that affects obesity. The hypothesis was that with obese individuals their body does not give enough positive feedback when stimulated with low calorie foods. This feedback is believed to be attenuated by the endocrine system. The exact mechanism of attenuation is not known but believed to be related to insulin and blood sugar levels.

In our initial work with Tanja Adam PhD, we designed a fMRI experiment that presented visual stimulus in the form of low calorie and high calorie foods and applied fMRI tools to the neurobiological problem of Obesity. We measured how well the T2* BOLD signal correlated in time with the presentation paradigm convolved with the hemodynamic response function.

The project with Kathleen Page MD showed more understanding of how this could influence or how the reward pathways could influence functional connectivity. Furthermore, this experiment allowed us to probe whether gut response could be different from a visual response. With functional connectivity we are at the forefront of looking at down-regulation instead of up-regulation and looking at overall connectivity instead of correlation with a visual paradigm which gives us an new viewpoint / dimension of brain function.

We then looked at how well our fMRI experiment with visual stimulus correlated with endocrinological factors such as insulin resistance. We found that insulin as neurotransmitter in the endocrine system could have a downstream effect of how the reward pathway reacts to low and high calorie foods.

3 Aging and Dementias

We then turn our attention to white matter damage and dementia. This project was particular challenging because there are no standard methods for characterizing neuronal damage in vivo. The main methods of imaging white matter damage has been White Matter Hyperintensities (WMHs) using FLAIR MRI. White matter is particular difficult because of the structured nature of the fiber bundles and neurons. Histology of White Matter post-mortem has driven how we look at in vivo ways of imaging white matter. The histological understanding, together with our understanding of aging allows us to postulate what may be contaminating our white matter diffusion signal.

In our CSF contamination chapter, we were able to design a contamination correction technique based on the biological phenomenon of brain atrophy where CSF partial volume increases as the brain tissue atrophies.

Similar to the idea with insulin modulating the reward system, we postulated that a genetic factor could be modulating white matter damage. Using a similar framework but with the diffusion MRI metric instead of the fMRI statistical parametric map, we correlated each voxel with the subject's genetic factor status- in this case, we looked at whether the subject is a (1) non-carrier (2) homozygote or (3) heterozygote of the ApoE-ϵ4 gene. This allowed us to ask whether this genetic factor modulates white matter decline. In this case we assumed that the process can be approximately linear since we are using the general linear model but the modulation could very well be non-linear and an extension of this work could be to try to model this interaction non-linearly.

For voxel-wise methods, detection becomes very computationally intensive since we are correlating each voxel with each of the co-factors. To make the problem computationally

viable we mainly assumed linearity in modulation of voxel values by other factors such as insulin or genetics, but we believe this a reasonable assumption since our domain knowledge of most biological systems informs us that tissue metrics measured via imaging tend to have monotonic modulation functions. For example, the deterioration of FA values should be approximately linearly modulated by the genetic factor ApoE.

With features from the bone age assessment work, we have much lower dimensionality since we are not doing voxelwise analysis, therefore we were able to use higher order classification / correlation models such as fuzzy logic. I believe that this may be also possible with some of the voxelwise MRI work if we are able to do some reasonable dimension reduction using domain knowledge. However, I also believe that most changes are dictated by monotonic modulation functions and therefore can be detected by linear models. Moreover, even if you use higher order methods for high dimensional feature spaces, the fit is only as good as the quality of the feature space and high order methods do not substitute for better SNR or better domain knowledge-based definition of the feature space.

4 Generating Meaningful Imaging Contrast

Throughout this thesis we've been designing metrics or image contrasts that correlates well with either brain function or some pathological state in the tissue. In the imaging of obesity, we assume that the T2* Blood Oxygen Level Dependent (BOLD) activity is correlated with brain activity but we know that there are vascular effects that could displace the signal away from the exact location of brain activity. However, with this type of study it is reasonable just to deconvolve the Hemodynamic Response Function (HRF)

which is essentially the point spread function of the BOLD effect. We then correlate the deconvolved T2* BOLD time sequence with the time sequence of the presentation paradigm.

If we assume that the HRF is uniform across the entire brain, we can then do the analysis without deconvolving the hemodynamic response function and do voxelwise correlations to look at functional connectivity. There still needs to be work done on correlation due to vascular changes and how this affects brain connectivity. Obviously vascular changes are part of the response to brain activity and whether that is something that we consider actual brain activity. The actual brain activity that we want to detect is action potentials going the neuron causing the release of neurotransmitters. However the surrogate event is the vascular response to the need for more energy as modeled by the HRF that is measured by the T2* BOLD signal. The question is how well this surrogate event correlates with actual action potential based brain activity. There could be global vascular effects that can cause this assumption to be violated. Moreover, local vascular effects due to differences in "plumbing" could also detect differences that are not due to brain activity. The connectivity to seem connected as seen by correlation but may be purely due to vascular effect.

An extension to the fMRI BOLD experiment, especially relating to the high and low calorie foods, another novel contrast would be the correlation or the second level correlation of the t-scores from the T2* BOLD signal's correlation with the presentation paradigm. The correlation of the correlation would then be the second level analysis, where these t scores are correlated with a subject's amount of insulin sensitivity. This ties back to the first goal of using demonstrating how domain knowledge can be used to build hypothesis. Our understanding of how the brain works tell us that the difference

of BOLD signal correlation with the presentation of low calorie foods versus with high calorie foods could be modulated by insulin sensitivity and we could then use this two level statistical approach to detect this difference.

Moving on to white matter imaging contrast with diffusion MRI, once again our understanding of the domain knowledge allowed us to definite what meaningful contrast in this case means. We realized that meaningful contrast in the context of white matter imaging is the an accurate measurement of the actual fibers. Certainly, the amount of CSF partial volume may be correlated with how much white matter atrophy exists at a single voxel. These atrophic effects tend to be non-focal and widespread in the brain. However, what we really need in our FA maps are measurements without the CSF signal. The atrophic effects of the brain are much better measured by morphometric methods, which looks at are how much the brain deforms as it ages. Although we haven't looked at CSF partial volume as a measure of brain atrophy because we aren't able to accurately measure the CSF partial volume accurately yet. Certainly, the changes based on CSF partial volume as measured by DTI are not useful because they are non-focal. Therefore the DTI signal without CSF partial volume should give us more interesting information about the more focal white matter damage. This extends to our voxelwise analysis with the genetic factor ApoE4 which mirrors our second level fMRI analysis with insulin sensitivity, where we would like to look for focal changes and not these brain wide effects.

This general model framework also allows us to look at multiple covariates and not only ApoE4. With our poster in ISMRM we showed that we can separate voxelwise correlations of white matter tissue measures such as FA with multiple covariates such as ApoE4 and Age, giving us the possibility of separating the effects of each of these covariates on white matter deterioration.

5 Pattern Detection

Last but not least we evaluate our goal of designing computation techniques for pattern detection. With the bone age assessment, we applied a number of machine learning techniques to the bone age assessment system. We applied ANN techniques but we found that the fuzzy logic system was quite adequate in weighting the different features to give an accurate prediction of bone age. However, we did evaluate applying Support Vector Machine (SVM) on highly non-linear feature spaces and may be worth trying since it is quite robust. But the common theme here is that the computation technique is as good as the feature space and the feature space has to very robust and finely tuned for the pattern that you are looking for. In the case of bone age assessment, we found that the improvements in prediction power either ANN or fuzzy logic was comparable and there is simply not enough information in the radius bone to accurate predict the last couple of years of development. Therefore beyond better computation techniques we need more information in our feature space.

There has also been attempts at using Massive Artificial Neural Network using a whole image as an input with many hidden layers. Not only is training such massive artificial neural network (MANN) difficult, and computationally inefficient but the results often run into problems with over fitting (citation). The bone age assessment project was a good first step at applying computational techniques for pattern detection in medical imaging since we have both the pediatric radiologist's reading of the bone age as well as the normal subject's chronological age as targets. The advantage of the computation technique in this case is also much obvious since the computer vision is known to be more

consistent than inter-reader variation. Moreover, computer vision does not suffer from fatigue that a human reader would.

We were also able to apply the general linear model to both the obesity imaging fMRI work as well as the diffusion MRI white matter imaging work to investigate how non-imaging factors modulate the imaging measures. The main computational technique capstone project was the application of convex fused sparse group lasso in predicting disease progression. Although the technique was developed by our collaborating at Arizona State University, our understanding of domain knowledge (in this case dementia) definitely allows us to have a better idea of how to fine tune the system for maximum performance. Moreover, it is interesting to look at how the lasso portion of the algorithm behaves in dimension reduction in this high dimensional features space.

6 Future Work

The RadSearch project is not yet fully complete. We have not explored how the system can be implemented whilst being HIPAA compliant.

The Obesity Neuroimaging work unfortunately is no longer on-going at USC. I still believe that it is extremely interesting to look at the differences between gut-based stimulus response and taste-based stimulus response. I believe the gut, which is an often neglected part of the nervous system, may hold the keys to understanding obesity and our perception of food-based stimuli. This becomes even more compelling, especially, when you look at development and how the gut develops by separating from the brain stem. Furthermore, the interaction between the gut and the brain is not well known and it would be interesting to develop fMRI / EEG techniques that could sensitive to activity in

that part of the nervous system. With the on-going obesity epidemic, the idea of obesity as a pathology has been more accepted and more work needs to be done on finding the origins of this pathology. This is predicated on seeing how the brain reacts differently to different stimulus based on different obesity statuses. I believe that information will help support the increasingly accepted view that obesity is not just a lack of motivation but a pathology of the reward pathways and thus has a lot of socioeconomic and public health implications. Endocrine-Nervous interactions are also of interest, especially in clarifying the causal relationship between insulin sensitivity developed and reward pathway changes.

With the diffusion MRI work, our lab's ICA has the potential of changing what white matter DTI information can be acquired during a routine clinical scan. Moreover, promising model-based reconstruction techniques using a dictionary techniques as well as work with higher order might be necessary to understanding what is going on. Moreover, metrics that are more than tensor-based metrics such as FA and MD may also be helpful. However, whatever new metrics are developed should maintain the advantages of the tensor model; The model should be orientation invariant and scanner agnostic.

Moreover, I would still like to model the diffusion signal as Wide Sense Stationary signal (WSS) and leverage the pool of probabilistic signal processing techniques to model the diffusion signal. Moreover, Van Wedeem's work at getting gold standard high angular resolution scans of the brain might allow us to build better model-based diffusion MRI methods.

I am also still interested in looking at functional Diffusion MRI. During my PhD we tried for 6 months to use the diffusion MRI signal as the surrogate signal for neuronal activity. Our work suggests that this might be possible although better signal processing

techniques are still needed to determine a robust point spread function relationship between the diffusion effect and neuronal activity. Moreover, I don't believe that we have fully fine tuned the diffusion MR pulse sequence to look at the diffusion time resolution necessary for signal changes from neural activity. I also believe that although high b-value (greater than 4000) diffusion scans have very low SNR, a lot of interesting information exists in measuring small diffusion distances. Moreover, we are not unfamiliar with this low SNR environment and is not unlike the SNR of T2* BOLD images. Furthermore, I believe that the diffusion MRI image reconstruction engine from our MRI scanners may have filtered out some of the meaningful signal when bringing the signal from the frequency to the spatial domain. Therefore, I believe that analysis using the raw k-space data may yield better results.

With the machine learning / computational technique works, we have yet to see any techniques in the clinical space suggests that more work done is necessary in translating these techniques into the clinic. It is telling that the bone age assessment system has not been applied even though we have a very low dimension feature space in this case.

References

[1] N. Tzourio-Mazoyer, "Automated anatomical labeling of activations in spm using a macroscopic anatomical parcellation of the mni mri single-subject brain," *NeuroImage*, vol. 15, no. 1, pp. 273–289, 2002.

[2] D. L. Sackett, "Evidence-based medicine," in *Seminars in perinatology*, vol. 21, pp. 3–5, Elsevier, 1997.

[3] V. Yaghmai, S. Kuppuswami, J. W. Berlin, and S. A. Salehi, "Evaluation of personal digital assistants as an interpretation medium for computed tomography of patients with intracranial injury," *Emergency Radiology*, vol. 10, no. 2, pp. 87–89, 2003.

[4] D.-K. Kim, S. K. Yoo, and S. H. Kim, "Instant wireless transmission of radiological images using a personal digital assistant phone for emergency teleconsultation," *Journal of telemedicine and telecare*, vol. 11, no. suppl 2, pp. 58–61, 2005.

[5] W. M. Tellis and K. P. Andriole, "Integrating multiple clinical information systems using the java message service framework to enable the delivery of urgent exam results at the point of care," *Journal of Digital Imaging*, vol. 18, no. 4, pp. 316–325, 2005.

[6] B. Raman, R. Raman, L. Raman, and C. F. Beaulieu, "Radiology on handheld devices: Image display, manipulation, and pacs integration issues1," *Radiographics*, vol. 24, no. 1, pp. 299–310, 2004.

[7] U. Tachinardi, M. de Sa Rebelo, P. de Magalhaes Oliveira Jr, and P. Pilon, "Real time information from bedside monitors as part of a web-based patient record.," in *Proceedings of the AMIA Symposium*, p. 691, American Medical Informatics Association, 2001.

[8] B. J. Liu, L. Documet, J. Documet, H. Huang, and J. Muldoon, "Wireless remote control clinical image workflow: utilizing a pda for offsite distribution," in *Medical Imaging 2004*, pp. 178–184, International Society for Optics and Photonics, 2004.

[9] J. Documet, B. J. Liu, L. Documet, and H. Huang, "Wireless remote control of clinical image workflow: using a pda for off-site distribution and disaster recovery," *Journal of the American College of Radiology*, vol. 3, no. 7, pp. 520–527, 2006.

[10] J. Documet, R. Shretha, K. Wang, and L. B.J., "A vendor agnostic real-time patient dashboard to monitor patient workflow in a radiology department.," in *Presented at Radiological Society of North America's Annual Meeting*, 2007.

[11] A. Pyrros, P. Nikolaidis, V. Yaghmai, S. Zivin, J. I. Tracy, and A. Flanders, "A bayesian approach for the categorization of radiology reports," *Academic radiology*, vol. 14, no. 4, pp. 426–430, 2007.

[12] C. Friedman, P. O. Alderson, J. H. Austin, J. J. Cimino, and S. B. Johnson, "A general natural-language text processor for clinical radiology," *Journal of the American Medical Informatics Association*, vol. 1, no. 2, pp. 161–174, 1994.

[13] Y. Huang and H. J. Lowe, "A grammar-based classification of negations in clinical radiology reports," in *AMIA Annual Symposium Proceedings*, vol. 2005, p. 988, American Medical Informatics Association, 2005.

[14] Y. Huang and H. J. Lowe, "A novel hybrid approach to automated negation detection in clinical radiology reports," *Journal of the American Medical Informatics Association*, vol. 14, no. 3, pp. 304–311, 2007.

[15] B. Desjardins and R. C. Hamilton, "A practical approach for inexpensive searches of radiology report databases," *Acad Radiol*, vol. 14, pp. 749–56, Jun 2007.

[16] V. Bashyam and R. K. Taira, "A study of lexical behavior of sentences in chest radiology reports," in *AMIA Annual Symposium Proceedings*, vol. 2005, p. 891, American Medical Informatics Association, 2005.

[17] P. Szolovits, "Adding a medical lexicon to an english parser," in *AMIA Annual Symposium Proceedings*, vol. 2003, p. 639, American Medical Informatics Association, 2003.

[18] C.-H. Hsiao, T.-C. Hsu, J. N. Chang, S. J. Yang, S.-T. Young, and W. C. Chu, "Developing a medical image content repository for e-learning," *Journal of Digital Imaging*, vol. 19, no. 3, pp. 207–215, 2006.

[19] R. Jakobovits, J. F. Brinkley, C. Rosse, and E. Weinberger, "Enabling clinicians, researchers, and educators to build custom web-based biomedical information systems.," in *Proceedings of the AMIA Symposium*, p. 279, American Medical Informatics Association, 2001.

[20] W. Ceusters, P. Spyns, and G. De Moor, "From natural language to formal language: when multitale meets galen," *Studies in health technology and informatics*, pp. 396–400, 1997.

[21] W. Ceusters, P. Spyns, and G. De Moor, "From syntactic-semantic tagging to knowledge discovery in medical texts," *International journal of medical informatics*, vol. 52, no. 1, pp. 149–157, 1998.

[22] C. E. Kahn and C. Thao, "Goldminer: a radiology image search engine," *American Journal of Roentgenology*, vol. 188, no. 6, pp. 1475–1478, 2007.

[23] Y. Huang, H. J. Lowe, D. Klein, and R. J. Cucina, "Improved identification of noun phrases in clinical radiology reports using a high-performance statistical natural language parser augmented with the umls specialist lexicon," *Journal of the American Medical Informatics Association*, vol. 12, no. 3, pp. 275–285, 2005.

[24] V. Bashyam and R. K. Taira, "Indexing anatomical phrases in neuro-radiology reports to the umls 2005aa," in *AMIA Annual Symposium Proceedings*, vol. 2005, p. 26, American Medical Informatics Association, 2005.

[25] P. Spyns, N. T. Nhàn, E. Baert, N. Sager, and G. De Moor, "Medical language processing applied to extract clinical information from dutch medical documents.," *Studies in health technology and informatics*, vol. 52, p. 685, 1998.

[26] P. Spyns, "Natural language processing," *Methods of information in medicine*, vol. 35, no. 4, pp. 285–301, 1996.

[27] B. I. Reiner, N. Knight, and E. L. Siegel, "Radiology reporting, past, present, and future: the radiologist's perspective," *Journal of the American College of Radiology*, vol. 4, no. 5, pp. 313–319, 2007.

[28] P. S. Cho, R. K. Taira, and H. Kangarloo, "Syntactic parsing of medical reports using evolutionary optimization," in *AMIA Annual Symposium Proceedings*, vol. 2005, p. 920, American Medical Informatics Association, 2005.

[29] G. Hripcsak, C. Friedman, P. O. Alderson, W. DuMouchel, S. B. Johnson, and P. D. Clayton, "Unlocking clinical data from narrative reports: a study of natural language processing," *Annals of internal medicine*, vol. 122, no. 9, pp. 681–688, 1995.

[30] G. Hripcsak, J. H. Austin, P. O. Alderson, and C. Friedman, "Use of natural language processing to translate clinical information from a database of 889,921 chest radiographic reports1," *Radiology*, vol. 224, no. 1, pp. 157–163, 2002.

[31] P. J. Kenny, "Reward mechanisms in obesity: new insights and future directions," *Neuron*, vol. 69, pp. 664–79, Feb 2011.

[32] K. Stanek, J. Smith, and J. Gunstad, "Structural and functional neuroimaging in obesity," *Brain Imaging in Behavioral Medicine and Clinical Neuroscience*, pp. 193–200, 2011.

[33] E. Stice, S. Spoor, C. Bohon, and D. M. Small, "Relation between obesity and blunted striatal response to food is moderated by taqia a1 allele," *Science*, vol. 322, pp. 449–52, Oct 2008.

[34] E. Stice, S. Yokum, and K. Burger, "Youth at risk for obesity show greater activation of striatal and somatosensory regions to food," *The Journal of Neuroscience*, 2011.

[35] G.-J. Wang, N. D. Volkow, and J. S. Fowler, "The role of dopamine in motivation for food in humans: implications for obesity," *Expert Opin Ther Targets*, vol. 6, pp. 601–9, Oct 2002.

[36] W. D. S. Killgore and D. A. Yurgelun-Todd, "Body mass predicts orbitofrontal activity during visual presentations of high-calorie foods," *NeuroReport*, vol. 16, pp. 859–863, May 2005.

[37] W. D. Killgore and D. A. Yurgelun-Todd, "Affect modulates appetite-related brain activity to images of food," *International Journal of Eating Disorders*, vol. 39, pp. 357–363, July 2006.

[38] W. D. S. Killgore and D. A. Yurgelun-Todd, "Positive affect modulates activity in the visual cortex to images of high calorie foods," *Int J Neurosci*, vol. 117, pp. 643–53, May 2007.

[39] W. A. Marshall and J. M. Tanner, "Variations in pattern of pubertal changes in girls," *Arch Dis Child*, vol. 44, pp. 291–303, Jun 1969.

[40] D. H. Brainard, "The psychophysics toolbox," *Spat Vis*, vol. 10, no. 4, pp. 433–6, 1997.

[41] W. D. S. Killgore, A. D. Young, L. A. Femia, P. Bogorodzki, J. Rogowska, and D. A. Yurgelun-Todd, "Cortical and limbic activation during viewing of high- versus low-calorie foods," *Neuroimage*, vol. 19, pp. 1381–94, Aug 2003.

[42] T. C. Adam, C. Toledo-Corral, C. J. Lane, M. J. Weigensberg, D. Spruijt-Metz, J. N. Davies, and M. I. Goran, "Insulin sensitivity as an independent predictor of fat mass gain in hispanic adolescents," *Diabetes Care*, vol. 32, pp. 2114–5, Nov 2009.

[43] T. C. Adam, R. E. Hasson, E. E. Ventura, C. Toledo-Corral, K.-A. Le, S. Mahurkar, C. J. Lane, M. J. Weigensberg, and M. I. Goran, "Cortisol is negatively associated with insulin sensitivity in overweight latino youth," *J Clin Endocrinol Metab*, vol. 95, pp. 4729–35, Oct 2010.

[44] T. C. Adam, R. E. Hasson, C. J. Lane, J. N. Davis, M. J. Weigensberg, D. Spruijt-Metz, and M. I. Goran, "Fasting indicators of insulin sensitivity: effects of ethnicity and pubertal status," *Diabetes Care*, vol. 34, pp. 994–9, Apr 2011.

[45] B. Bennett, D. E. Larson-Meyer, E. Ravussin, J. Volaufova, A. Soros, W. T. Cefalu, S. Chalew, S. Gordon, S. R. Smith, B. R. Newcomer, M. Goran, and M. Sothern, "Impaired insulin sensitivity and elevated ectopic fat in healthy obese vs. nonobese prepubertal children," *Obesity (Silver Spring)*, vol. 20, pp. 371–5, Feb 2012.

[46] P. A. M. Smeets, C. de Graaf, A. Stafleu, M. J. P. van Osch, and J. van der Grond, "Functional mri of human hypothalamic responses following glucose ingestion," *Neuroimage*, vol. 24, pp. 363–8, Jan 2005.

[47] P. A. M. Smeets, S. Vidarsdottir, C. de Graaf, A. Stafleu, M. J. P. van Osch, M. A. Viergever, H. Pijl, and J. van der Grond, "Oral glucose intake inhibits hypothalamic neuronal activity more effectively than glucose infusion," *Am J Physiol Endocrinol Metab*, vol. 293, pp. E754–8, Sep 2007.

[48] S. Vidarsdottir, P. A. M. Smeets, D. L. Eichelsheim, M. J. P. van Osch, M. A. Viergever, J. A. Romijn, J. van der Grond, and H. Pijl, "Glucose ingestion fails to inhibit hypothalamic neuronal activity in patients with type 2 diabetes," *Diabetes*, vol. 56, pp. 2547–50, Oct 2007.

[49] Y. Liu, J. H. Gao, H. L. Liu, and P. T. Fox, "The temporal response of the brain after eating revealed by functional mri," *Nature*, vol. 405, pp. 1058–62, Jun 2000.

[50] G. Musen, D. C. Simonson, N. R. Bolo, A. Driscoll, K. Weinger, A. Raji, J. Théberge, P. F. Renshaw, and A. M. Jacobson, "Regional brain activation during hypoglycemia in type 1 diabetes," *J Clin Endocrinol Metab*, vol. 93, pp. 1450–7, Apr 2008.

[51] C. J. Holmes, R. Hoge, L. Collins, R. Woods, A. W. Toga, and A. C. Evans, "Enhancement of mr images using registration for signal averaging," *J Comput Assist Tomogr*, vol. 22, no. 2, pp. 324–33, 1998.

[52] J. L. Lancaster, L. H. Rainey, J. L. Summerlin, C. S. Freitas, P. T. Fox, A. C. Evans, A. W. Toga, and J. C. Mazziotta, "Automated labeling of the human brain: a preliminary report on the development and evaluation of a forward-transform method," *Hum Brain Mapp*, vol. 5, no. 4, pp. 238–42, 1997.

[53] J. L. Lancaster, M. G. Woldorff, L. M. Parsons, M. Liotti, C. S. Freitas, L. Rainey, P. V. Kochunov, D. Nickerson, S. A. Mikiten, and P. T. Fox, "Automated talairach atlas labels for functional brain mapping," *Hum Brain Mapp*, vol. 10, pp. 120–31, Jul 2000.

[54] S. Tsao, T. C. Adam, M. I. Goran, and M. Singh, "Application of fmri to obesity research: differences in reward pathway activation measured with fmri bold during visual presentation of high and low caloric foods," in *Proceedings of SPIE Medical Imaging, San Diego, CA*, 2012.

[55] A. Z. Snyder and M. E. Raichle, "A brief history of the resting state: The washington university perspective," *Neuroimage*, Jan 2012.

[56] S. Vidarsdottir, P. Vlug, F. Roelfsema, M. Frölich, and H. Pijl, "Orally disintegrating and oral standard olanzapine tablets similarly elevate the homeostasis model

assessment of insulin resistance index and plasma triglyceride levels in 12 healthy men: a randomized crossover study," *J Clin Psychiatry*, vol. 71, pp. 1205–11, Sep 2010.

[57] D. S. Tuch, T. G. Reese, M. R. Wiegell, N. Makris, J. W. Belliveau, and V. J. Wedeen, "High angular resolution diffusion imaging reveals intravoxel white matter fiber heterogeneity," *Magnetic Resonance in Medicine*, vol. 48, no. 4, pp. 577–582, 2002.

[58] M. Singh and C.-W. Wong, "Independent component analysis-based multifiber streamline tractography of the human brain," *Magn Reson Med*, vol. 64, pp. 1676–84, Dec 2010.

[59] M. Singh and C.-W. Wong, "Recovery of multiple fibers per voxel by ica in dti tractography," *Conf Proc IEEE Eng Med Biol Soc*, vol. 1, pp. 735–8, 2006.

[60] V. Wedeen, R. Wang, J. Schmahmann, T. Benner, W. Tseng, G. Dai, D. Pandya, P. Hagmann, H. D'Arceuil, and A. De Crespigny, "Diffusion spectrum magnetic resonance imaging (dsi) tractography of crossing fibers," *Neuroimage*, vol. 41, no. 4, pp. 1267–1277, 2008.

[61] V. J. Wedeen, P. Hagmann, W.-Y. I. Tseng, T. G. Reese, and R. M. Weisskoff, "Mapping complex tissue architecture with diffusion spectrum magnetic resonance imaging," *Magnetic Resonance in Medicine*, vol. 54, no. 6, pp. 1377–1386, 2005.

[62] J.-D. Tournier, F. Calamante, D. G. Gadian, and A. Connelly, "Direct estimation of the fiber orientation density function from diffusion-weighted mri data using spherical deconvolution," *Neuroimage*, vol. 23, no. 3, pp. 1176–1185, 2004.

[63] R. W. Cox *et al.*, "Afni: software for analysis and visualization of functional magnetic resonance neuroimages," *Computers and Biomedical research*, vol. 29, no. 3, pp. 162–173, 1996.

[64] R. Wang, T. Benner, A. Sorensen, and V. Wedeen, "Diffusion toolkit: a software package for diffusion imaging data processing and tractography," in *Proc Intl Soc Mag Reson Med*, vol. 15, p. 3720, 2007.

[65] A. Hyvärinen and E. Oja, "A fast fixed-point algorithm for independent component analysis," *Neural computation*, vol. 9, no. 7, pp. 1483–1492, 1997.

[66] P. Maillard, E. Fletcher, D. Harvey, O. Carmichael, B. Reed, D. Mungas, and C. DeCarli, "White matter hyperintensity penumbra," *Stroke*, vol. 42, pp. 1917–22, Jul 2011.

[67] L. C. Silbert, H. H. Dodge, L. G. Perkins, L. Sherbakov, D. Lahna, D. Erten-Lyons, R. Woltjer, L. Shinto, and J. A. Kaye, "Trajectory of white matter hyperintensity

burden preceding mild cognitive impairment," *Neurology*, vol. 79, pp. 741–7, Aug 2012.

[68] J. P. Seab, W. J. Jagust, S. T. S. Wong, M. S. Roos, B. R. Reed, and T. F. Budinger, "Quantitative nmr measurements of hippocampal atrophy in alzheimer's disease," *Magn. Reson. Med.*, vol. 8, no. 200-208, 1988.

[69] P. M. Thompson, C. Schwartz, R. T. Lin, A. A. Khan, and A. W. Toga, "Three-dimensional statistical analysis of sulcal variability in the human brain," *J. Neurosci*, vol. 16, pp. 4261–4274, 1996.

[70] J. Ashburner and K. J. Friston, "Nonlinear spatial normalization using basis functions," *Human Brain Mapping*, vol. 7, no. 4, pp. 254–266, 1999.

[71] K. Juottonen, M. P. Laakso, K. Partanen, and H. Soininen, "Comparative mr analysis of the entorhinal cortex and hippocampus in diagnosing alzheimer disease," *AJNR Am J Neuroradiol*, vol. 20, no. 139-144, 1999.

[72] I. D. Dinov, M. S. Mega, P. M. Thompson, L. Lee, R. P. Woods, C. J. Holmes, D. W. Sumners, and A. W. Toga, "Analyzing functional brain images in a probabilistic atlas: a validation of subvolume thresholding," *J. Comput. Assist. Tomogr.*, vol. 24, pp. 128–138, 2000.

[73] B. Fischl, D. H. Salat, and E. Busa, "Whole brain segmentation: automated labeling of neuroanatomical structures in the human brain," *Neuron*, vol. 33, no. 341-355, 2002.

[74] S. M. Smith, "Fast robust automated brain extraction," *Hum. Brain Mapp*, vol. 17, no. 143-155, 2002.

[75] B. Fischl, A. van der Kouwe, C. Destrieux, E. Halgren, F. Segonne, and et al, "Automatically parcellating the human cerebral cortex," *Cereb Cortex*, vol. 14, no. 11-22, 2004.

[76] Y. Kabir, M. Dojat, B. Scherrer, F. Forbes, and C. Garbay, "Multimodal mri segmentation of ischemic stroke lesions," *Conf. Proc. IEEE Eng Med. Biol. Soc*, pp. 1595–1598, 2007.

[77] P. Nachev, E. Coulthard, H. R. Jager, C. Kennard, and M. Husain, "Enantiomorphic normalization of focally lesioned brains," *Neuroimage*, vol. 39, pp. 1215–1226, 2008.

[78] A. Klein, J. Andersson, B. Ardekani, J. Ashburner, B. Avants, M. Chiang, G. Christensen, D. Collins, J. Gee, P. Hellier, J. Song, M. Jenkinson, C. Lepage, D. Rueckert, P. Thompson, T. Vercauteren, R. Woods, J. Mann, and R. Parsey, "Evaluation of 14 nonlinear deformation algorithms applied to human brain mri registration," *Neuroimage*, vol. 46, no. 3, pp. 786–802, 2009.

[79] A. Solodkin, U. Hasson, R. Siugzdaite, M. Schiel, E. Chen, K. Rolf, and S. Small, "Virtual brain transplantation (vbt): A method for accurate image registration and parcellation in large cortical stroke," *Arch Ital Biol*, vol. 148, no. 3, pp. 219–41, 2010.

[80] A. Albanese, C. Hall, and R. Stanhope, "The use of a computerized method of bone age assessment in clinical practice," *Horm Res*, pp. 2–7, 1995.

[81] W. Grelich and S. Pyle, *Radiographic Atlas of Skeletal Development of Hand Wrist, Stanford, CA: Stanford University Press*. 1959.

[82] A. Gertych, A. Zhang, J. Sayre, S. Pospiech-Kurkowska, and H. K. Huang, "Bone age assessment of children using a digital hand atlas," *to appear in J Comp Med Imag Graphic*, vol. 31, pp. 4–5, May 2007.

[83] H. K. Huang, A. Zhang, B. Liu, Z. Zhou, J. Documet, N. King, and L. W. C. Chan, "Data grid for large-scale medical image archive and analysis," in *Proceedings of the 13th ACM International Conference on Multimedia*, pp. 1005–1013, 2005.

[84] E. Pietka, A. Gertych, and K. Witko, "Informatics infrastructure of cad system," *Comput Med Imaging Graph*, vol. 29, pp. 157–69, 2005.

[85] F. Cao, H. K. Huang, E. Pietka, and V. Gilsanz, "Digital hand atlas and web-based bone age assessment: system design and implementation," *Comput Med Imaging Graph*, vol. 24, pp. 297–307, 2000.

[86] E. Pietka, A. Gertych, S. P. E. Kurkowska, F. Cao, H. K. Huang, and V. Gilzanz, "Computerassisted bone age assessment: graphical user interface for image processing and comparison," *J Digit Imaging*, vol. 17, pp. 175–88, 2004.

[87] E. Pietka, A. Gertych, S. Pospiech, F. Cao, H. K. Huang, and V. Gilsanz, "Computer-assisted bone age assessment: image preprocessing and epiphyseal/metaphyseal roi extraction," *IEEE Trans Med Imaging*, vol. 20, pp. 715–29, 2001.

[88] E. Pietka, S. Pospiech-Kurkowska, A. Gertych, and F. Cao, "Integration of computer assisted bone age assessment with clinical pacs," *Comput Med Imaging Graph*, vol. 27, pp. 217–28, 2003.

[89] A. G. Zhang and B. J. Liu, "Automatic bone age assessment for young children from newborn to 7-year- old using carpal bones," *J Comp Med Imag and Graphics*, vol. 31, pp. 4–5, May 2007.

[90] P. DuBois, *MySQL: the definitive guide to using, programming, and administering MySQL 4*. Pearson Education, 3rd ed., 2003.

[91] H. E. Williams, *David Lane Web Database Applications with PHP MySQL*. O'Reilly, 2nd ed., 2002.

[92] E. Pietka, A. Gertych, S. Pospiech, F. Cao, H. K. Huang, and V. Gilsanz, "Computer-assisted bone age assessment: image preprocessing and epiphyseal/metaphyseal roi extraction," *IEEE Trans. Med. Imaging.*, vol. 20, pp. 715–729, Aug 2001.

[93] W. Grelich and S. Pyle, *Radiographic Atlas of Skeletal Development of Hand Wrist*. Stanford, CA: Stanford University Press, 1959.

[94] J. M. Tanner and R. H. Whitehouse, *Assessment of Skeletal Maturity and Prediction of Adult Height (TW2 Method)*. London: Academic Press, 1975.

[95] A. Zhang, A. Gertych, B. J. Liu, H. K. Huang, and S. Kurkowska-Pospiech, "Carpal bone segmentation and features analysis in bone age assessment of children," in *Proceedings of RSNA Conference*, (pp.688Chicago, pp.688), Chicago, 2005.

[96] A. Zhang, A. Gertych, B. J. Liu, and H. K. Huang, "Data mining for 'average' image based on phalangeal and carpal bone features in a large-scale digital hand atlas," in *Proceedings of RSNA Conference*, 2006.

[97] A. Zhang, A. Gertych, and B. J. Liu, *Automatic Bone Age Assessment for Young Children from Newborn to 7-Year- Old Using Carpal Bones*. JCMIG, 2007.

[98] A. Zhang, S. Tsao, J. Sayre, A. Gertych, B. J. Liu, and H. K. Huang, "Is greulich and pyle atlas still a good reference for bone age assessment?," in *Proceedings of SPIE Medical Imaging*, February 2007.

[99] A. Gertych, E. Pietka, and B. J. Liu, "Segmentation of regions of interest and post-segmentation edge location improvement in computer-aided bone age assessment," *Pattern Anal Applic*, vol. 10, pp. 115–123, April 2007.

[100] J. Zhou, J. Liu, V. A. Narayan, and J. Ye, "Modeling Disease Progression via Multi-task Learning," *NeuroImage*, 2013.

[101] Y. Wang, L. Yuan, J. Shi, A. Greve, J. Ye, A. W. Toga, A. L. Reiss, and P. M. Thompson, "Applying tensor-based morphometry to parametric surfaces can improve mri-based disease diagnosis," *Neuroimage*, vol. 74, pp. 209–30, Jul 2013.

[102] R. J. Caselli, D. E. C. Locke, A. C. Dueck, D. S. Knopman, B. K. Woodruff, C. Hoffman-Snyder, R. Rademakers, A. S. Fleisher, and E. M. Reiman, "The neuropsychology of normal aging and preclinical alzheimer's disease," *Alzheimers Dement*, Mar 2013.

[103] L. S. Elias-Sonnenschein, S. Helisalmi, T. Natunen, A. Hall, T. Paajanen, S.-K. Herukka, M. Laitinen, A. M. Remes, A. M. Koivisto, K. M. Mattila, T. Lehtimäki, F. R. J. Verhey, P. J. Visser, H. Soininen, and M. Hiltunen, "Genetic loci associated with alzheimer's disease and cerebrospinal fluid biomarkers in a finnish case-control cohort," *PLoS One*, vol. 8, no. 4, p. e59676, 2013.

[104] S. J. Teipel, M. Grothe, S. Lista, N. Toschi, F. G. Garaci, and H. Hampel, "Relevance of magnetic resonance imaging for early detection and diagnosis of alzheimer disease," *Med Clin North Am*, vol. 97, pp. 399–424, May 2013.

[105] G. A. Becker, M. Ichise, H. Barthel, J. Luthardt, M. Patt, A. Seese, M. Schultze-Mosgau, B. Rohde, H.-J. Gertz, C. Reininger, and O. Sabri, "Pet quantification of 18f-florbetaben binding to -amyloid deposits in human brains," *J Nucl Med*, Mar 2013.

[106] K. Blennow and H. Zetterberg, "The application of cerebrospinal fluid biomarkers in early diagnosis of alzheimer disease," *Med Clin North Am*, vol. 97, pp. 369–76, May 2013.

[107] I. Hajjar, L. Brown, W. J. Mack, and H. Chui, "Alzheimer pathology and angiotension receptor blockers," *JAMA Neurol*, vol. 70, p. 414, Mar 2013.

[108] S. G. Mueller, M. W. Weiner, L. J. Thal, R. C. Petersen, C. R. Jack, W. Jagust, J. Q. Trojanowski, A. W. Toga, and L. Beckett, "Ways toward an early diagnosis in alzheimer's disease: the alzheimer's disease neuroimaging initiative (adni)," *Alzheimers Dement*, vol. 1, pp. 55–66, Jul 2005.

[109] B. S. Bagepally, H. N. Halahalli, J. P. John, L. Kota, M. Purushottam, O. Mukherjee, P. T. Sivakumar, S. Bharath, S. Jain, and M. Varghese, "Apolipoprotein e4 and brain white matter integrity in alzheimer's disease: tract-based spatial statistics study under 3-tesla mri," *Neurodegener Dis*, vol. 10, no. 1-4, pp. 145–8, 2012.

[110] M. Schwartz and K. Niswender, "Adiposity signaling and biological defense against weight gain: absence of protection or central hormone resistance?," *J Clin Endocrinol Metab*, vol. 89, pp. 5889–97, 2004.

[111] R. Kuczmarski, C. Ogden, L. Grummer-Strawn, K. Flegal, S. Guo, R. Wei, Z. Mei, L. Curtin, A. Roche, and C. Johnson, "Cdc growth charts: United states," *Adv Data*, pp. 1–27, 2000.

[112] S. Kullmann, M. Heni, R. Veit, C. Ketterer, F. Schick, H. Haring, A. Fritsche, and H. Preissl, "The obese brain: association of body mass index and insulin sensitivity with resting state network functional connectivity," *Hum Brain Mapp*, vol. 33, pp. 1052–61, 2012.

[113] K. Anthony, L. Reed, J. Dunn, E. Bingham, D. Hopkins, P. Marsden, and S. Amiel, "Attenuation of insulin-evoked responses in brain networks controlling appetite and reward in insulin resistance: the cerebral basis for impaired control of food intake in metabolic syndrome?," *Diabetes*, vol. 55, pp. 2986–92, 2006.

[114] N. Tzourio-Mazoyer, B. Landeau, D. Papathanassiou, F. Crivello, O. Etard, N. Delcroix, B. Mazoyer, and M. Joliot, "Automated anatomical labeling of activations in spm using a macroscopic anatomical parcellation of the mni mri single- subject brain," *Neuroimage*, vol. 15, pp. 273–89, 2002.

[115] J. Bruce, L. Hancock, A. Bruce, R. Lepping, L. Martin, J. Lundgren, S. Malley, L. Holsen, and C. Savage, *Changes in brain activation to food pictures after adjustable gastric banding.* Surg Obes Relat Dis, 2011.

[116] K. Page, D. Seo, R. Belfort-DeAguiar, C. Lacadie, J. Dzuira, S. Naik, S. Amarnath, R. Constable, R. Sherwin, and R. Sinha, "Circulating glucose levels modulate neural control of desire for high-calorie foods in humans," *J Clin Invest*, vol. 121, pp. 4161–9, 2011.

[117] T. Adam, C. Toledo-Corral, C. Lane, M. Weigensberg, and D. Spruijt-Metz, "Davies jn a nd goran mi: Insulin sensitivity as an independent predictor of fat mass gain in hispanic adolescents," *Diabetes Care*, vol. 32, pp. 2114–5, 2009.

[118] Y. Rothemund, C. Preuschhof, G. Bohner, H. Bauknecht, R. Klingebiel, H. Flor, and B. Klapp, "Differential activation of the dorsal striatum by high-calorie visual food stimuli in obese individuals," *Neuroimage*, vol. 37, pp. 410–21, 2007.

[119] D. Figlewicz, S. Evans, J. Murphy, M. Hoen, and D. Baskin, "Expression of receptors for insulin and leptin in the ventral tegmental area/substantia nigra (vta/sn) of the rat," *Brain Res*, vol. 964, pp. 107–15, 2003.

[120] J. Tanner, "Growth and maturation during adolescence," *Nutr Rev*, vol. 39, pp. 43–55, 1981.

[121] N. Speed, C. Saunders, A. Davis, W. Owens, H. Matthies, S. Saadat, J. Kennedy, R. Vaughan, R. Neve, C. Lindsley, S. Russo, L. Daws, K. Niswender, and A. Galli, "Impaired striatal akt signaling disrupts dopamine homeostasis and increases feeding," *PLoS One*, 2011.

[122] C. Davis, S. Strachan, and M. Berkson, "Sensitivity to reward: implications for overeating and overweight," *Appetite*, vol. 42, pp. 131–8, 2004.

[123] S. Wallner-Liebmann, K. Koschutnig, G. Reishofer, E. Sorantin, B. Blaschitz, R. Kruschitz, H. Unterrainer, R. Gasser, F. Freytag, C. Bauer-Denk, A. Schienle, A. Schafer, and H. Mangge, "Insulin and hippocampus activation in response to images of high-calorie food in normal weight and obese adolescents," *Obesity (Silver Spring)*, vol. 18, pp. 1552–7, 2010.

[124] M. Goran, R. Bergman, M. Cruz, and R. Watanabe, "Insulin resistance and associated compensatory responses in african-american and hispanic children," *Diabetes Care*, vol. 25, pp. 2184–90, 2002.

[125] J. Lee, "Insulin resistance in children and adolescents," *Rev Endocr Metab Disord*, vol. 7, pp. 141–7, 2006.

[126] D. Figlewicz, J. Bennett, A. Naleid, C. Davis, and J. Grimm, "Intraventricular insulin and leptin decrease sucrose self-administration in rats," *Physiol Behav*, vol. 89, pp. 611–6, 2006.

[127] M. Schwartz, A. Sipols, S. Kahn, D. Lattemann, G. Taborsky, R. Bergman, S. Woods, and D. Porte, "Jr," *: Kinetics and specificity of insulin uptake from plasma into cerebrospinal fluid*, pp. 378–83, 1990.

[128] L. Tamm, V. Menon, and A. Reiss, "Maturation of brain function associated with response inhibition," *J Am Acad Child Adolesc Psychiatry*, vol. 41, pp. 1231–8, 2002.

[129] A. Jastreboff, R. Sinha, C. Lacadie, D. Small, R. Sherwin, and M. Potenza, "Neural correlates of stress- and food cue-induced food craving in obesity: Association with insulin levels," *Diabetes Care*, vol. 36, pp. 394–402, 2013.

[130] M. Cruz, G. Shaibi, M. Weigensberg, D. Spruijt-Metz, G. Ball, and M. Goran, "Pediatric obesity and insulin resistance: chronic disease risk and implications for treatment and prevention beyond body weight modification," *Annu Rev Nutr*, vol. 25, pp. 435–68, 2005.

[131] A. DelParigi, K. Chen, A. Salbe, J. Hill, R. Wing, E. Reiman, and P. Tataranni, "Persistence of abnormal neural responses to a meal in postobese individuals," *Int J Obes Relat Metab Disord*, vol. 28, no. 370-7, pp. 440–8, 2007.

[132] M. Goran, C. Lane, C. Toledo-Corral, and M. Weigensberg, *Persistence of Pre-Diabetes in Overweight and Obese Hispanic Children: Association With Progressive Insulin Resistance, Poor Beta-cell Function and Increasing Visceral Fat*. Diabetes, 2008.

[133] R. Bergman, L. Phillips, and C. Cobelli, "Physiologic evaluation of factors controlling glucose tolerance in man: measurement of insulin sensitivity and beta-cell glucose sensitivity from the response to intravenous glucose," *J Clin Invest*, vol. 68, pp. 1456–67, 1981.

[134] A. Byars, S. Holland, R. Strawsburg, W. Bommer, R. Dunn, V. Schmithorst, and E. Plante, "Practical aspects of conducting large-scale functional magnetic resonance imaging studies in children," *J Child Neurol*, vol. 17, pp. 885–90, 2002.

[135] K. Flegal, C. Ogden, and M. Carroll, "Prevalence and trends in overweight in mexican-american adults and children," *Nutr Rev*, pp. 144–8, 2004.

[136] E. Stice, S. Spoor, C. Bohon, and D. Small, "Relation between obesity and blunted striatal response to food is moderated by taqia a1 allele," *Science*, vol. 322, pp. 449–52, 2008.

[137] A. Must and R. Strauss, "Risks and consequences of childhood and adolescent obesity," *Int J Obes Relat Metab Disord*, pp. 2–11, 1999.

[138] A. Konner, S. Hess, S. Tovar, A. Mesaros, C. Sanchez-Lasheras, N. Evers, L. Verhagen, H. Bronneke, A. Kleinridders, B. Hampel, P. Kloppenburg, and J. Bruning, "Role for insulin signaling in catecholaminergic neurons in control of energy homeostasis," *Cell Metab*, vol. 13, pp. 720–8, 2011.

[139] D. H. Brainard, "The psychophysics toolbox," *Spat Vis*, vol. 10, no. 4, pp. 433–6, 1997.

[140] E. Gomez-Perez, F. Ostrosky-Solis, and O. Prospero-Garcia, "The development of attention, memory and the inhibitory processes: the chronological relation with the maturation of brain structure and functioning]," *Rev Neurol*, vol. 37, pp. 561–7, 2003.

[141] P. Lang, "The emotion probe. studies of motivation and attention," *Am Psychol*, vol. 50, pp. 372–85, 1995.

[142] G. Wang, N. Volkow, and J. Fowler, "The role of dopamine in motivation for food in humans: implications for obesity," *Expert Opin Ther Targets*, vol. 6, pp. 601–9, 2002.

[143] W. Banks, "The source of cerebral insulin," *Eur J Pharmacol*, vol. 490, pp. 5–12, 2004.

[144] E. Boyko, W. Fujimoto, D. Leonetti, and L. Newell-Morris, "Visceral adiposity and risk of type 2 diabetes: a prospective study among japanese americans," *Diabetes Care*, vol. 23, pp. 465–71, 2000.